6-2015

Implementation of Traditional Printing Techniques for the Development of Flexible Printed Sensors

Sai Guruva Reddy Avuthu
Western Michigan University, saiguruva@gmail.com

IMPLEMENTATION OF TRADITIONAL PRINTING TECHNIQUES FOR THE DEVELOPMENT OF FLEXIBLE PRINTED SENSORS

by

Sai Guruva Reddy Avuthu

A Dissertation submitted to the Graduate College
in partial fulfillment of the requirements
for the degree of Doctor of Philosophy
Electrical and Computer Engineering
Western Michigan University
June 2015

Doctoral Committee:

Massood Atashbar, Ph.D, Chair
Margaret Joyce, Ph.D.
Paul D Fleming, Ph.D.
Bradley J Bazuin, Ph.D.

IMPLEMENTATION OF TRADITIONAL PRINTING TECHNIQUES FOR THE DEVELOPMENT OF FLEXIBLE PRINTED SENSORS

Sai Guruva Reddy Avuthu, Ph.D.

Western Michigan University, 2015

Printed electronics has gained a remarkable interest over the past decade for the fabrication of cost efficient electronic devices, with a major focus on the development of flexible sensors. This dissertation focuses on the fabrication of flexible sensors using traditional printing processes such as screen, inkjet and gravure printing.

A flexible organic thin film transistor (OTFT) was successfully fabricated on a polyethylene terephthalate (PET) substrate and employed as a humidity sensor. Aluminum gate electrode was thermally evaporated on PET and UV clear dielectric layer was spin coated. Source and drain silver interdigitated electrodes were screen printed. 6,13-bis(triisopropylsilylethynyl) pentacene, a humidity sensitive material, was inkjet printed. The output characteristics of the printed OTFT were recorded for varying humidity levels, ranging from 15% RH to 85% RH. The humidity response of the fabricated sensor demonstrated the feasibility of using traditional printing processes for the fabrication of OTFT based sensors.

A flexible electrochemical sensor was screen printed on PET. Carbon and silver based inks were used for metallization of the working, counter and reference electrodes. 1,10-phenanthroline and its derivative naphtho[2,3-a]dipyrido[3,2-h:2',3'-f]phenazine-5,18-dione (QDPPZ) was synthesized as sensitive layers for Hg^{2+} and Pb^{2+}, respectively. Cyclic voltammetry response of the sensor resulted in reduction peaks at 0.2 eV and -0.6 eV for selective detection of Hg^{2+} and Pb^{2+}, respectively. The response of the electrochemical sensor demonstrated the use of traditional printing processes and synthesized chemicals for the selective detection of heavy metals.

An inductor capacitor (LC) wireless passive sensor for the detection of toxic heavy metals was screen printed on PET using a silver ink. Palladium nanoparticles were synthesized and drop casted onto the LC sensor as a sensitive layer. The change in resonant frequency of the LC sensor towards varying concentrations of heavy metal ions was remotely monitored using a screen printed detection coil. The LC sensor was able to detect mercury ions (Hg^{2+}), as low as 1 µM, with a resonant frequency shift of 0.2 MHz. The feasibility of the sensor to vary its resonant frequency with different concentrations of heavy metal ions such as Hg^{2+} and lead ions (Pb^{2+}) was demonstrated.

ACKNOWLEDGEMENTS

I would first like to acknowledge my committee chair Dr. Massood Atashbar and committee members Dr. Margaret Joyce, Dr. Paul D Fleming and Dr. Bradley J Bazuin for their guidance and preparation of this dissertation. My advisor, Dr. Massood Atashbar, deserves my gratitude for the tutelage and mentorship he has given me over the past six and half years. His dedication to his students and the electrical and computer engineering (ECE) department has influenced me greatly and I am forever thankful for his guidance. I would also like to give special recognition to Dr. Margaret Joyce, Dr. Paul D Fleming and Dr. Bradley J Bazuin for providing their inputs in all aspects related to this work. I would also like to acknowledge Dr. Sherine O Obare who has provided some of the chemicals used in the study, and also for her invaluable feedback on chemistry related attributes. I thank Dr. Binu B Narakathu, Dinesh Maddipatla, Zeinab Ramshani, Sepehr Emamian, Ali Eshkeiti, Amer A Chlaihawi and Mohammed Ali for their significant support and for being good friends throughout my studies at Western Michigan University.

I would also like to acknowledge Electrical and Computer Engineering Department, Chemical and Paper Engineering Department, Department of Chemistry, Center for Advanced Smart Sensors and Structures (CASSS), Sensors Technology Lab (STL), Center of Advancement in Printed Electronics (CAPE) for all the support given to me during the course of this dissertation.

This dissertation is also a result of encouragement provided by my parents. Especially, I am grateful for their patience and the confidence that they have built on me. And finally, most deservingly, I am thankful to my wife, Dr. Nivya Kolli, for her time and walking side-by-side in all these years of reaching this milestone. I wouldn't have reached this point without the love and affection of my family, thus I would dedicate this dissertation to all my family members.

Sai Guruva Reddy Avuthu

TABLE OF CONTENTS

Tables of Contents—continued

Tables of Contents—continued

LIST OF TABLES

LIST OF FIGURES

List of Figures—continued

List of Figures—continued

CHAPTER I

INTRODUCTION

1.1 Background

Printed electronics (PE) has gained a considerable attention for the fabrication of low-cost and large-area flexible electronic devices using traditional printing processes [1]. It is predicted that in the next two decades, the field of printed electronics will capture a significant portion of the huge market. This is due to the advantages of printing, such as high throughput, minimal usage of resources, lower manufacturing temperature and much less complex fabrication processes, when compared to conventional silicon based technology, which involves high-vacuum and high-temperature deposition processes along with sophisticated photolithographic patterning techniques [2]. A forecast from IDTechEx reports that the printed electronics market will exceed $300 Billion in the next 20 years [3].

PE has been used for the manufacture of radio frequency identification tags (RFID's) [4-5], displays [6-7], organic thin film transistors (OTFT's) [8-9] and sensors [10], using inkjet, gravure, flexographic and screen printing techniques. The manufacturing of sensors on flexible substrates such as plastic, paper and textiles using traditional printing techniques is very fantasizing in the field of PE [11-13]. However, there are a few emerging studies on the adaption of continuous and large area printing methods on flexible substrates for the development of sensors.

There is an urgent need for the development of reliable, miniaturized, accurate and cost effective sensors for use in portable hand-held systems, which detect various toxic heavy metals; particularly in applications such as agricultural, environmental

and medical industries [14-16]. Heavy metals, such as lead (Pb) and mercury (Hg) are highly toxic and carcinogenic even at low concentrations [17]. Moreover, heavy metals are non-biodegradable and accumulate in the food chain, leading to severe threats to human health by affecting metabolic processes, which result in neuromuscular, neurological, nephritic physiological disorders [18]. Thus, rapid and highly sensitive monitoring of heavy metals in the environment and food is very crucial and is beginning to be addressed by this and other work [14-16].

Detection of heavy metals using various techniques such as atomic absorption spectrometry, inductively coupled plasma mass spectrometry and optical methods has been reported [19-21]. However, these techniques are instrumentally intensive, complex and time consuming, thus making the experiments lengthy, massive and expensive. In contrast, the electrochemical detection of lead has proved to be rapid, simple and cost-efficient way of detecting lead ions [22-23]. Miniaturization of the electrochemical sensors leads to small scale experiments, in terms of sample volume, and helps in building hand-held systems with similar accuracy and sensitivity to that of bench-top analyzers. Furthering this approach, the use of microelectrodes in the field of sensors has also been receiving growing attention [24-25]. It was revealed that microelectrodes offer higher sensitivity than macro electrodes. Most of the sensors consisting of microelectrodes are constructed using traditional CMOS fabrication techniques. Even though these sensors are rigid and robust they are costly. Microelectrode sensors fabricated through printing methods have demonstrated similar results [26] but at significantly lower cost.

In recent years, a lot of attention has been given towards the development of humidity based sensors in semiconductor, environmental, agricultural and automobile based industries [27-32]. Humidity sensors are also used in the medical field for

applications in incubators, respiratory equipment, pharmaceutical processing, sterilizers and biological products [33]. Various detection techniques have been reported for measuring humidity. To name a few, capacitive/resistive [34], optical [35], thermal [36] and surface acoustic wave sensors [37] have attracted interest. Recently, the use of OTFTs for humidity sensing has also been reported [29]. OTFT has a distinct advantage when compared to other techniques, by controlling the gate bias voltage, amplification of the humidity response can be provided [38]. Currently, the OTFT based humidity sensors reported in the literature have been fabricated using Si based fabrication techniques [38]. The recent trend of using traditional printing methods in the field of PE provides a promising technique for the fabrication of OTFT based flexible humidity sensors.

1.2 Author's Contributions

The author's research work has resulted in **thirty seven conference publications, one intellectual property (IP) disclosure, one patent applications and eight high-quality peer-reviewed journal publications** as given in the list of publications in Appendix A. A "*" was used to denoted on the publications directly related to this dissertation work. The outcomes of the projects have been published in prestigious journals such as *Journal of Sensor Letters*, *IEEE Transactions on Components, Packaging and Manufacturing Technology*, *International Journal of Engineering Research & Technology*, and the *Sensors and Actuators: B Chemical*. The author has also presented the research work at several international conferences, which have been published in the proceedings of the IEEE Sensors Conference (2010, 2012, 2013, 2014); International Meeting for Chemical Sensors (IMCS) (2010, 2012, 2014); Annual Flexible Electronics and Displays Conference (2011, 2013, 2014); Eurosensors Conference (2011); International Conference on Sensing Technology

(ICST) (2012); and IEEE International Conference on Electro/Information Technology (EIT) (2013). The author was also awarded the Department level Graduate Research and Creative Scholar Award for 2012-13 by Western Michigan University.

1.3 Organization of the Dissertation

In this dissertation, the author presents the details of the research projects that were performed during the course of his Doctoral studies. The first research project is focused on the development of a screen printed electrochemical sensor for selective detection of lead and mercury ions in DI water. In addition, the author developed a screen printed wireless passive LC sensor for detection of heavy metals. During the course of his doctoral studies, the author also focuses on fabrication of organic thin film transistors (OTFT) and implementing the fabricated device as a humidity sensor. The rest of the dissertation is organized in five chapters.

Chapter 2 includes the comprehensive literature review consisting of introduction to sensors and PE. A brief discussion on overview of sensors, sensor characteristics and different types of sensors is included. A detailed review on two specific sensors (electrochemical and humidity sensors), which have been designed, fabricated and tested as part of the dissertation work is presented. This chapter also includes the review of different printing techniques used in the fabrication of electronics devices and challenged associated with direct printing of electronic devices.

In chapter 3, the development of a printed OTFT sensor for the detection of relative humidity is presented. This includes the design, fabrication and characterization of the OTFT sensor. The measurement setup for testing and the humidity response of the fabricated sensor are presented. The test results and device

response demonstrate the feasibility of integrating traditional printing processes with conventional photolithographic techniques in the fabrication of an OTFT sensor for detection of humidity.

Chapter 4 presents the design, fabrication and characterization of wireless passive inductive capacitor (LC) sensors for the detection of heavy metal ions. The resonant frequency of a printed LC sensor is remotely monitored using an inductively coupled sensing coil. The experiment setup and test results of the LC sensors are also presented. The capability of the sensor to vary its resonant frequency with different concentrations of toxic heavy metals is demonstrated.

In chapter 5, development of screen printed electrochemical sensor for selective detection of heavy metals is presented. This includes the design, fabrication and characterization of an electrochemical sensor on a flexible substrate, and the synthesis of selective layers for the detection of lead and mercury. The measurement setup for testing and voltammetric response of the electrochemical sensors is also presented. The voltammetric response of the printed sensor demonstrated the feasibility of using printed sensors for selective detection of heavy metals in DI water.

Finally, chapter 6 summarizes the dissertation work performed conclusions and provides suggestions for future work

References

[1] E.B. Secor, S. Lim, H. Zhang, C.D. Frisbie, L.F. Francis, M.C. Hersam, “Gravure printing of graphene for large-area flexible electronics”, Advanced materials, vol. 26 pp. 4533–4538, 2014.

[2] C. Reese, M. Roberts, M. Ling, Z. Bao, “Organic thin film transistors”, Materials Today, vol. 7(9) pp. 20-27, 2004.

[3] IDTechEx, Market research report, Printed Electronics 2011.

[4] M. Rebros, E. Hrehorova, B. Bazuin, M. Joyce, P. D. Fleming, A. Pekarovicova, “Rotogravure Printed UHF RFID Antennae Directly on Packaging Materials, TAGA 60th Annual Technical Conference, San Francisco, CA, pp. 16-19, 2008

[5] C. Aliaga, B. Ferreira, M. Hortal, M.A. Pancorbo, J.M. López, F.J. Navas, “Influence of RFID tags on recyclability of plastic packaging”, Waste Management (oxford), vol. 31 pp. 1133–1138, 2011.

[6] C. Wu, X.F. Jin, “Optimization design and fabrication of annular field emitter for field emission display panel”, Key Engineering Materials, vol. 467 pp. 1520-1523, 2011.

[7] R. Ramakrishnan, N. Saran, R.J. Petcavich, Selective inkjet printing of conductors for displays and flexible printed electronics, J. Disp. Technol. 7 (2011) 344-347.

[8] C.T. Lin, C.H. Hsu, I.R. Chen, C.H. Lee, W.J. Wu, Enhancement of carrier mobility in all-inkjet-printed organic thin-film transistors using a blend of poly(3-hexylthiophene) and carbon nanoparticles, Thin Solid Films 519 (2011) 8008–8012.

[9] L. Jiang, J. Zhang, D. Gamota, C.G Takoudis, Organic thin film transistors with novel thermally cross-linked dielectric and printed electrodes on flexible substrates, Org. Electron. 11 (2010) 959-963.

[10] G. Chitnis and B. Ziaie, “Waterproof Active Paper via Laser Surface Micropatterning of Magnetic Nanoparticles” ACS Applied Materials and Interfaces vol. 4, 4435-4439, 2012.

[11] S. Melamed, L. Ceriotti, W. Weigel, F. Rossi, P. Colpo, S. Belkin, “A printed nanolitre-scale bacterial sensor array”, Lab on Chip, vol. 11, pp. 139-146 2011.

[12] A.S.G. Reddy, B.B. Narakathu, M.Z. Atashbar, M. Rebros, E. Hrehorova, M.K. Joyce, “Printed electrochemical based biosensors on flexible substrates”, 9th IEEE Sensors Conference, November 1-4, Waikoloa, Hawaii, USA, pp. 1596-1600, 2010.

[13] A.S.G. Reddy, B.B. Narakathu, M.Z. Atashbar, M. Rebros, E. Rebrosova, M. Joyce, B.J Bazuin, P.D. Fleming, A. Pekarovicova, “Printed capacitive based humidity sensors on flexible substrates”, Sensors Letters, vol. 9 pp. 869-871, 2011.

[14] B.B. Narakathu, W. Guo, S.O. Obare, M.Z. Atashbar, “Novel approach for detection of toxic organophosphorus compounds”, Sensors and Actuators B Chemical vol. 158(1), pp. 69-74, 2011.

[15] J. Wang, “Nanomaterial-based electrochemical biosensors”, Analyst, vol. 130 pp. 421-426, 2005.

[16] B.B. Narakathu, B.E. Bejcek, M.Z. Atashbar, “Improved detection limits of toxic biochemical species based on impedance measurements in electrochemical biosensors”, Biosensors and Bioelectronics vol. 26, pp. 923–928, 2010.

[17] M. Li, H. Gou, I.A. Ogaidi, N. Wu, “Nanostructured sensors for detection of heavy metals: A Review”, ACS Sustainable Chemical Engineering vol. 1 pp. 713−723, 2013.

[18] B. Ibarlucea, C.D. Gil, J.R.I, Veciana, A. Caballero, F. Zapata, A. Tárraga, P.S. Molina, S. Demming, S. Büttgenbach, C.S. Fernández, A. Llobera, "PDMS based photonic lab-on-a-chip for the selective optical detection of heavy metal ions", Analyst, vol. 138 pp. 839-844, 2013.

[19] L. Moens, T.D. Smaele, R. Dams, P.V.D. Broeck P. Sandra, "Sensitive, Simultaneous Determination of Organomercury, -lead, and -tin Compounds with Headspace Solid Phase Microextraction Capillary Gas Chromatography Combined with Inductively Coupled Plasma Mass Spectrometry", Analytical Chemistry, vol. 69, pp. 1604-1611, 1997.

[20] M.T. Naseri, M.R.M. Hosseini, Y. Assadi, A. Kiani, "Rapid determination of lead in water samples by dispersive liquid–liquid microextraction coupled with electrothermal atomic absorption spectrometry", Talanta, vol. 75, pp. 56-62, 2008.

[21] J. Liu, Y. Lu, "A Colorimetric Lead Biosensor Using DNAzyme-Directed Assembly of Gold Nanoparticles", Journal of the American Chemical Society, vol. 125, pp. 6642-6643, 2003.

[22] X. Wang, G. Ye, X. Wang, "Hydrogel diffraction gratings functionalized with crown ether for heavy metal ion detection", Sensors and Actuators B: Chemical, vol. 193 pp. 413-419, 2014.

[23] P. Jothimuthu, R.A. Wilson, J. Herren, E.N. Haynes, W.R. Heineman, I. Papautsky, "Lab-on-a-chip sensor for detection of highly electronegative heavy metals by anodic stripping voltammetry", Biomedical Microdevices vol. 13, pp. 695-703, 2011.

[24] B.B. Narakathu, B.E. Bejcek, M.Z. Atashbar, “Pico-mole level detection of toxic bio/chemical species using impedance based electrochemical biosensors”, Sensors Letters, vol. 9(2) pp. 872-875, 2011.

[25] B.B. Narakathu, B.E. Bejcek, M.Z. Atashbar, “Impedance based electro-chemical biosensors”, 8th IEEE Sensors Conference, October 25-28, Christchurch, New Zealand, pp. 1212-1216, 2009.

[26] A.S.G. Reddy, B.B. Narakathu, M.Z. Atashbar, M. Rebros, E. Hrehorova, M. Joyce, “Printed electrochemical based biosensors on flexible substrates,” 10th IEEE Sensors conference, pp.1596-1600, 2010.

[27] M. Consales, A. Buosciolo, A. Cutolo, G. Breglio, A. Irace, S. Buontempo, P. Petagna, M. Giordano, A. Cusano, “Fiber optic humidity sensors for high-energy physics applications at CERN”, Sensors and Actuator B Chemical vol. 159, pp. 66-74, 2011.

[28] K.M. Tan, S.C. Tjin, C.C. Chan, L. Mohanty, C.M. Tay, “High relative humidity sensing using gelatin-coated long period grating”, in Proceedings of SPIE - the International Society for Optical Engineering, pp. 375-378, 2005.

[29] Z. Zhu, J. T. Mason, R. Dieckmann, G. G. Malliaras, “Humidity sensors based on pentacene thin-film transistors”, Applied Physics Letters, vol. 81, pp. 4643-4645, 2002.

[30] N. Ichinose, “Ceramic Sensors in the Microprocessor Industry”, Ceramurgia, vol.18, pp. 79-83, 1988.

[31] I. Naydenova, R. Jallapuram, V. Toal, S. Martin, “Hologram-based humidity indicator for domestic and packaging applications, Proceedings of SPIE - the International Society for Optical Engineering, vol. 6528, pp. 1-8, 2007.

[32] Z. Chen, C. Lu, “Humidity sensors: A review of materials and mechanisms”, Sensors Letters vol. 3, pp.274-295, 2005.

[33] A. Tételin, C. Pellet, C. Laville, G. N'Kaoua, “Fast response humidity sensors for a medical microsystem”, Sensors and Actuators B Chemical vol. 91, pp. 211-218 2003.

[34] A.S.G. Reddy, B.B. Narakathu, M.Z. Atashbar, M. Rebros, E. Rebrosova, B.J. Bazuin, M.K. Joyce, P.D. Fleming, A. Pekarovicova, “Printed capacitive based humidity sensors on flexible substrates”, Sensors Letters, vol.9, pp. 869-871, 2011.

[35] Y.J. Liu, J. Shi, F. Zhang, H. Liang, J. Xu, A. Lakhtakia, S.J. Fonash, T.J. Huang, “High-speed optical humidity sensors based on chiral sculptured thin films”, Sensors and Actuator B Chemical vol. 156, pp. 593-598, 2011.

[36] O. Legendre, H. Bertin, H. Mathias, F. Mailly, S. Megherbi, “Novel humidity sensing method based on the transient response of a micro-heater”, Sensors and Actuators A Physics vol. 192, pp. 92-100, 2013.

[37] Y. Liu, C.H. Wang, Y. Li, “BCB film based SAW humidity sensor”, Electronics Letters vol. 47, pp. 1012-1014, 2011.

[38] P. Lin, F. Yan, “Organic thin-film transistors for chemical and biological sensing”, Advanced Materials vol.24, pp. 34-51, 2012.

CHAPTER II

LITERATURE REVIEW

2.1 Introduction to Sensors

The advancement of sensor innovation has continually been determined by the enabling progress made in material science and engineering. The growth of the sensor industry increased significantly with the advent of the semiconductor industry in 1960's. Since then, the modern era of sensors, with explosive growth, has come about based on the influence and demand of multiply industries; including, automotive, consumer electronics, manufacturing, infrastructure, aerospace and ship building industries [1-11]. Subsequently, silicon (Si) based fabrication techniques have become a traditional way of fabricating sensors.

The integration of sensors into modern life and the expected increase is apparent from the market analysis information. According to the IC Insights, the global sales of the conventional sensors were $8 billion in the year 2014. The compound annual growth rate (CAGR) of traditional sensor market is forecasted to be 16 % in 2015 compared to 2014, reaching $9.2 billion. It is also predicted the total number of sensor units will be 9.3 billion by the year 2018. The global market forecast of the sensors is shown in Fig. 2.1 [12].

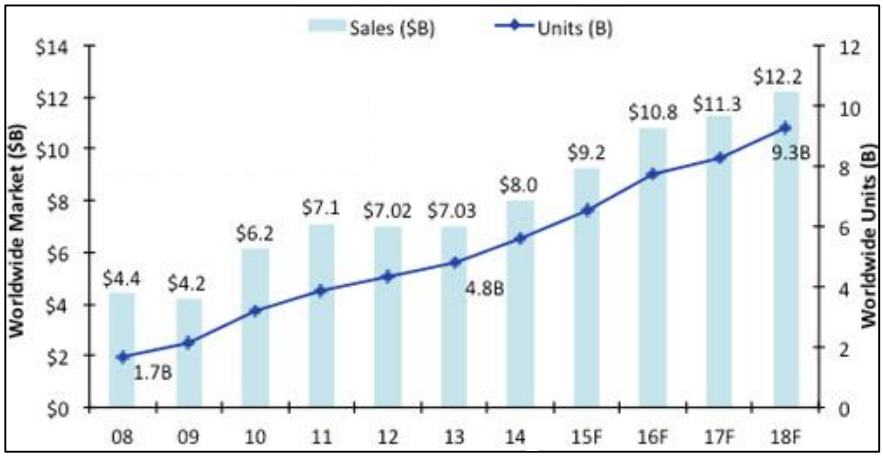

Figure 2.1. Global market of traditional fabricated sensors [12]

2.2 Overview of Sensors

A sensor is defined as a device that detects and measures a stimulus or physical quantity [13]. Based on this broad definition, the term sensor covers everywhere from a human sensors to a trigger in the pistol. Sensors can be classified as natural and man-made sensors. The human body can be considered as a good example of natural sensing system that contains a wide variety of the sensors capable of selectively and sensitively detecting a wide variety of stimuli. The human body consists of vison, hearing, smell, taste and touch sensors as eyes, ears, nose, tongue and skin, respectively. The senses of all the living organism can also be considered as a natural sensors. A compass is one of the earliest artificial sensor known to mankind even before Roman times [14]. A compass is typically constructed by hanging a thin magnetic needle to a thread, which constantly point in the northerly direction. A compass was a navigation tool for early travels and explorers on land and sea.

The earliest man-made modern sensor that is still used in present day is a mercury bulb thermometer, which was invented by Gabriel Fahrenheit in 1714 [15]. A schematic representation of a typical liquid-in-glass thermometer is shown in Fig. 2.2 [16]. The main parts of the thermometer are bulb, stem, liquid and markings.

The bulb is the thin glass container which holds the liquid, usually mercury. Markings are etched or printed on a glass stem (as shown in Figure 2.2). The mechanism of the liquid-in-glass thermometer is based on the expansion of the liquid with respect to temperature. When the temperature increases, the liquid in the bulb is forced to move up due to capillary action. The position of the mercury in the bulb with respect to temperature can be read using the markings on the glass stem. The volume of mercury after expansion is given by [16]

$$V = V_0 \times \rho \tag{1}$$

where V_0 is the volume at 0° C temperature and ρ is

$$\rho = 1 + \alpha t + \beta t^2 \tag{2}$$

where α and β are coefficients of thermal expansion and t is the temperature.

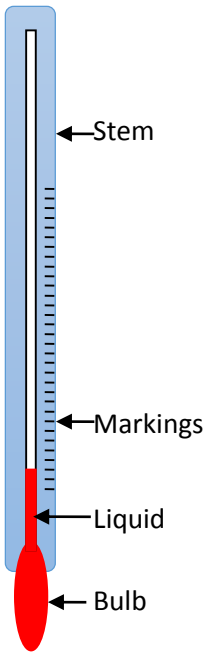

Figure 2.2. Liquid in thermometer.

Artificial sensors in the present day can be classified as absolute and relative sensors. A relative sensor detects the stimulus in reference to a signal that relates to some special case, whereas the absolute sensor produces a signal with respect to an

absolute physical scale. The best examples of absolute and relative sensors are absolute and relative pressure sensors. A relative pressure sensor generates a signal with respect to the selected baseline of non-zero pressure, whereas the absolute pressure sensors generate output with respect to a zero pressure or vacuum [17]. Sensors can also be classified based on how they transduce an input, either as direct or complex sensors. A direct sensor converts the stimulus directly into necessary output signals without any intermediate step, whereas complex sensors need one or more transduction processes to generate a necessary output. A mercury bulb thermometer shown in Fig. 2.2, is a good example of direct sensor in which temperature is directly shown on the marking of the stem. Glucometers available in the market comes under the class of complex sensors. The enzyme present on the electrode reacts with the blood glucose resulting in a flux which is then detected by glucometer [18].

2.2.1 Sensing System

Often, a sensor does not function by itself and must be a part of a larger sensing system that may consists of one or multitude of sensors, signal conditioners, memory devices and data recorders. Many man-made sensing systems can be compared with the sensing and processing of living organisms. Some similarities include; acquiring and processing of the physical inputs, changes in the properties of the receptors in response to the environmental parameters, amplification of the receptor signals and processing by a microcomputer or central nervous system. Figure 2.3 illustrates the similarities between man-made systems and living organisms.

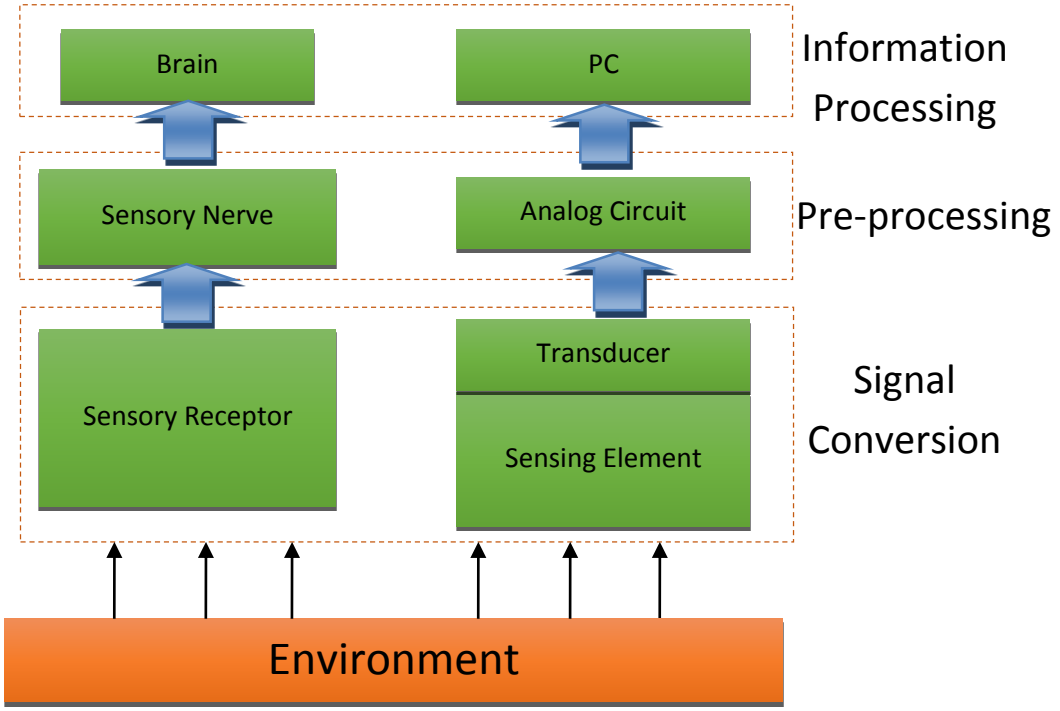

Figure 2.3. Signal processing in living organisms and in intelligent machines.

The sensing system is the complete system that displays the response of the sensor to an input stimulus. The output value of the system can be any format. For instance, consider the example of mercury bulb thermometer in Fig. 2.2, the expansion and contraction of the mercury inside a glass thermometer (temperature sensing system) displays the corresponding temperature on the marking of the stem. A strain gauge converts strain into a corresponding electrical resistance, which can be read by an ohm meter. The change in resistance can also be converted into a voltage or current. A basic sensing system with an electrical output is shown in Fig. 2.4. [19-20]

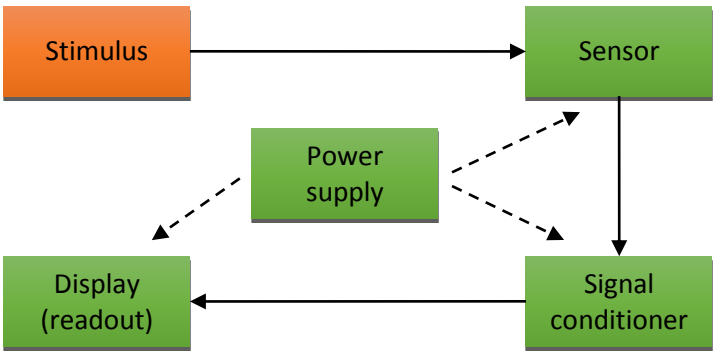

Figure 2.4. Sensing systems with electrical output [19-20].

The sensor responds to the input stimulus with an electrical output. This output could be quite small and subjected to various noise or interference sources. A signal conditioner modifies the sensed output signal into an amplified and possibly filtered electrical signal, which is stronger with less noise susceptibility, potentially has a higher signal to noise ratio, and is compatible with the display device or readout. Signal conditioners vary from impedance matching devices to multiple stage amplifiers with filtering. The display device presents an appropriate output signal corresponding to the input stimulus. The power supply provides the electrical power to the signal conditioner and display device.

Usually two or more sensors are integrated into a sensing system that is designed to handle and display the outputs of multiple sensors. These sensors can be of the same type (several thermocouples) or different type of sensors (pressure, vibration and biosensors). Signal conditioning can be minimized by standardizing the output of all the sensors, that is, regardless of the measurands the output of all the sensors should be the same full-scale electrical output to the system [21].

2.3 Sensors Specifications

Sensor specifications define the performance of the sensor. Response time, recovery time, reproducibility, stability, sensitivity, resolution, dead band, non-linearity and hysteresis are some of the key sensor specifications.

Response and recovery times can be explained by considering the typical sensor response (shown in Fig. 2.5). The time taken by sensor to reach 90 % of the steady state value after exposure to the input stimulus is defined as response time. Recovery time is the time that sensor has taken to reach 10 % of its original equilibrium state after removing the input stimulus. Typically recover time is longer than the response time. Consider the case of a chemical/biological sensor, when an input stimulus is exposed, the sensors responds as soon as the initial reaction takes place. In case of recovery time, the sensor might have to go through the addition reverse reaction to reach its original equilibrium value [22].

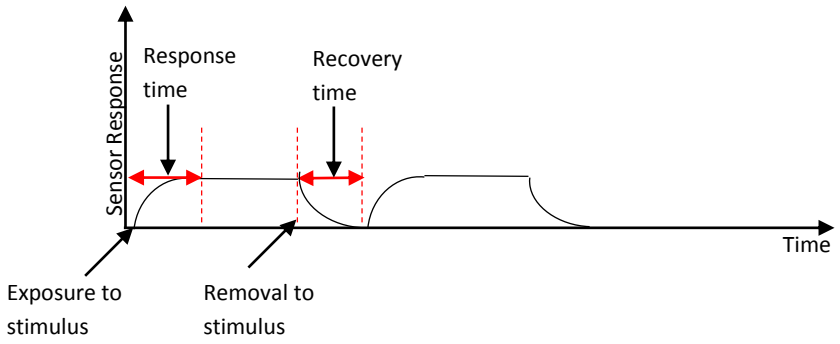

Figure 2.5. Typical sensor response showing response time and recovery times. [22]

Reproducibility of the sensor demonstrates the ability of the sensor to produce the same state of output including similar response and recovery times when exposed to the particular input. For example from Fig. 2.5, the sensor was repeatable for 3 times. Over a period of time and repetitive use of the sensor, its performance might degrade due to accumulation of impurities on the sensing element. The amount of

time it takes for the sensor permanence to vary from its original value to a degraded value is commonly referred as aging [23].

Stability can be considered both as short term and long term stability. Short term stability can be defined as the small deviation of the sensor response from a steady state value. The deviation can appear as either a drift or a ripple or even some unwanted value. In long term stability, aging of the sensor might be taken into account i.e., variation in the study state level, response and recovery times of the sensor for same input stimulus are considered. Any change in these quantities could be considered as instability of the sensor for measurements taken over a period of time.

Resolution can be defined as the smallest input stimulus that can be sensed. Resolution is often limited by the noise in the system. The effect of noise on the resolution can be reduced by using narrow bandwidth filters that provide an increase in the signal to noise ratio. The resolution can also be limited by the resolution of the measuring system itself [23].

Sensitivity(s) is defined as the ratio of small change in output response to the small change in input stimulus. Mathematically (shown in eq.3) sensitivity can be determined from the slope of the response curve (Fig. 2.6), which, for example, could be the sensor response as a function of concentration of input stimulus [24].

$$S = \frac{\Delta Y}{\Delta X} = \frac{Y_2 - Y_1}{X_2 - X_1} \tag{3}$$

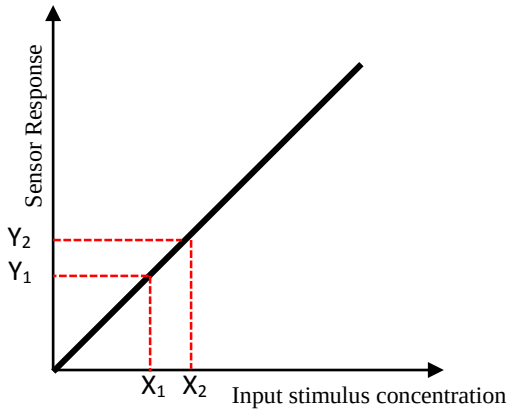

Figure 2.6. Typical sensor response.

Saturation is a point at which sensor stops responding to the input stimulus and remains at a constant output. This happens when a further increase in the dose or input stimulus doesn't effect the output response of the sensor.

Dead band is the region where sensor stops responding to the input stimulus. The output of the sensor may be a certain value or even zero in the dead band. Figure 2.7 shows a dead band in the sensor response [25].

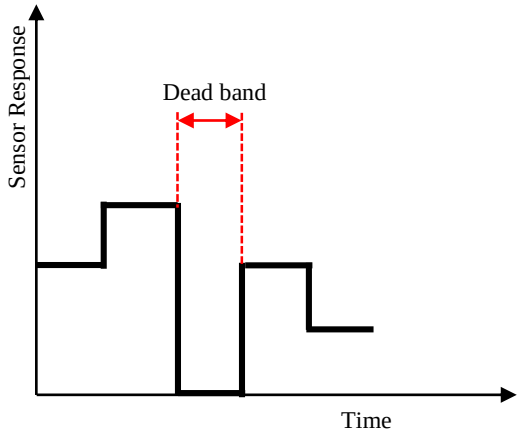

Figure 2.7. Dead band in sensor response.

Non linearity is defined as the deviation of the sensor response from its ideal transfer function over the specified dynamic range. The ideal transfer function can be approximated by a straight line. Figure 2.8 shows the nonlinearity of the sensor response. A straight line has been drawn between two points of output response

corresponding to the smallest and highest input stimulus. The amount of deviation from this straight line is nonlinearity of the sensor [26].

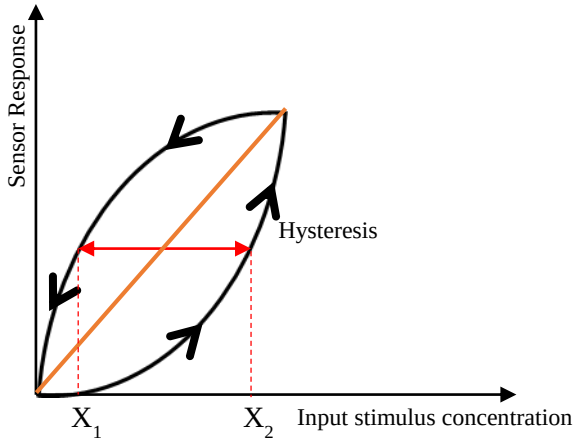

Figure 2.8. Nonlinearity in sensor response.

Hysteresis is the deviation of the sensor when the input stimulus is exposed from the opposite direction. Consider the sensor response in Fig. 2.8, the difference of two points X_2 and X_1 is the hysteresis of the sensor.

2.4 Types of Sensors

Sensors can be classified in many different ways depending upon their sensing schemes. One of the classification of sensors is based on how they transduce an input, either as indirect or direct sensors. An indirect sensor uses intermediate transducers to give the required output whereas the direct sensors respond without any intermediate step. The major classification of the sensors is based on their detection modes. Here the sensors can be classified as acoustic, chemical/biological, mechanical, optical and thermal sensors.

2.4.1 Acoustic Sensors

Acoustic sensors modify the amplitude or the velocity of the input acoustic signal with respect to input stimulus, which can be measured by measuring the frequency or phase of the sensor. The concept of an acoustic sensor can be explained

by considering an acoustic temperature sensor (shown in Figure 2.9). A dry air filled sealed tube, piezoelectric transmitter and piezoelectric receiver are the main components of the acoustic temperature sensor. An acoustic wave is generated in the dry air tube by an electric signal given to the transmitter. The receiving piezoelectric crystal converts the modified acoustic signal back into an electrical signal. Analyzing the change in the received signal when compared to the transmitted signal, the temperature in the tube can be determined [13].

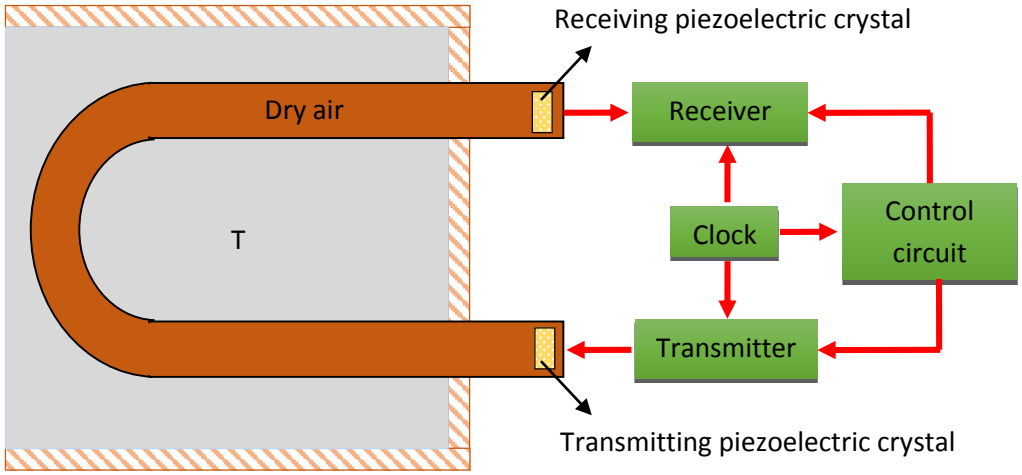

Figure 2.9. Schematic of an acoustic temperature sensor [13].

2.4.2 Mechanical Sensors

Mechanical sensors work on the principle of generating an electric signal in response to the mechanical deflection or deformation of the sensing layer caused by position, pressure, stress, acceleration or flow rate of the input stimulus. Capacitive or piezoresisitve change is often used as sensing mechanisms in mechanical sensors. A capacitive pressure sensor (shown in Fig. 2.10) can be treated as an example of a mechanical sensor, where changes in capacitance occur due to an applied pressure.

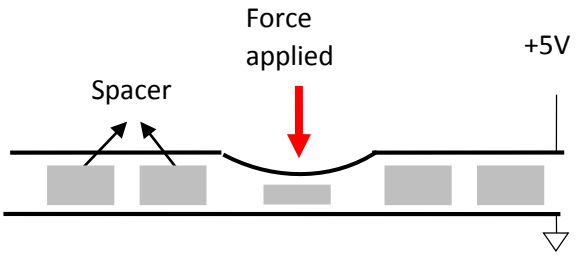

Figure 2.10. Schematic of a capacitive pressure sensor.

Typically, for capacitive pressure sensors, two conductors are mounted on a non-conducting elastomer sheet. The capacitance between the two conducting plates is given by equation 4.

$$C = \frac{\varepsilon_r \varepsilon_0 A}{d} \tag{4}$$

where C is the capacitance, ε_r, is the dielectric constant of the elastomer, ε_0 is the permittivity of the vacuum, A is the overlapping area of the conducting parallel plates and d is the distance between the plates. When the force is applies the distance between the plates reduces resulting in an increase in capacitance.

Piezoresistive material is used to form another class of mechanical sensors. Barium titanate is the material most often used for piezoresistors. Piezoelectric sensors change their voltage in response to mechanical deflection or an applied pressure. The example of the peizoresistive based pressure sensors is shown in Fig. 2.11 [27]. These sensors are usually fabricated using silicon based techniques. They are completely passive and do not need any power supply; the output voltage of a Barium titanate sample undergoing an applied force can be directly measured using an oscilloscope or a voltmeter.

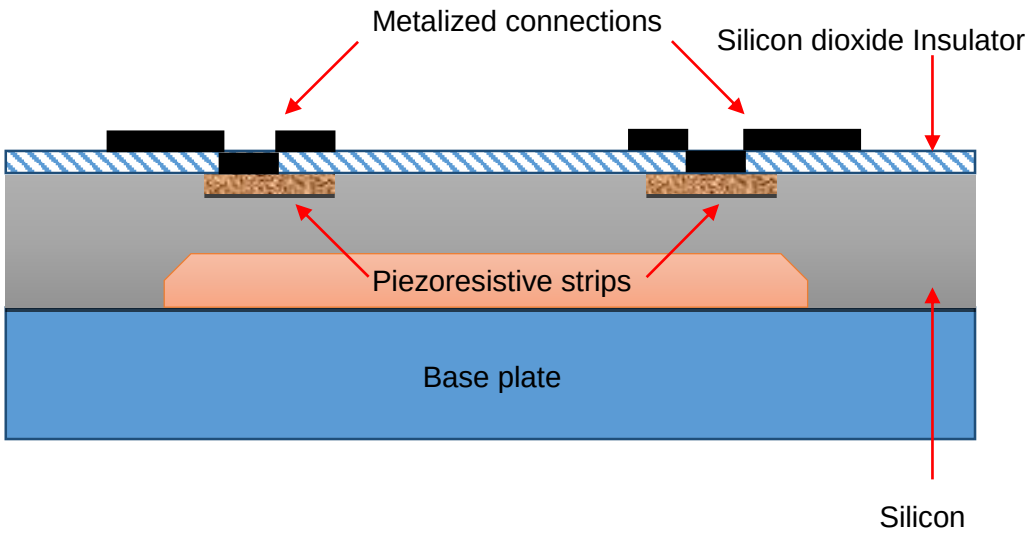

Figure 2.11. Schematic of piezoresistive pressure sensor [27].

2.4.3 Optical Sensors

Optical sensors convert the input stimulus to the optical quantity and an optoelectronic transducer changes the optical quantity to an electrical signal for data post processing. Most of the optical sensors work with optical fibers. Core and cladding are the main parts of the optical fiber. The basic structure of the optical fiber is shown in Fig. 2.12 [28].

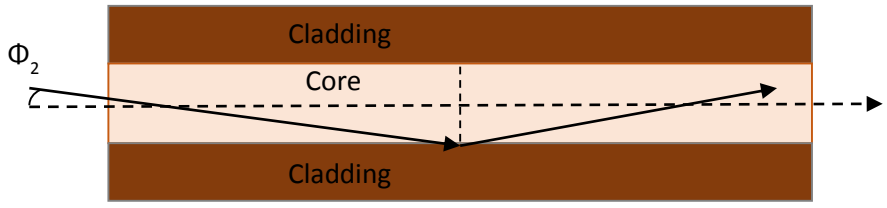

Figure 2.12. Basic structure of optical fiber [28].

The refractive index of the core is always greater than the refractive index of the cladding. The light signal propagated into the optical fiber with angles above the critical angle will continue to travel in optical fiber with almost zero propagation loss over a long distance. A Fiber Bragg Grating (FBG) sensor can be considered as an example of an optical fiber sensor [29]. Figure 2.13 demonstrates the FBG strain/

temperature sensor, which reflects a variation in light wavelength in response to a change in temperature and/or strain. FBG sensors are fabricated by inscribing nano structured Bragg gratings with a period of 'Λ' into the core of the optical fibers. The refractive index of the fiber is transformed according to the exposed light intensity. The periodic variation in the refractive index (n) is called a fiber Bragg grating. Depending upon the 'Λ' the FBG reflects particular wavelengths of light while transmitting all others. The reflected/ Bragg (λ_b) wavelength is given by equation (5).

$$\lambda_b = 2n\Lambda \tag{5}$$

The change in the temperature and/or strain alters both Λ and n of FBG resulting a change in λ_b. The change of λ_b of an FBG due to temperature and/or strain is given by equation (6).

$$\frac{\Delta\lambda_b}{\lambda_b} = (1 - p_e) * \epsilon + (\alpha_\Lambda + \alpha_n) * \Delta T \tag{6}$$

where p_e is the strain-optic coefficient, ε is the applied strain on the grating, α_Λ is the thermal expansion coefficient, α_n is the thermo-optic coefficient. The first part of the equation6 is due to the applied strain and second part is a function of temperature.

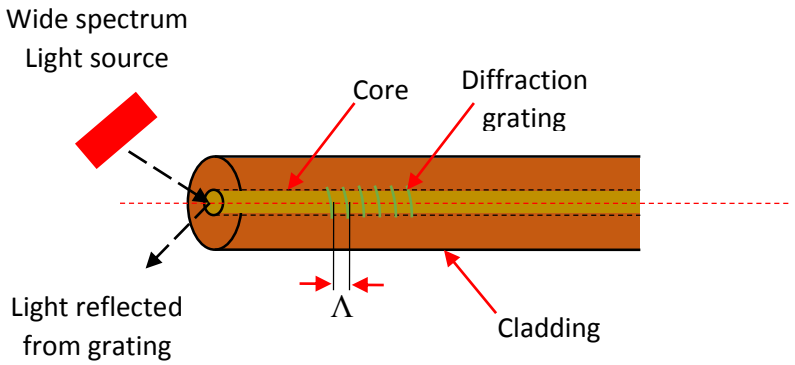

Figure 2.13. Fiber Bragg Grating sensor [29].

2.4.4 Thermal Sensors

In thermal sensors, the input stimulus is proportional to the measured temperature or heat of the sensor. The concept of thermal sensor can be explained using a bimetal strip based thermostat (shown in Fig. 2.14) which is used to control the room temperature [30]. Bimetal strip consists of two metals wielded or riveted together which curves when exposed to a change in temperature as the two metals have two different thermal expansion coefficients. The inner metal (orange color) is chosen in such a way that its thermal expansion coefficient is greater than the outer metal (blue color). When the sensor is exposed to heat, the inner metal expands more compared to the outer metal, resulted in an outward curve opening the connection between the bimetallic strip and contacts. This type of sensor is often found in thermostats used to control and maintain the given temperature of a room.

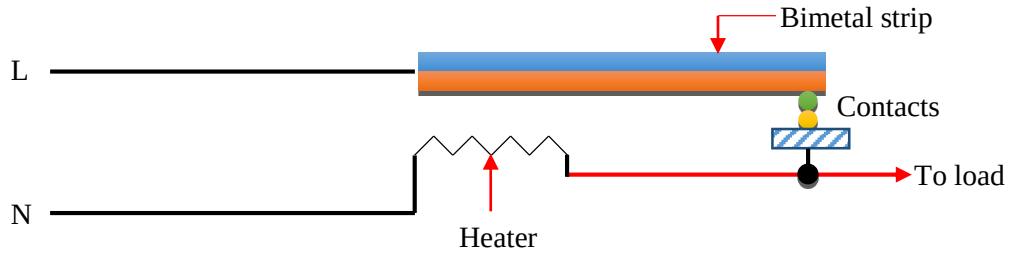

Figure 2.14. Bimetallic based thermostat [30].

2.4.5 Chemical/Biological Sensors

A chemical/biological sensor generates the output signal with response to input chemical or biological stimulus. Chemical sensors and biological sensors can be distinguished by their sensing layers. For the biosensor, the sensing layer is usually an antibody or an enzyme. Alternately, chemical receptors from the sensing layer for chemical sensors. A basic schematic of a transistor based chemical/biological sensor is shown in Fig. 2.15 [31]. The channel of the transistor is directly exposed to the

chemical/biological stimulus. The absorption of the stimulus changes the conductance of the semiconducting layer by doping it. The transistor in turn changes its output characteristics as a response to the input stimuli.

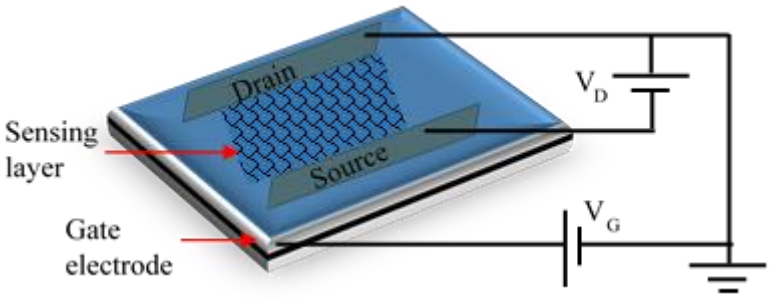

Figure 2.15. Schematic of a chemical/biological sensor [31].

2.5 Electrochemical Sensors

An electrochemical sensor is a device that transforms the information regarding input chemical stimulus, such as chemical identification and quantification, to a measurable signal. The first known electrochemical sensor reported was a glass electrode in 1906 by Cremer [32]. Electrochemical sensor using the enzymes was first proposed by Clark and Lyons in 1962 [33]. In the modern world, electrochemical glucose sensors play an essential analytical role in the diabetic monitoring for the patients. Commercial applications of electrochemical sensor have increased drastically from the mid-1980s with introduction of strips for self-monitoring blood glucose [34]. In addition to glucose monitoring, studies on electrochemical sensors are also reported for heavy metal detection, drug detection and other defense applications [35-40].

Electrochemical sensors usually consist of a special electrode surface at which the charge transportation or chemical reaction can take place. Often, these electrodes are modified or treated to increase the sensitivity. A traditional electrochemical cell is

shown in Fig. 2.16 [41]. The cell consists of collection of electrodes, analyte or electrolyte and measuring system. Usually there are three electrodes in the electrochemical cell namely, sensing or working electrode (WE), auxiliary or counter electrode (CE) and reference electrode (RE). The chemical reaction or charge transfers takes place at the sensing electrodes. The CE is used to improve the operation of the electrochemical sensing system by modifying the error potentials introduced by polarizing the WE. The RE helps to monitor the potentials generated by the other electrodes and electrolyte. The electrochemical cell can be operated in various configurations, depending on the electrical measurement characteristics (impedance, potential, capacitance, current, etc.).

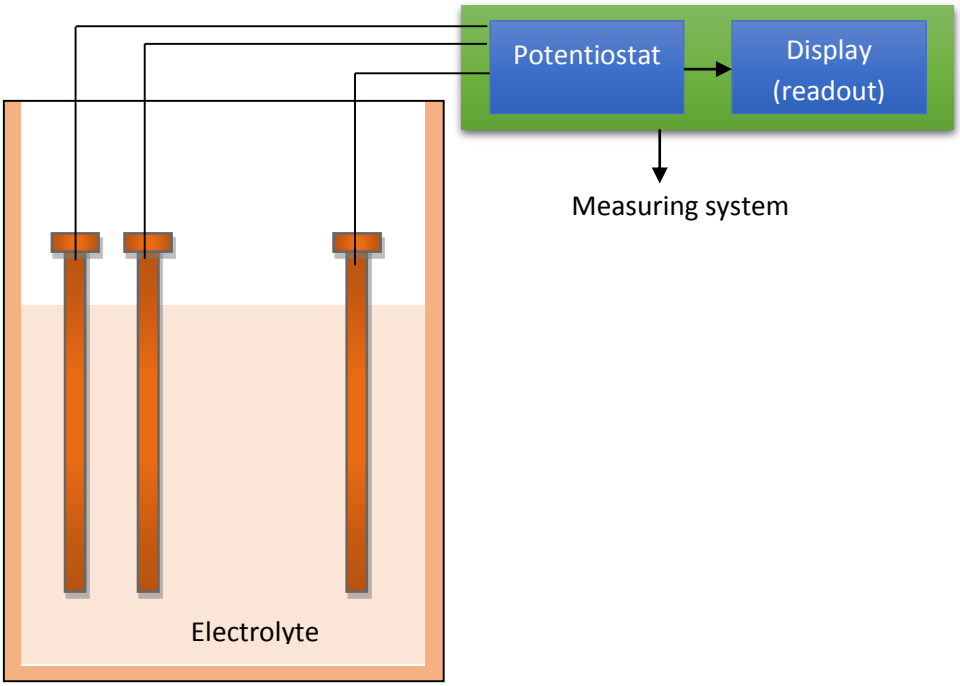

Figure 2.16. Three electrode electrochemical sensors system [41]

2.5.1 Electrochemical Sensor Configurations

Based upon the transduction principle of electrochemical sensors, the cell is configured as Impedance based, amperometric and voltammetric sensors. A brief discussion for each of the configurations is given below.

2.5.1.1 Impedance Based Electrochemical Sensors

Impedance based electrochemical sensors are configured with the principle of measuring change in impedance of the sensitivity layer with respect to the chemical reaction taking place. The measured change in impedance is proportional to the recorded voltage which shows the principle of Ohm's law. Electrochemical impedance spectroscopy (EIS) is one of powerful technique used for measuring the response of the impedance based electrochemical sensor. EIS is known to characterize the detailed properties of material at the surface of the conducting electrodes. EIS works on the principle of measuring impedance by applying a small amplitude sinusoidal signal. The resultant measured impedance of the system has a real and an imaginary parts whose resultant graph is termed as Nyqusit plot or Cole-Cole plot. An example of the Nyqusit plot is shown in Figure 2.17 (a) [42-45]

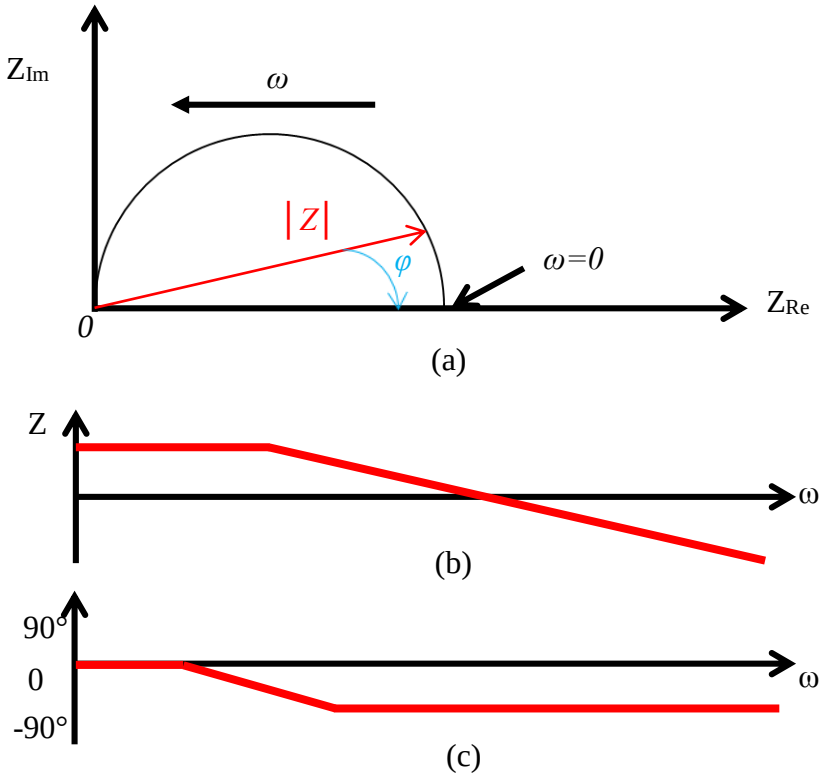

Figure 2.17. Output of EIS (a) Nyquist plot (b) Impedance Bode plot and (c) phase Bode plot

Impedance in any Nyquist plot is represented by a vector of length $|Z|$. The angle between the impedance vector and x-axis is equal to the phase of the system. The diameter of the semicircle in Nyquist plot gives out the real impedance of the system. The main drawback of the Nyquist plot is that it does not depict the frequency of the system. Another conventional way of representing the data from EIS is Bode plots in which the impedance and phase of the system is plotted with respect to operating frequency. An example of a Bode plot for magnitude and phase are shown in Fig. 2.17 (a) and Fig. 2.17 (b), respectively.

2.5.1.2 Amperometric Sensors

In an amperometric sensor, the resultant current from the oxidation and reduction reaction at the interface of working electrode and electrolyte is measured and analyzed. In these sensors, the voltage applied is always constant. Equation (7) shows theoritically calculated current in amperometric sensing. [46].

$$i_l(t) = nFAC\sqrt{D/\pi t} + \frac{nFACD}{r} \tag{7}$$

where n is number of electrons transferred in the electrochemical reaction, *A* is area of electrodes, *F* is Faraday constant, *D* is diffusion coefficient, *C* is concentration of target electrolyte, *r* is radius of electrode, and *t* is time. Equation 7 consists of two parts in which first part represents the transient current and second part represents the steady state current. An amperometric based glucose sensor is the simplest example of amperometric sensor, which consists of a KCl electrolyte with glucose oxide as a biocatalyst, a platinum cathode and a silver/silver chloride reference electrode. The typical schematic of an amperometric sensor is shown in Fig. 2.18. A constant voltage is applied between the cathode and RE which is responsible for the current in the cell.

The measured current is proportional to the concentration of the catalyst in the electrolyte.

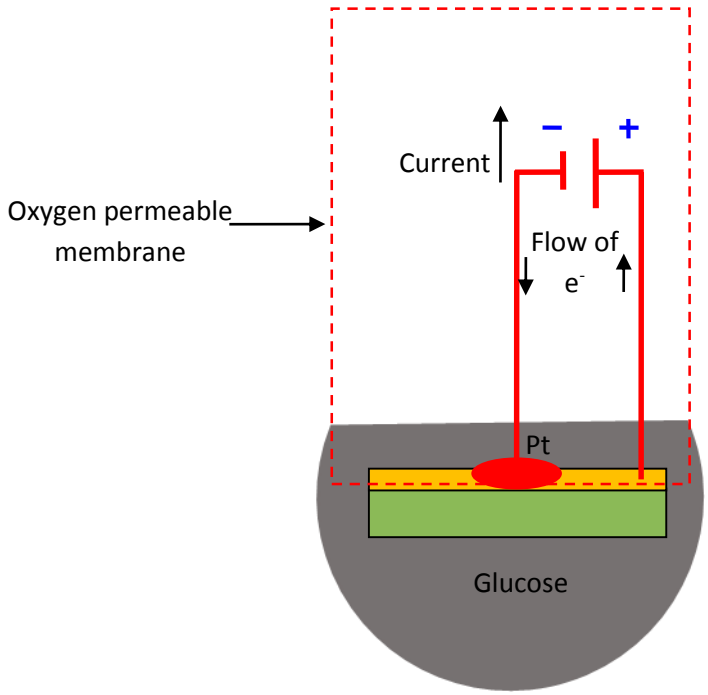

Figure 2.18. Typical schematic of amperometric sensors [46]

2.5.1.3 Voltammetric Sensors

Voltammetric sensors work on the principle of measuring open circuit voltage between the WE and CE. The change in the voltage is due to the oxidation and reduction cycles. The voltage on the WE is altered to see the oxidation and reduction cycle whereas the potential of the reference electrode is kept constant throughout the experiment. The materials used for RE are silver/ silver chloride (Ag/AgCl), saturated calomel electrode (SCE) or standard hydrogen electrode (SHE). The materials used for the WE mainly depend upon the target molecule, which can be one of the following: carbon, graphite, gold, platinum or a metal coated with a mercury film. A suitable material for CE electrode is platinum or silver.

Voltammetry is typically studied using a cyclic voltammetry (CV) technique, which is an important electrochemical method widely implemented to study the oxidation and reduction processes of the electrochemical species [47]. A DC increasing ramp followed by DC decreasing ramp is applied as input to the cyclic voltammetry. The starting potential of the ramp is the point where there is no reaction taking place (E_1). The voltage is then increased to E_2 which is after the reduction or oxidation potential of the target molecule. From this point the potential is swept back to E_1 as shown in Fig. 2.19. Depending on composition of the analyte the scan direction is negative or positive. The negative scan direction is termed as the forward scan where as the positive scan is defined as the reverse scan.

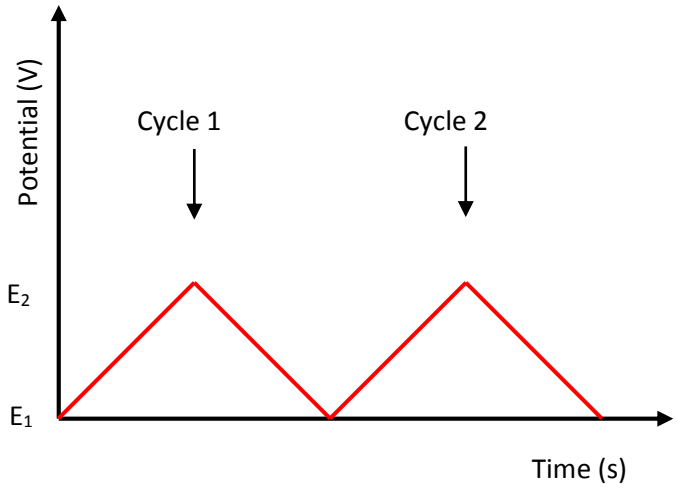

Figure 2.19. Input of the cyclic voltammetry

The slope of the ramp signal is called the scan rate of the cyclic voltammetry which is a crucial parameter in the experiment as it is proportional to the intensity of the current peaks. [48] Usually the scan rate is kept constant throughout the experiment. For analysis, the measure current is plotted against the applied voltage. Figure 2.20 shows the typical output of the CV technique for the redox couple of A^+/B. First, when the voltage is at E_1 potential, the sample is in the form of A^+. Voltage from E_1 was scanned in the negative direction towards to E_2. This scan

usually injects the electrons into A^+ which reduce to B. This process will continue until the A^+ molecule is completely reduced to B. The current in the cell will be minimum resulting in a reduction peak. When the potential reaches E_2, the reverse sweep will start, which leads to positive current. The current keeps increasing until B completely oxidizes to A^+ and hence the oxidation peak is formed. Parameters that need to be considered in CV are reduction and oxidation peak potentials which helps in determining the unknown substance in a given analyte. In an idea redox reaction, the oxidation peak is nearly equal to the reduction peak showing the complete reversibility of the process [49].

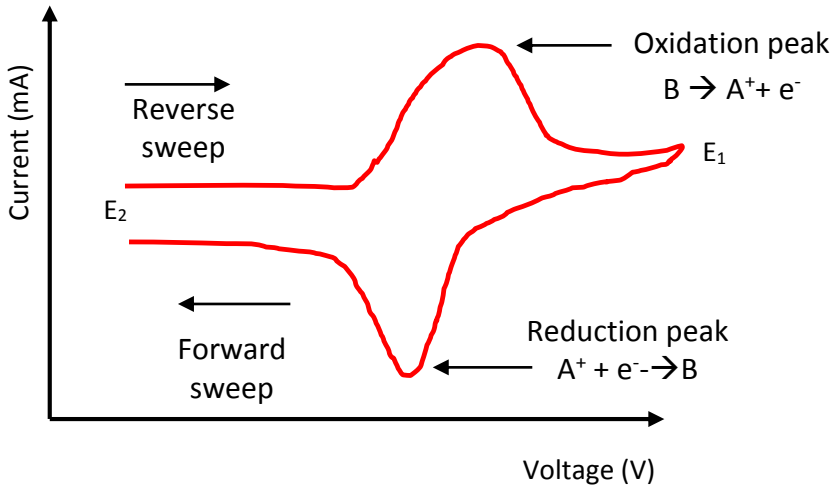

Figure 2.20. Output of cyclic voltammetry

The other types of voltammetric techniques apply pulsed voltage instead of ramp which are termed as pulse voltammetric techniques. Depending upon on the applied pulse, voltammetry can be performed in three different configurations as differential pulse voltammetry (DPV), normal pulse voltammetry (NPV), and square wave voltammetry (SWV). The applied inputs and expected outputs of all the pulse voltammetric configurations are shown in Fig. 2.21. A series of increasing amplitude potential pulses are used as an input (shown in Fig. 2.21 (a)) to NPV [50]. The current in the cell is measured at the end of each pulse. DPV also uses the series of increasing

amplitude potential pulses. However, the base line is not the same for all the pulses in DPV. Moreover, DPV measures current at start and end points of each pulse. The difference of both the currents is plotted with respect to voltage [51]. SWV uses a symmetrical square-wave pulses superimposed on a staircase waveform (shown in Fig. 2.21 (d)) as input. The difference of the forward and reverse currents are measured and plotted against redox potential. The height of the current peak is directly proportional to the concentration of the electrolyte. SWV rejects background current and has been proven to have excellent selectivity compared to other voltammetric techniques [52].

2.6 Humidity Sensors

The term humidity refers to the percentage of water content present in an object or any material and is detected by using hygrometer, invented by Sir John Leslie [13]. Over the past decade, tremendous attention has been laid on the development of humidity based sensors, owing to their numerous applications in the semiconductor industry, environmental monitoring, automobile industry, and medical field [53-55]. In the semiconductor industry, it is critical to maintain a desirable range of humidity while fabricating highly sophisticated integrated circuits [56]. Environmental application include monitoring greenhouse effect, cereal storage, measuring soil moisture content in the agriculture, etc.. Humidity sensors are also used in the automobile industry for motor assembly lines, air conditioning and rear defoggers [57]. Incubators, sterilizers, respiratory equipment and pharmaceutical processing all use humidity sensors as an indirect measure of an expected outcome [58]. Based on the mode of detection, humidity sensors are classified as optical humidity sensors, oscillating humidity sensors, thermal conductivity humidity

sensors, resistive or capacitive humidity sensors. The mechanisms employed by these humidity sensors are briefly below.

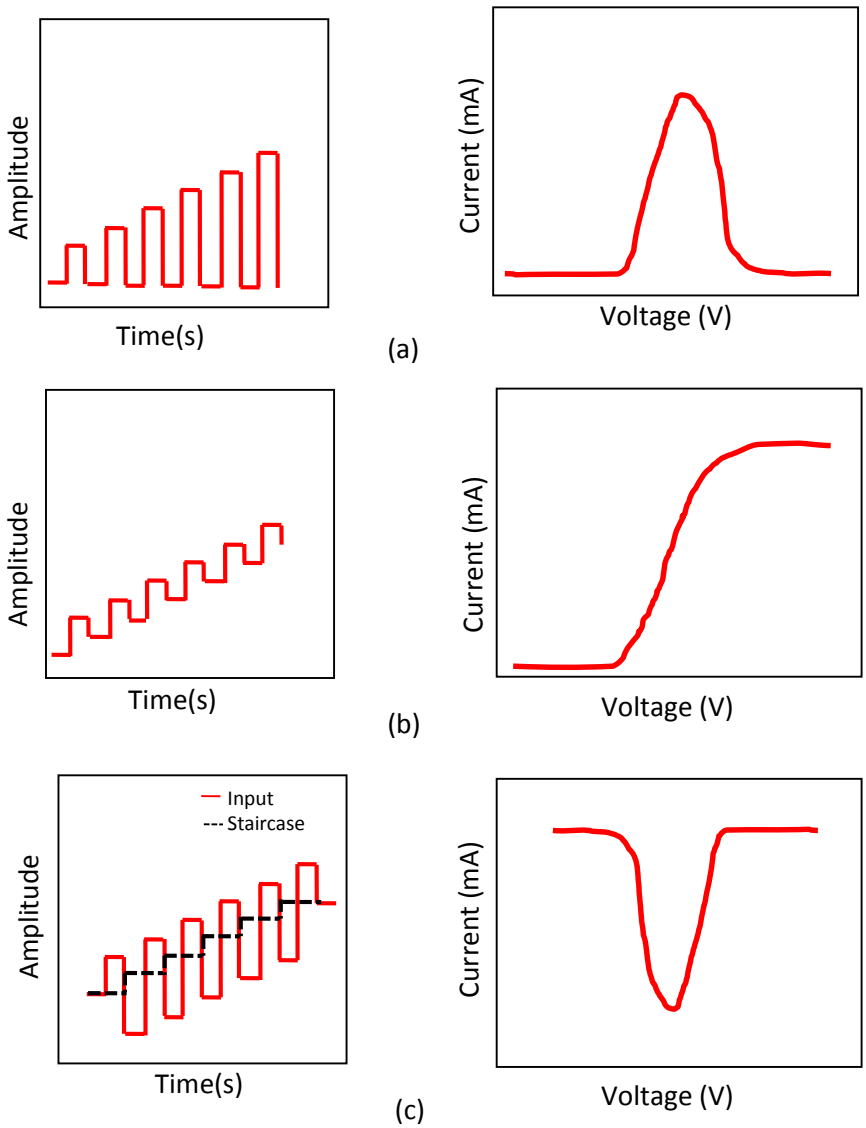

Figure 2.21.Input and expected output of pulse voltammetric configurations
(a) normal pulse voltammetry, (b) differential pulse voltammetry and
(c) square wave voltammetry

2.6.1 Optical Humidity Sensors

The optical method of measuring humidity is known to minimum hysteresis [13]. However, the cost involved to measure humidity with this method is considerably higher as compared to other methods. A chilled-mirror hygrometer (shown in Fig. 2.22) is an example of an optical humidity sensor [59]. Light emitting

diodes (LED), photodetectors, a digital thermometer, sampled glass mirror, heat pump and optical balance are the main parts of chilled-mirror hygrometer. The bottom LED and photo detectors, placed at an angle of 45° with respect to the sampled mirror, are used to measure the reflectivity. The top LED and photo detector are used as a reference to compensate for drifts and maintain symmetry. The optical balance helps in maintaining the symmetry of the upper LED light path. Heat at the surface of the thin glass is controlled by a heat pump. In a dry environment, the mirror has the highest reflectivity. With an increase in humidity water droplets starts condensing on the mirror which gradually reduces the reflectivity. As a result, the current in the bottom photodetector is effected. Humidity measurement then can be obtained based on the photodetector current and thermometer readings.

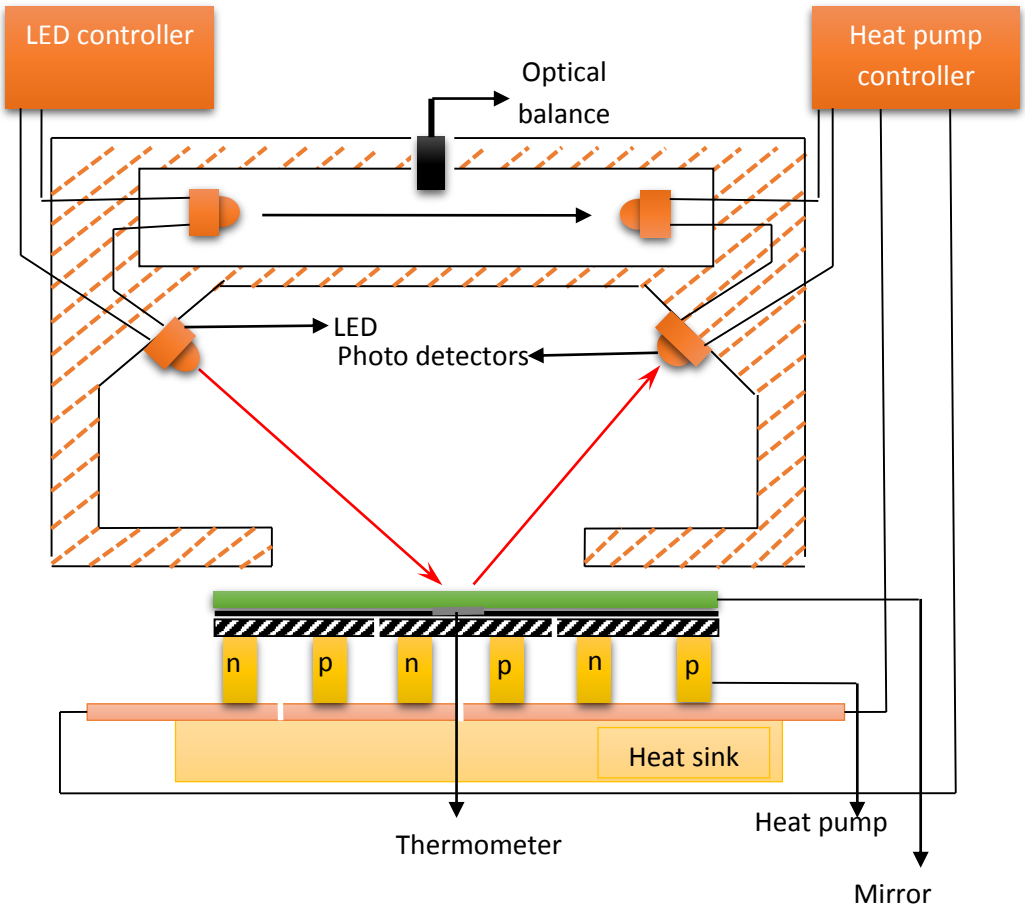

Figure 2.22. Chilled-mirror hygrometer [59]

2.6.2 Oscillating Humidity Sensors

Oscillating humidity sensors typically work with piezoelectric crystals. Hence, they can also be called as piezoelectric humidity sensor. The working of an oscillating humidity sensor is explained by considering the example of an oscillating hygrometer (shown in Fig. 2.23) [60]. An oscillating hygrometer measure the dew point based on the mass of a chilled quartz crystal, whereas optical hygrometers consider the reflectivity of a chilled plate. The temperature of the crystal is controlled by a Peltier cooler. The change in mass of the quartz crystal is proportional to the relative humidity and results in a change in the resonant frequency of the crystal from f_0 to f_1; where f_0 is initial resonant frequency and f_1 is new resonant frequency of the crystal.

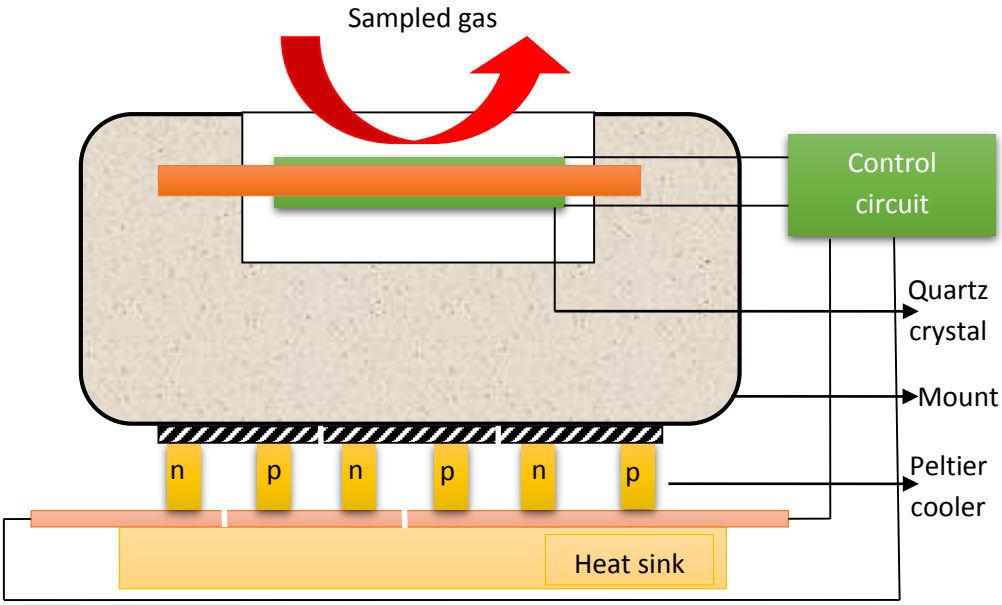

Figure 2.23. Oscillating hygrometer [60]

2.6.3 Thermal Humidity Sensors

Thermal humidity sensors employ thermistors as sensing elements. A schematic of the typical thermal sensor is shown in Fig. 2.24 [61]. Wheat stone bridge circuit is constructed with two normal resistors and two thermistors. The bridge is

powered with a known voltage source. The value of the resistors, R_1 and R_2, are chosen in such a way that the bridge is balanced in dry air. The thermistors are placed inside a closed chamber as shown in Fig. 2.24. The left thermistor is exposed to the environment whereas the right thermistor is sealed in dry air. When the thermistor 1 changes in resistance due to the inflow of air in left chamber, the bridge gets unbalanced and results in an output voltage that is a function of humidity.

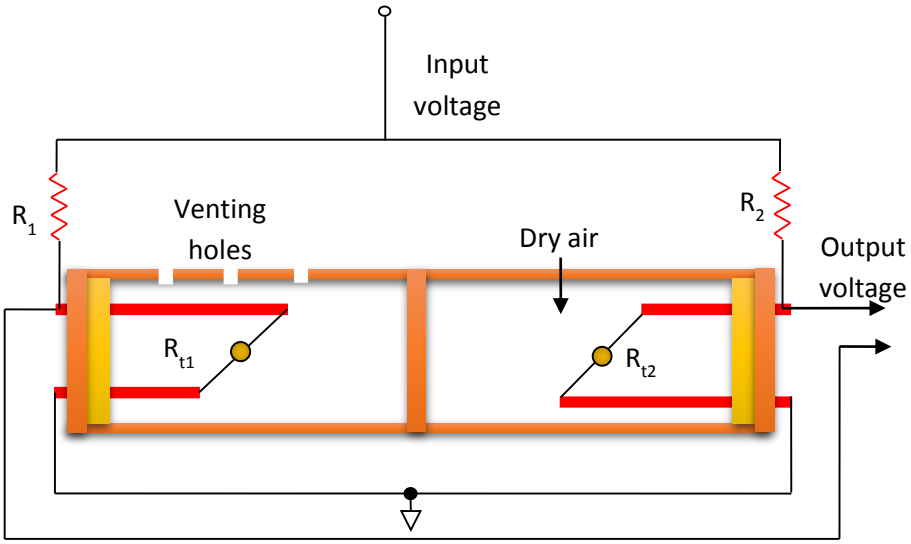

Figure 2.24. Thermal humidity sensors [61]

2.6.4 Resistive and Capacitive Humidity Sensors

Resistive and capacitive humidity sensors rely on changes in conductivity or dielectric constant of the sensing material with respect to relative humidity. Polyelectrolytes and ceramics are the usual materials used for resistive type humidity sensors. The materials suitable for capacitive type humidity sensors are porous silicon and hydrophobic polymers that are stable at high humidity conditions. Advancements in the microfabrication industry has lead to the miniaturization of humidity sensors. Capacitive and resistive sensors can be implemented as a coplanar structure, hence they requires a single side process for fabrication. Research has shown that capacitive and resistive sensors offers low power consumption and are compatible with most

interface circuits [62]. The typical schematic of resistive and capacitive humidity sensors using a coplanar structure is shown in Fig. 2.25

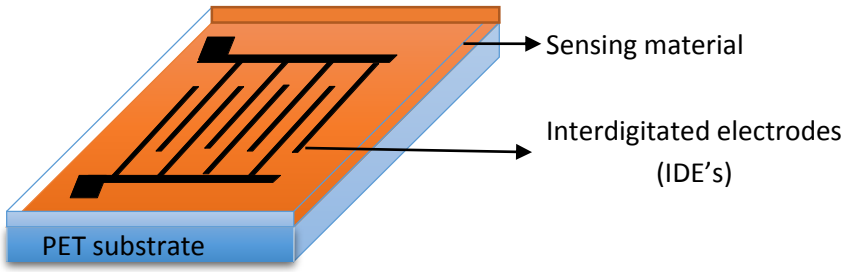

Figure 2.25. Resistive and capacitive humidity sensors [62]

2.7 Sensors with Electrical Output

Almost all the sensors in the modern world have been designed to have electrical signals as their output. Sensors with an electrical output can be classified into active and passive sensors. A passive sensor does not need any excitation signal and directly generates an electrical signal; whereas, active sensors are excited with an additional energy source to generate an electrical output in response to the input stimulus. Examples of the active sensors are ultrasonic sensors [63-67] and radar [68-73]. Photodiode [74-78] and thermocouple [79-82] sensors are typical examples of passive sensors. Most of the passive sensors are direct sensors that don't require an additional transducer for generating the required output. For instance, consider a thermistor whose output voltage is a function of temperature. The energy used to generate this voltage is from temperature [83].

Sensors with an electrical output have a significant advantage over other types of sensors in that they can be embedded them into smart sensing systems, which have

numerous applications in the present day [84-95]. Moreover, the output responses of the sensors can also be easily processed and data can be stored in memory.

2.7.1 Fabrication of Sensors with Electrical Output

The first known electrical sensor was a copper resistor based temperature sensor developed by Wilhelm von Siemens in 1860 [96]. The sensor industry has been constantly growing following advancements in electrical engineering and material science. However, the most drastic change in the sensor industry has occurred with the advent of semiconductor technology in the 1960s [97-106]. Lithography based techniques such as photolithography [107-111], x-ray lithography [112-117], electron beam lithography [118-123] and ion beam lithography [124-1280] have been used for the patterning fabrication of sensors. All these techniques are subtractive process and have complex fabrication steps [129]. Advancements in research of alternate methods of electronics fabrication have demonstrated that traditional printing methods may be used for manufacturing sensors [130-134].

2.8 Printed Electronics

Over the past decade, printed electronics (PE) has revolutionized the manufacturing sector as it is an additive process [135]. PE offers various advantages, such as reduction of material wastage, processing at ambient conditions and capable of printing on large areas [136-138]. The advantages overcome the disadvantages of conventional silicon (Si) based technology, such as high-vacuum and high-temperature deposition processes along with sophisticated photolithographic patterning techniques [139]. In addition, the efficient use of resources during fabrication and mechanical flexibility of printed electronic devices make them potential candidates for cost efficient, flexible and lightweight products. Some

applications of PE include, but are not limited to, flexible radio frequency identification (RFID) tags [140-144], organic light emitting diodes (OLEDs) [145-148], flexible displays [149-153] and sensors [154-157].

2.8.1 Types of Printing

PE uses high throughput printing techniques, such as roll-to-roll gravure, flexography, screen and inkjet printing, along with solution processed electronic materials (conductive, semiconductive and dielectric inks) for layer on layer fabrication of electronic sensors, devices and circuits. A comparison 0f the printing techniques is shown in Table 2.1 [150].

Table 2.1. Comparison of traditional printing techniques [158-159].

	Gravure	Inkjet	Flexography	Screen
Resolution	15 µm	15 µm	20 µm	30 µm
Printing speed (m/min)	8-100	0.02-5	5-180	0.6-100
Ink film thickness (µm)	0.02- 12	0.01-0.5 µm	0.17-8	3-30 µm
Image carrier	Gravure cylinder	Virtual carrier	Flexo plate	Stencil

2.8.1.1 Gravure Printing

Gravure printing offers significant advantages through its high quality printing, high print speeds, variable ink film thickness, use of low viscosity inks and simplicity of its process in transferring the ink onto the substrate. Gravure printing has the ability to transfer larger amounts of inks to larger areas at high speeds with nominal distortion. Gravure printing can be operated at high printing speeds in comparison to other conventional printing processes. The gravure cylinder (image carrier), doctor blade, impression roller and ink fountain are the main components of the typical gravure printing process as shown in Fig. 2.26. The impression roller is

made of rubber. Steel is the material used for the doctor blade. Chromium and copper coated steel is used for making the gravure cylinder. The image carrier is etched electromechanically, chemically or by laser to form an image area, which is usually made up of small gravure cells. When the gravure cylinder rotates in the ink fountain the small cells get filled with ink. The doctor blade wipes off the excess ink that remains on the surface of the cylinder. The angle of the doctor blade also plays a key role in printing. Transferring the ink from the cells onto the substrate is assisted by the impression cylinder [160].

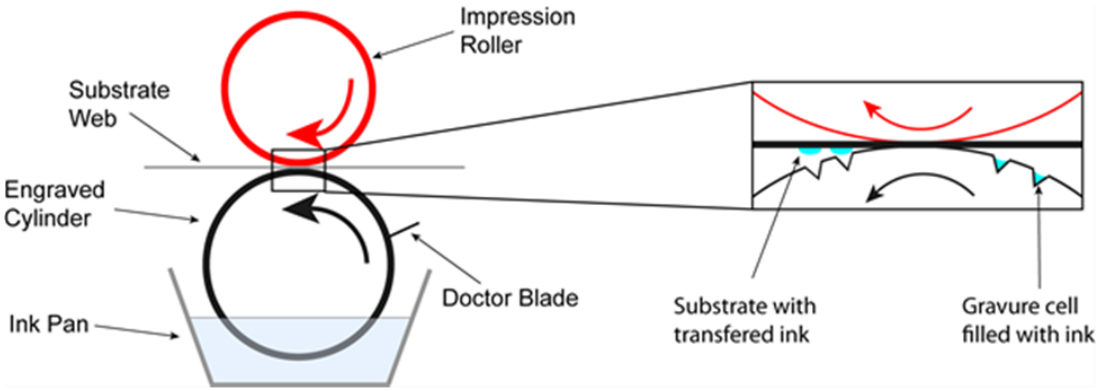

Figure 2.26. Typical gravure printing process.

2.8.1.2 Flexographic Printing

Flexographic printing is known for depositing a wide range of thicknesses with the same resolution. This is because in the flexographic printing technique is an indirect printing process and can use the same nominal resolution plate with anilox rolls of different cell volumes. Impression cylinder, plate, anilox roller, doctor blade and inking unit are the main parts of the flexographic printing (shown in Fig.2.27). The material used for the doctor blade and anilox is usually stainless steel. The plate is made of either a photopolymer or rubber. The image areas of the plate cylinder are raised with respect to the surface of the plate. The anilox roller transfers the ink from

the inking unit, to the image areas of the plate cylinder. Transferring the ink from the image areas onto the substrate is assisted by the impression cylinder [160].

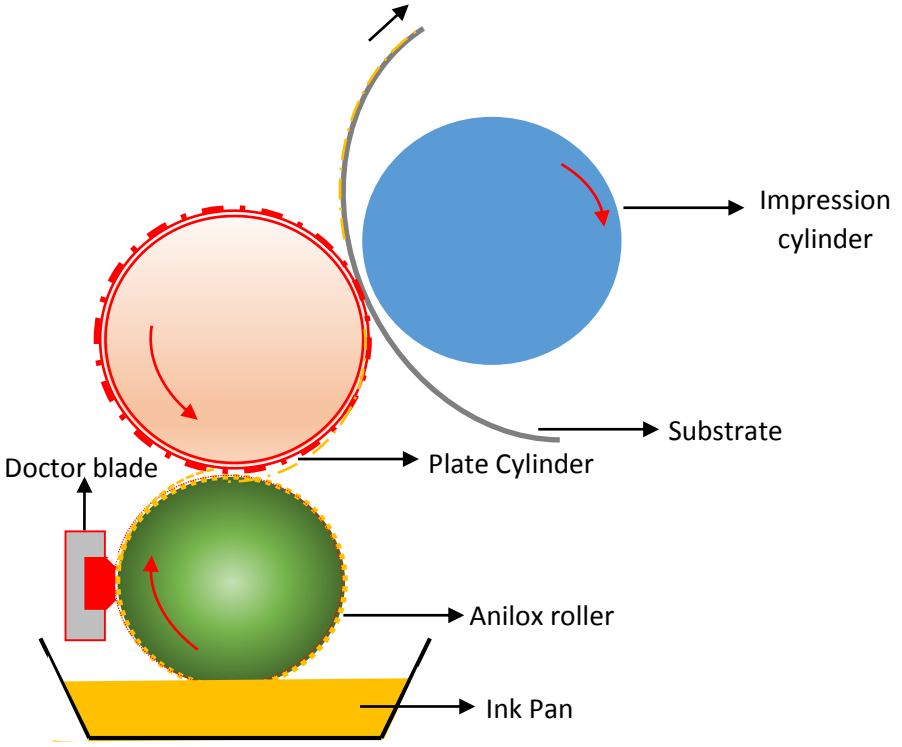

Figure 2.27. Typical flexographic printing process.

2.8.1.3 Screen Printing

Screen printing is known for depositing thicker films when compared to all other printing methods. It is a push through process. A squeegee and screen printing plate are the main components of the screen printing process. The typical screen printing process is shown in Fig. 2.28 (a). A screen printing plate (Fig. 2.28 (b)) consists of screen fabric, stencil and frame. The materials used for the screen fabric and stencil vary depending upon the use of solvents and cleaning agents. The frame is made of either aluminum or steel. Rubber is the usual material used for the squeegee. Ink is applied on top of the screen. The squeegee is used to sweep the ink on top of

the screen with high pressure. The ink passes through the screen and transferred onto the substrate [160].

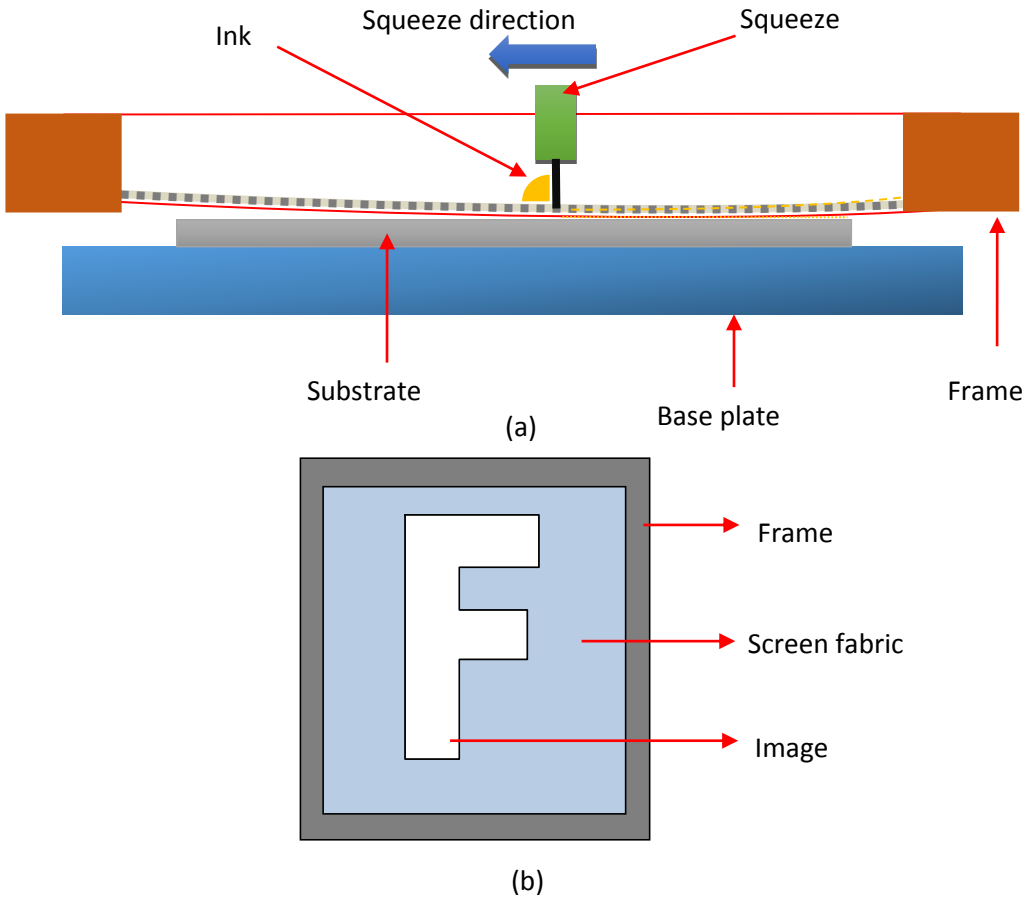

Figure 2.28. (a) Screen printing process and (b) screen printing plate.

2.8.1.4 Inkjet Printing

The main advantage of an inkjet printing process is the lack of a need for a physical mask or image carrier, using a direct deposition technique where a virtual digital image carrier exists on a computer. Inkjet printing is also known for depositing thin films. Inkjet is classified into continuous inkjet and drop on demand inkjet based on the ink transfer method. Drop on demand inkjet is further classified as thermal inkjet and piezo inkjet printing processes. A continuous stream of ink is generated in a continuous inkjet printing (Figure 2.29 (a)). The ink is deflected towards the substrate by use of voltage source. The non-deflected ink is fed back into the cartridge. Drop on

demand inkjet generates ink droplets with respect to image signals. Thermal (Figure 2.29 (b)) and piezo electric technique (Figure 2.29 (c)) are two methods used to generate ink droplets [160].

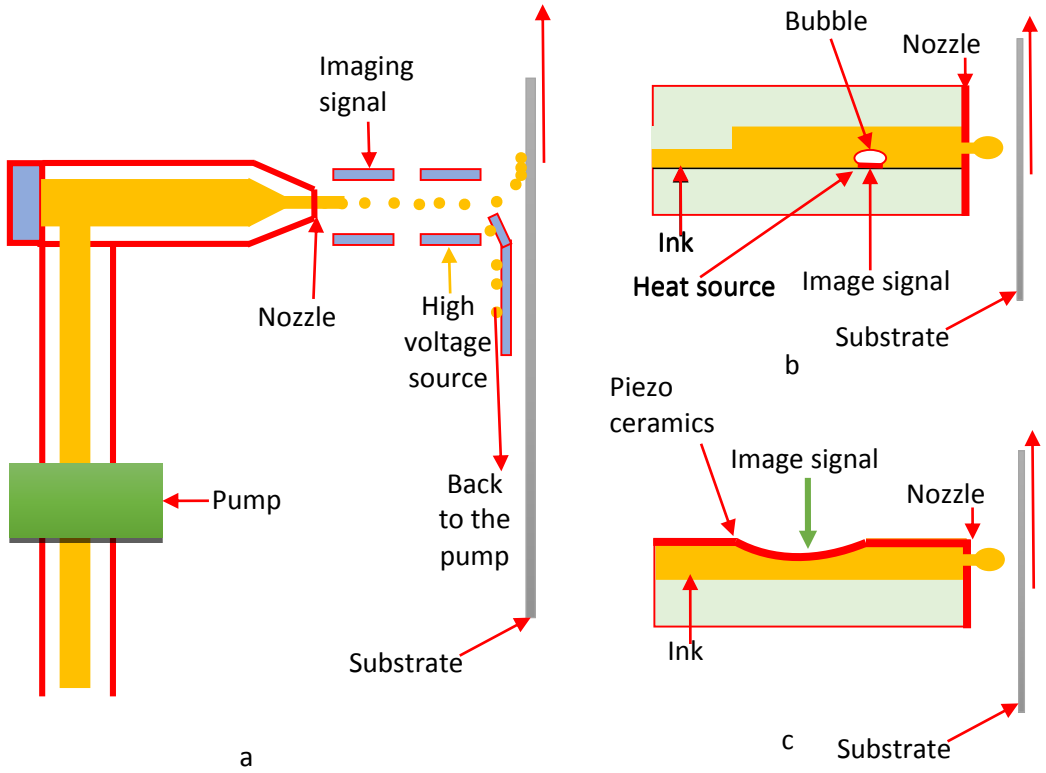

Figure 2.29. (a) Continuous, (b) thermal and (c) peizo electric drop on demand inkjet.

2.8.2 Challenges in Printed Electronics

Even though PE has addictive advantages, there are some challenges that needs to be addressed. To name a few, complexity of ink formulation, choice of print process and compatibility of the printed layers. Consistency, performance and yield are also challenges to be overcome for future PE applications. Another challenge that needs to be addressed in time is to achieve nano feature sizes approaching that of traditional Si based fabrication while retaining device functionality.

There are also challenges in the material selection including, but not limited to ink stability, printability, material lifetime, cost, wetting properties and solvent

compatibility with the substrate [161]. The relation between the surface energy of the substrate and surface tension of the ink is also crucial. As a rule of thumb, the surface energy of the substrate should be at least 10 units greater than the surface tension of the ink. Moreover, contact angle of the ink on the substrate should be less than 90° for proper wetting. The coffee ring effect, due to uneven evaporation of the solvent, is also an important factor to be considered. This can be overcome by mixing solvents of different boiling points and surface tensions [162]. Some of the other critical issues that need to be considered in PE are (a) registration for multi-layered devices, (b) physical compatibility such as step coverage and work function and (c) curing of inks within thermal tolerances.

2.8.3 Printed Sensors

In 2013, the market for printed sensors was at $6.28 billion. It is expected to reach $7.51 billion by the year 2020 [163]. The prominent examples of the printed sensors are humidity sensors, biosensors, temperature sensors and photo detectors. Figure 2.30 shows the relative market size of printed and flexible sensors in the year of 2024 [164]. Biosensors will have the biggest market share followed by hybrid sensors. According to IDTechEx, the two sensors viz., printed humidity sensors and biosensors used in this dissertation are predicted to have the highest compound annual growth rate (CAGR) of 75 % and 45 % in the next 10 years, respectively, as shown in the Fig. 2.31 [165].

PE is an additive process for fabrication of sensors. Sensors with coplanar structure will have an additional advantage, as they need only a single side fabrication process. Prominent examples of the coplanar sensors are electrochemical sensors [166-169] and thin film transistor based sensors [170-173].

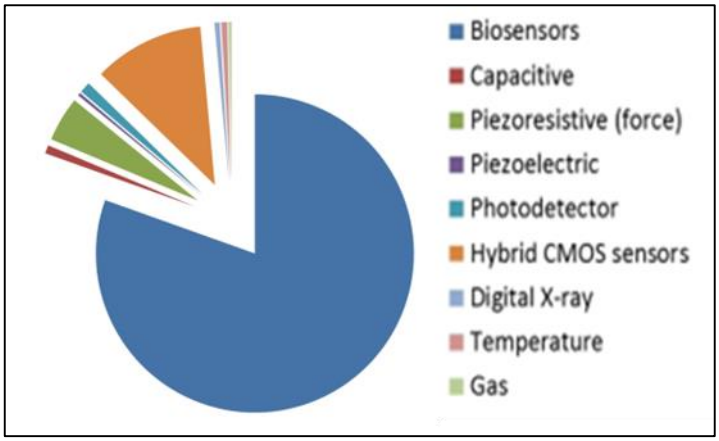

Figure 2.30. Relative market share of printed sensor in 2024 [164].

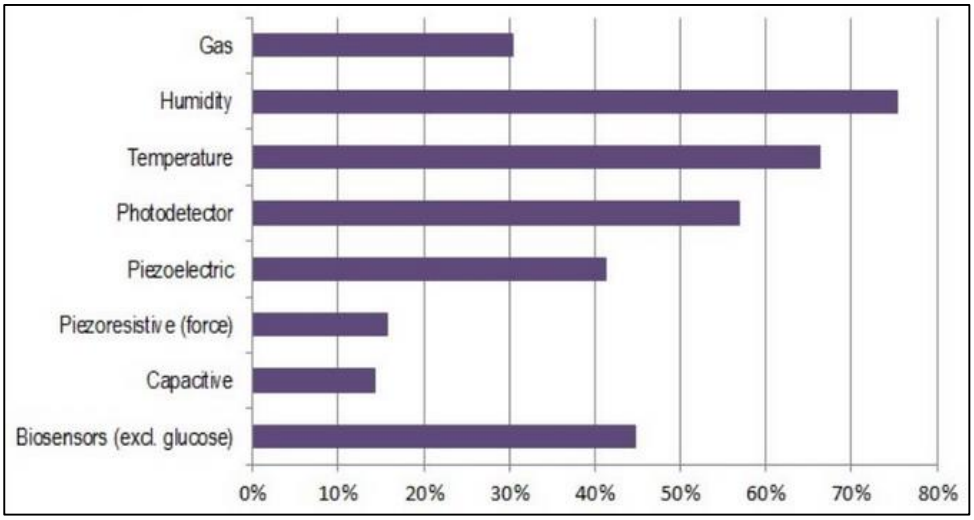

Figure 2.31. Printed sensors CAGR 2015-2025 [165]

2.9 Introduction to Organic Electronics

The era of organic electronics was started with the discovery of conductive properties in polyacetylene polymer by Heeger, MacDiarmid, and Shirakawa in 1977 which later won them a Nobel Prize in chemistry for the year 2000 [174]. Organic electronics have gained a huge interest as they are low cost materials and allow fabrication at low processing temperatures resulting in cost efficient electronics. Moreover organic polymers can be deposited using various conventional methods, such as thermal evaporation, vapor deposition, and spin coating, and traditional print methods like screen, gravure, inkjet and flexographic printing process [175-176].

Organic electronics are known to be fabricated on both rigid and flexible substrates such as paper, fabric, plastic and polymer substrates enabling the various applications in defense, communication and consumer industries [177-179].

2.9.1 Organic Semiconductors

In traditional semiconductor industry, silicon is an intrinsic semiconductor as it has same number of holes and electrons. Silicon can become a p-type or n-type extrinsic semiconductor when it is doped with group III or group V materials from the periodic table, respectively. However organic semiconductors favor only one type of charge carrier either a hole (p-type) or an electron (n-type) transporting depending upon their molecular chemistry. Pentacene (Fig. 2.32 (a)) and Perfluoropentacene (Fig. 2.32 (b)) are prominent examples of p-type and n-type organic semiconductors, respectively [180]. In pentacene, the hydrogen atoms around the core molecule are less electronegative compared to the carbon. These hydrogen atoms give free electrons to the carbon resulting in an electron rich environment at the carbon core. Due to this high density of electrons, the molecule helps in positive charge carrier transport [181]. Perfluoropentacene is a derivative of pentacene in which hydrogen atoms are replaced by electronegative fluorine atoms. In this case, due to the higher negative electron density of fluorine atoms carbon will become electron deficient resulting an n-type semiconductor [182].

The properties of an intrinsic semiconductor are defined by the highest occupied molecular orbital (HOMO) (valance band p-type semiconductor) and lowest unoccupied molecular orbital (LUMO) energy (conduction band) level rather than doping concentration [183-184]. HOMO and LUMO levels were considered for designing the organic electronics. Ideally, these levels should be matched with the

work functions of the contact metals i.e., the difference between work function of the contact metal and semiconductor should be very small, to have a minimum barrier for

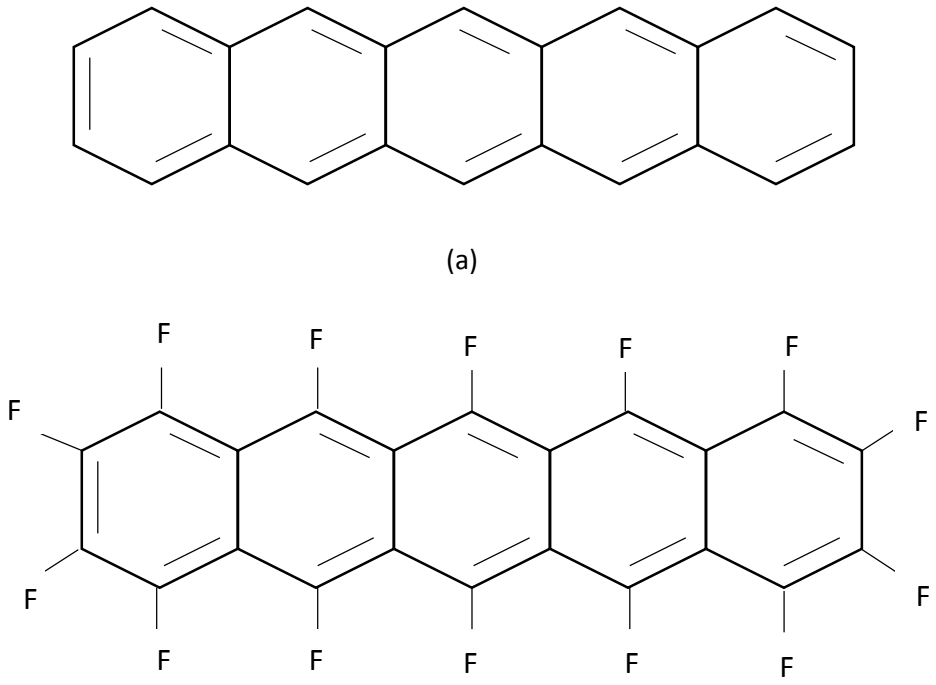

Figure 2.32. Example of two organic semiconductors, (a) Pentacene (b) Perfluoropentacene

charge injection [181]. For p-type semiconductors HUMO energy levels should be matched while for n-type LUMO energy levels should be matched. Figure 2.33 shows the HOMO and LUMO levels of the pentacene semiconductor. Pentacene has a HUMO energy level of 5.30 eV which is typically high for most of the metals. Gold with work function of 5.1 eV is one of the best choices for charge injection. The Fermi level of the gold is close to the HOMO level of the pentacene resulting in lower barrier height [185]. As per studies, metals with lower work function react and form a thin insulating oxide layer on the surface of the electrode [186].

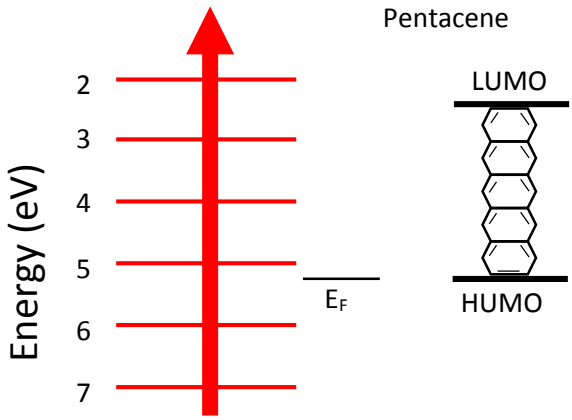

Figure 2.33. Energy level diagram of pentacene with HUMO and LUMO levels.

2.9.2 Organic Thin Film Transistors

In OTFTs, the current in conductive channel between source and drain electrodes is controlled by the voltage applied on the gate electrode. OTFT's are usually fabricated in four different configurations, such as bottom-gate bottom-contact (Fig. 2.34 (a)), bottom-gate top-contact (Fig. 2.34 (b)), top-gate top-contact (Fig. 2.34 (c)) and as top-gate bottom-contact (Fig. 2.34 (d)). For top gate structures, the first semiconductor is deposited onto the substrate, whereas for bottom gate structures, the gate conductive electrodes are deposited onto the substrate. The major difference between the top-contact and bottom-contact is the sequence of depositing drain-source electrodes and semiconductor. According to the previous research, the bottom contact devices have lower 'off' currents and better overall working characteristics when compared to the top contact devices [187].

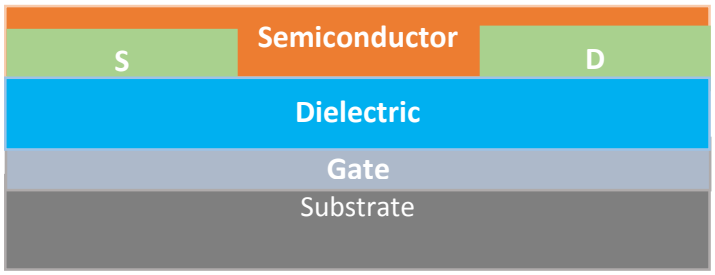

(a)

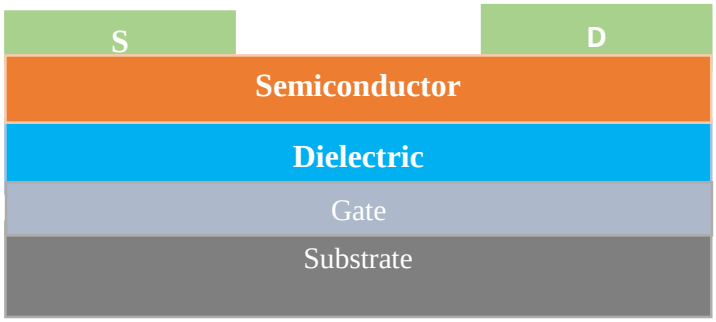

(b)

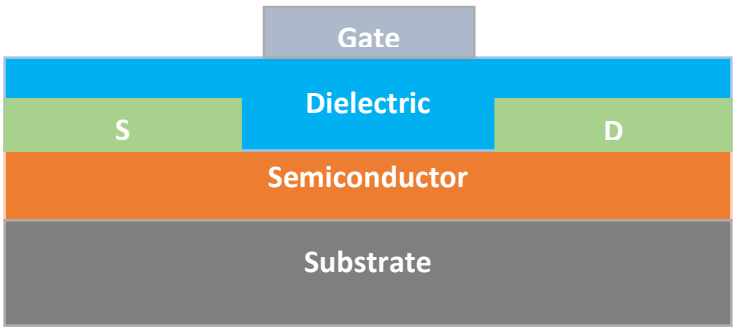

(c)

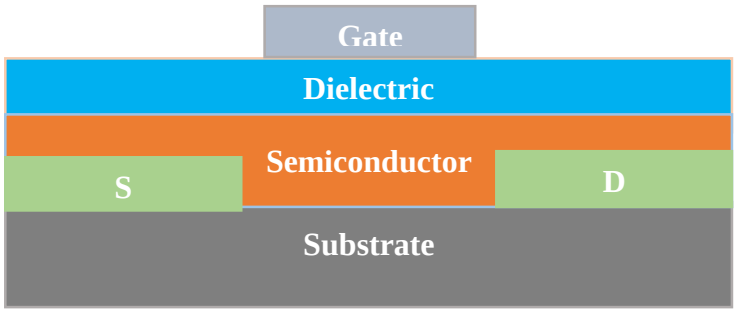

(d)

Figure 2.34. (a) bottom-gate, bottom-contact OTFT configuration, (b) bottom-gate, top-contact (c) top-gate, top-contact and (d) top-gate, bottom contact OTFT configurations

Unlike traditional TFTs, the majority of OTFTs works in accumulation mode i.e., there is no current between the source and drain electrodes at zero gate voltage. Current in the semiconductor layer increases with the gate voltage as the gate electrode charges are accumulated in the semiconducting layer forming a channel for the flow of current. This can be explained by considering an energy level diagram of pentacene based p-type OTFT (shown in Fig. 2.35) [188]. When there is no applied drain to source voltage (V_{DS}) and gate bias (V_{GS}-V_T (Threshold voltage of OTFT)), there is no conduction in the semiconductor channel as shown in Fig. 2.35 (a). If only V_{DS} is applied, then there will be minimal conduction which can be defined as an intrinsic conductivity of the semiconductor. In the case of p type semiconductors, application of gate bias increases the hole accumulation in the semiconducting layer near the interface (shown in Fig 2.35 (b)). This is because the barrier between the HOMO of semiconductor and metal Fermi level is decreased. As the V_{DS} increases to a more negative value, the charge carriers in the semiconducting channel allows current to flow through the channel, which is directly proportional to the applied V_{GS}. The channel modulation in the OTFT with respect to applied V_{GS} and V_{DS} is shown in Fig 2.36. At lower V_{DS} the current follows the Ohm's law i.e., current in the channel is proportional to the applied V_{GS} and V_{DS}. This is called the linear or active region of the OTFT (Fig 2.35 (a)) in which drain to source voltage is less than the gate bias ($V_{DS}<<V_{GS}$ -V_T). As the V_{DS} approaches gate bias then a pinch-off of the channel carrier density occurs (Fig 2.35 (b)) ($V_{DS}\approx V_{GS}$ - V_T). Further increment of V_{GS} results in channel current independent of the V_{DS} (Fig 2.35 (c)). At this point, OTFT enters the saturation region ($V_{DS}>>V_{GS}$ - V_T) [189].

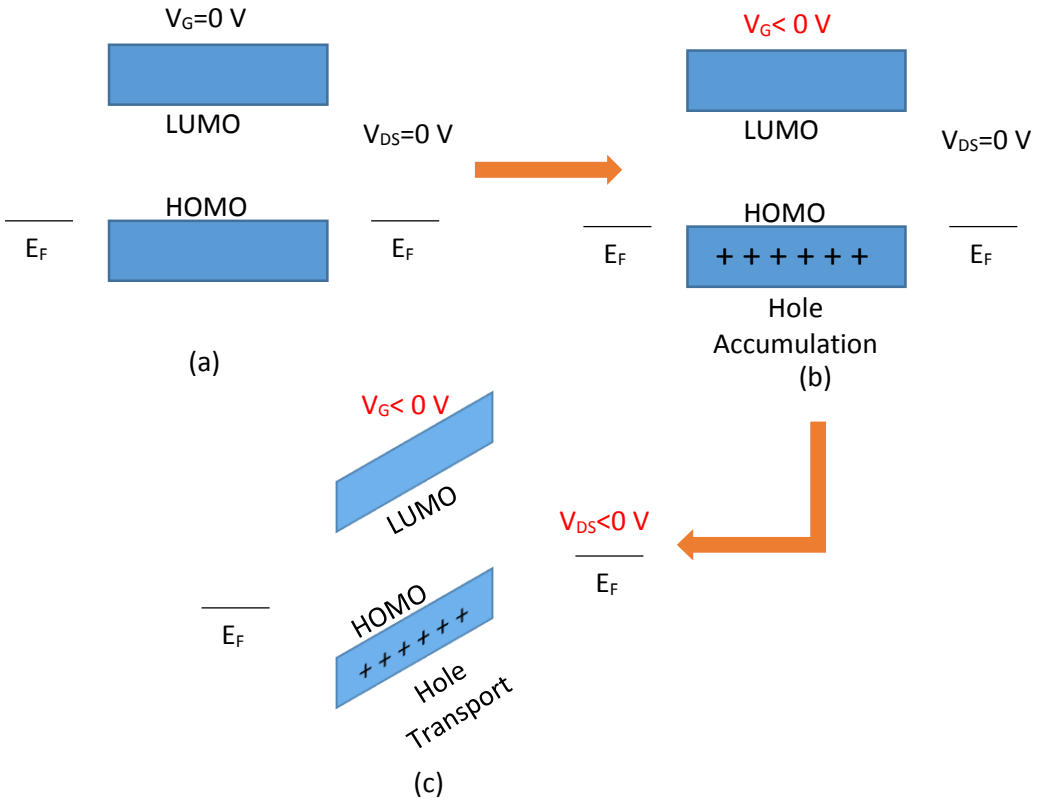

Figure 2.35. (a) Energy level diagram for TFT operation, (b) hole (positive charge) accumulation in the semiconducting channel due to $V_{GS} < 0$, (c) hole transport is achieved as the $V_{DS} < 0$

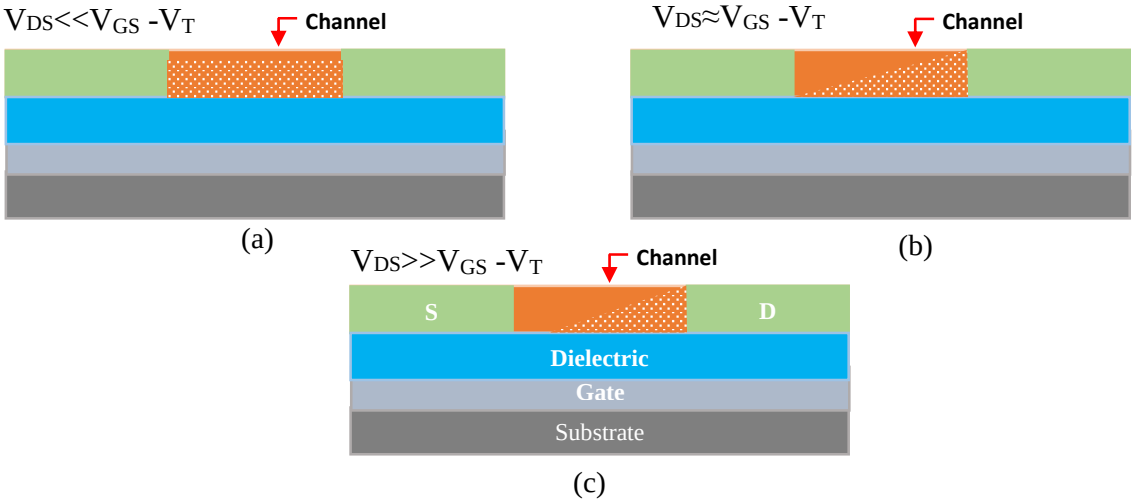

Figure 2.36. OTFT operation (a) linear region, (b) pinch-off point and (c) saturation region

Figure 2.37 shows the typical output and transfer characteristics of the p-type OTFT and its operating regions. The currents and voltage values shown in the Fig. 2.37 (a) are negative as the p-type OTFT works in negative voltages. For the

OTFT to operate in the liner region, the conditions show in equation (8) has to be satisfied [190].

$$V_{DS} \leq V_{GS} - V_T \tag{8}$$

In the linear region, the current varies linearly with the applied voltage and mathematically expressed as

$$I_D = C_{OX} \frac{w}{l} \mu_{lin} (V_{GS} - V_t - \frac{V_{DS}}{2}) V_{DS} \tag{9}$$

Where I_D is the drain current, C_{OX} is the gate oxide capacitance per unit overlap area, μ_{lin} is the mobility in the linear region and *w/l* is the ratio of the channel width and length. When the V_{DS} is greater than the gate bias, the OTFT operates in saturation region (equation (10))

$$V_{DS} > V_{GS} - V_T \tag{10}$$

The drain current in the saturation region is given by equation (11)

$$I_D = C_{OX} \frac{w}{l} \mu_{sat} (V_{GS} - V_t)^2 \tag{11}$$

where μ_{sat} is the mobility in the saturation region. C_{ox} for both the regions is given by

$$C_{ox} = \frac{k\varepsilon_0}{t_{ox}} \tag{12}$$

In equation (12), *k* is the dielectric contact of the insulator, ε_0 is the permittivity constant and t_{ox} is the thickness of the dielectric layer. From eq. 11, V_t can be given as

$$V_t = V_{GS} - \sqrt{\frac{I_D}{C_{ox}\mu_{sat}\left(\frac{w}{l}\right)}} \tag{13}$$

From eq. 13, V_t is same as V_{GS} when I_D is equal to zero. The threshold voltage can also be extracted from the transfer characteristics which are plotted with square root of the drain current to the gate to source voltage as shown in Fig. 2.37 (b).

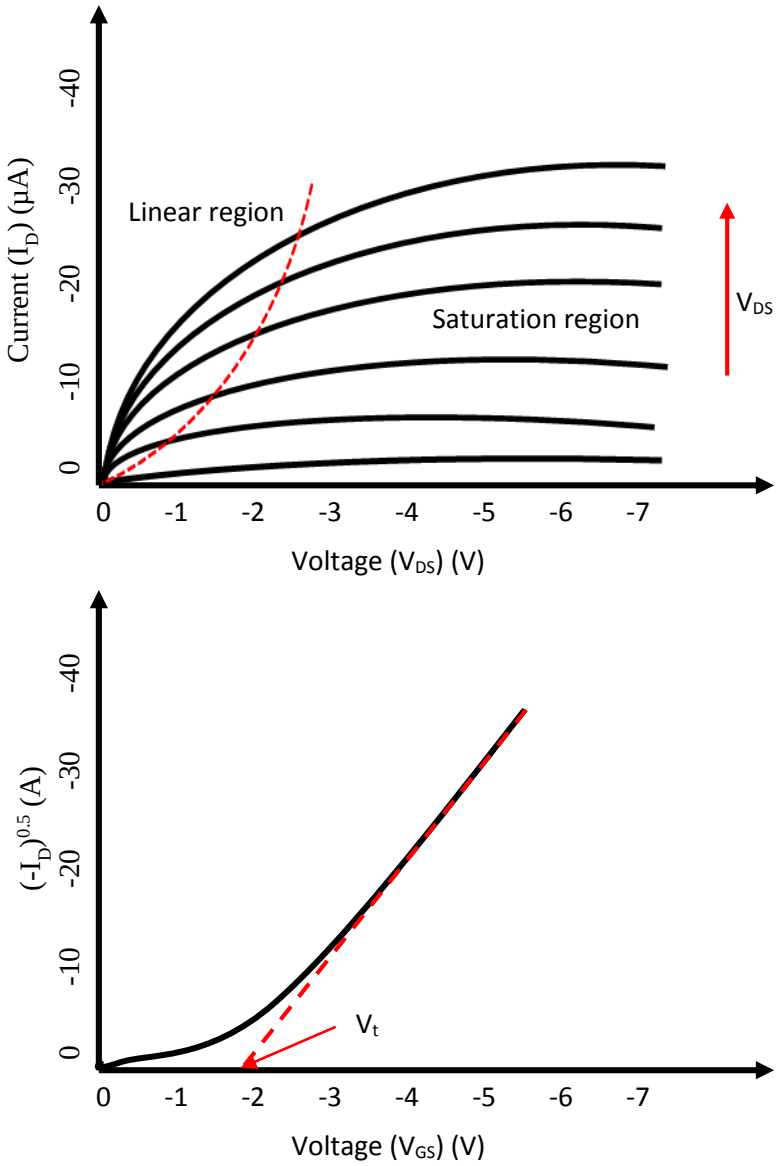

Figure 2.37. Typical (a) output and (b) transfer characteristics of the OTFT.

Threshold voltage and mobility are the two major parameters that are usually reported in TFT characterization. In addition, on/off current ratio is also reported to determine the performance of the OTFT.

2.9.3 OTFT Based Sensors

OTFT based sensors have been gaining a lot of interest for various application such as artificial skin, drug delivery, food safety, environmental monitoring, medical diagnostics and light sensing applications [191-196]. The use of printing techniques

such as inkjet printing, screening printing and gravure printing in the fabrication of OTFT on low cost plastics has an added advantage of cost effectiveness compared to the traditional Si based fabricated OTFTs. Usually, the semiconductor is the sensitive material that changes its characteristics with the input measurand. OTFT sensors exhibit higher sensitivity compared to the two terminal sensors such as impedance and capacitive based sensors as it is a combination of a sensor and an amplifier. The small change in the sensor is amplified by the effective gate voltage resulting in a higher sensitivity [197].

2.10 Summary

In this chapter, a brief history of sensors has been given followed by various types of sensors and sensor characteristics having been discussed. An introduction to PE including the advantages of PE over conventional Si based fabrication is included. The chapter also discussed the various printing techniques used for fabrication of electronic devices and a few challenges for printed electronics were also presented. A brief introduction to organic semiconductors and TFT's was also included. The following chapter will discuss the development of printed OTFT sensors for detection of relative humidity. The author presents the design, fabrication and characterization of an OTFT sensor, as well as the measurement set-up, testing, results, discussion and conclusion.

References

[1] M. Schulz, “The end of the road for silicon?” Nature, vol. 399, pp. 729-730, 1999.

[2] L.B. Wilner, “Variable capacitance liquid level sensors”, Review of Scientific Instruments, vol. 31(5), pp. 501-507, 1960.

[3] A.M. Mayo, C.L. Buddecke and G.R. Tenery, “Data Sensors and Information Acquisition”, Proc. First International Symposium on Basic Environmental Problems of Man in Space, pp. 493-506, 1965.

[4] E.G. Moore, “Application of remote sensors to the classification of areal data at different scales: a case study in housing quality”, Remote Sensing of Environment, vol. 1(2), pp. 109-121, 1970.

[5] I.A. Troyan, A.D. Shevchuk and Y.M. Golovanev, “A sensor for measuring the amplitude of high frequency mechanical oscillations”, Strength of Materials, vol. 7(2), pp. 255-256, 1975.

[6] J.D. Meindl, “Biomedical implantable microelectronics”, Sci., vol. 210(4467), pp. 263-267, 1980.

[7] J.F. McAleer, P.T. Moseley, P. Bourke, J.O.W. Norris and R. Stephan, “Tin dioxide gas sensors: use of the Seebeck effect”, Sensors and Actuators, vol. 8(3), pp. 251-257, 1985.

[8] K. Kalcher, J.M. Kauffmann, J. Wang, I. Svancara, K. Vytras, C. Neuhold and Z. Yang, “Sensors based on carbon paste in electrochemical analysis: a review with particular emphasis on the period 1990–1993”, Electroanalysis, vol. 7(1), pp. 5-22, 1995.

[9] H. Suzuki, “Advances in the microfabrication of electrochemical sensors and systems”, Electroanalysis, vol. 12(9), pp. 703-715, 2000.

[10] A. Caballero, R. Martínez, V. Lloveras, I. Ratera, J.V. Gancedo, K. Wurst, A. Tarraga, P. Molina and J. Veciana, "Highly selective chromogenic and redox or fluorescent sensors of Hg^{2+} in aqueous environment based on 1, 4-disubstituted azines", Journal of the American Chemical Society, vol. 127, pp. 15666-15667, 2005.

[11] H. Greve, E. Woltermann, R. Jahns, S. Marauska, B. Wagner, R. Knochel, M. Wuttig and E. Quandt, "Low damping resonant magnetoelectric sensors", Applied Physics Letters, vol. 97, pp. 152503, 2010.

[12] G. Ross, "MEMS Semiconductor Sales to reach $8B in 2014", Electronics Purchasing Strategies, July 14, 2014, Available: http://electronicspurchasingstrategies.com/2014/07/14/mems-semiconductor-sales-reach-8b-2014/ [Accessed: May 10, 2015].

[13] F. Jacob, "Hand Book of Modern Sensors", Springer New York, 2003.

[14] F.C. Lane, "The Economic Meaning of the Invention of the Compass," The American Historical Review, vol. 68 (3), pp.616, 1963.

[15] H.J. Debra, "Weather Scientists", Capstone, 2009.

[16] J. G. Webster, "Measurement, Instrumentation and Sensors Handbook", CRC press, 1999.

[17] G. Gustav, "Piezoelectric Sensorics: Force, Strain, Pressure, Acceleration and Acoustic Emission Sensors", Materials and Amplifiers. 2002.

[18] Sarah Jensen, Ask and Engineer, "How do Glucometers work?", Oct. 16, 2011 Available : http://engineering.mit.edu/ask/how-do-glucometers-work [Accessed: May 10, 2015]

[19] H. N. Norton, "Sensor and Analyzer Handbook", Prentice-Hall, pp. 562, 1982.

[20] M. L. Garcia, “Interior intrusion sensors”, in Design and Evaluation of Physical Protection Systems Anonymous, pp. 351, 2007.

[21] Body, Soul, and Spirit. Available: https://shareaverse.wordpress.com/2012/06/10/body-soul-and-spirit/ [Accessed: May. 10, 2014].

[22] J. Vetelino, A. Reghu, “Introduction to Sensors”, CRC Press, 2010.

[23] T. Tatsuo, T. Tamura, P.A. Oberg, “Biomedical sensors and instruments”, CRC Press, 2011.

[24] C.N. Fu, T.Y. Huang. “Sensitivity and kinetic analysis of graphene oxide-based surface plasmon resonance biosensors”, Sensors and Actuators B Chemical vol. 197, pp. 35-42, 2014.

[25] S.A. Dyer, “Wiley survey of instrumentation and measurement”, John Wiley & Sons, 2004.

[26] P.G. Ruiz, K. De Meyer, A. Witvrouw, “Poly-SiGe for MEMS-above-CMOS Sensors”, Springer, 2014.

[27] I.R. Sinclair, “Sensors and Transducers”, Butterworth-Heinemann, 2001.

[28] A. Docherty, L. Poladian, A. Argyros, M. C. J. Large, J. Poulin and R. Kashyap, “Increasing the Numerical Aperture of Large-Core Microstructured Polymer Optical Fibers Using a ‘Y’-Bridge Cladding”, Journal of Lightwave Technology, vol. 27, pp. 1610-1616, 2009.

[29] D. Stanislav and F. Jan, “Optical sensors”, in Modern Sensors Handbook ISTE, pp. 49, 2007/

[30] L.G. Béla, “Instrument Engineers Handbook”, Volume Two: Process Control and Optimization. vol. 2. CRC press, 2005.

[31] Z.S. Kim, S.C. Lim, S.H. Kim, Y.S. Yang, D.H. Hwang, “Biotin-Functionalized Semiconducting Polymer in an Organic Field Effect Transistor and Application as a Biosensor”, Sensors, vol. 12, pp. 11238-11248, 2012.

[32] L. Moretto, K. Kalcher, “Environmental Analysis by Electrochemical Sensors and Biosensors”, Nanostructure Science and Technology, Springer, 2015.

[33] L. Clark and C. Lyons, “Electrode systems for continuous monitoring in cardiovascular surgery”, Ann. N. Y. Acad. Sci., vol. 102, pp. 29-45, 1962.

[34] R. Tor, “New enzyme membrane for enzyme electrodes”, Anal. Chem., vol. 58, pp. 1042-1046, 1986.

[35] L. Cui, J. Wu, H. Ju, “Electrochemical sensing of heavy metal ions with inorganic, organic and bio-materials”, Biosensors and Bioelectronics, vol. 63, pp. 276-286, 2015.

[36] H. Zhu, Y. Xu, A. Liu, N. Kong, F. Shan, W. Yang, C.J. Barrow, J. Liu, “Graphene nanodots-encaged porous gold electrode fabricated via ion beam sputtering deposition for electrochemical analysis of heavy metal ions”, Sensors and Actuators B: Chemical, vol.206, pp. 592-600, 2015.

[37] S. Zhou, T. Zheng, Y. Chen, J. Zhang, L. Li, F. Lu, J.J. Zhu, “Toward therapeutic effects evaluation of chronic myeloid leukemia drug: Electrochemical platform for caspase-3 activity sensing”, Biosensors and Bioelectronics, vol. 61, pp. 648-654, 2014.

[38] J. Narang, N. Malhotra, G. Singh, C.S. Pundir, “Electrochemical impediometric detection of anti-HIV drug taking gold nanorods as a sensing interface”, Biosensors and Bioelectronics, vol. 66, pp. 332-337, 2015.

[39] A.J. Bandodkar, J. Wang, “Non-invasive wearable electrochemical sensors: a review”, Trends in Biotechnology, vol. 32(7), pp.363-371, 2014.

[40] J. Wang, “Electrochemical Sensing of Explosives”, Electroanalysis, vol. 19(4), pp. 415–423, 2007.

[41] A. J. Bard and L. R. Faulkner, "Electrochemical methods," John Wiley & Sons, Inc., New York, NY, pp. 232-236, 1980.

[42] J.R. Macdonald, E. Barsoukov, “Impedance Spectroscopy Theory, Experiment, and Applications” Science, pp. 595, 2005.

[43] K.S. Cole, R.H. Cole, “Dispersion and Absorption in Dielectrics - I Alternating Current Characteristics”, Journal of Chemical Physics, vol. 9, pp. 341–352, 1941.

[44] K.S. Cole, R.H. Cole, “Dispersion and Absorption in Dielectrics - II Direct Current Characteristics”, Journal of Chemical Physics vol. 10, pp. 98–105, 1942.

[45] H. Nyquist, “Regeneration Theory”, Bell Labs Technical Journal, vol. 11 pp. 126–147, 1932.

[46] T.A.K. Gregory, “Chemical and biological transducers,” in Micromachined Transducers Sourcebook, The McGraw-Hill, pp. 715, 1998.

[47] A.C. Fisher, “Electrode Dynamics”, Oxford Chemistry Primers 1996.

[48] A.J. Bard, L.R. Faulkner, “Electrochemical Methods: Fundamentals and Applications”, Wiley New York, 2001.

[49] A.M. Bond, “Broadening Electrochemical Horizons: Principles and Illustrations of Voltammetric and Related Techniques”, Oxford, New York, 2002.

[50] J.F. Rusling, A.F. Nassar, “Electron transfer rates in electroactive films from normal pulse voltammetry. Myoglobin-surfactant films,” Langmuir, vol. 10, pp. 2800-2806, 1994.

[51] J.A. Ortuño, C. Serna, A. Molina, A. Gil, “Differential pulse voltammetry and additive differential pulse voltammetry with solvent polymeric membrane ion sensors,” Analytical Chemistry, vol. 78, pp. 8129-8133, 2006.

[52] N.G. Rajendra, B. Sunita, A. Bharati. “Single-walled-carbon-nanotube-modified pyrolytic graphite electrode used as a simple sensor for the determination of salbutamol in urine”, International Journal of Electrochemistry, pp. 1-8, 2011.

[53] M. Consales, A. Buosciolo, A. Cutolo, G. Breglio, A. Irace, S. Buontempo, P. Petagna, M. Giordano, A. Cusano, “Fiber optic humidity sensors for high-energy physics applications at CERN”, Sensors and Actuators, B: Chemical, vol. 159, pp. 66-74, 2011.

[54] K.M. Tan, S.C. Tjin, C.C. Chan, L. Mohanty, C.M. Tay, “High relative humidity sensing using gelatin-coated long period grating”, Proceedings of SPIE - the International Society for Optical Engineering, pp. 375-378,2005.

[55] Z. Zhu, J.T. Mason, R. Dieckmann, G.G. Malliaras, “Humidity sensors based on pentacene thin-film transistors”, Applied Physics Letters, vol. 81, pp. 4643-4645, 2002.

[56] N. Ichinose, “Ceramic Sensors in the Microprocessor Industry”, Ceramurgia, vol. 18, pp. 79-83, 1988.

[57] Z. Chen, C. Lu, “Humidity sensors: A review of materials and mechanisms”, Sensor Letters, vol. 3, pp. 274-295, 2005.

[58] A. Tételin, C. Pellet, C. Laville, G. N'Kaoua, “Fast response humidity sensors for a medical microsystem”, Sensors and Actuators, B: Chemical, vol. 91, pp. 211-218, 2003.

[59] J.C. Harding, “A chilled mirror dew point sensor/psychrometric transmitter for energy monitoring and control systems. In: Moisture and humidity”, Proceedings of the International Symposium on Moisture and Humidity, 1985.

[60] C. Porlier, “Chilled piezoelectric hygrometer: sensor interface design. In: Sensors Expo Proceedings”, Helmers Publishing, vol. 107B-7, 1991.

[61] T. Miura, “Thermistor humidity sensor for absolute humidity measurements and their applications”, Moisture and Humidity1985, pp. 855-873, 1985.

[62] P.M. Harrey, B.J. Ramsey, P.S.A. Evans, D.J. Harrison, “Capacitive-type humidity sensors fabricated using the offset lithographic printing process”, Sensors and Actuators, B: Chemical, vol. 87, pp. 226-232, 2002.

[63] B. Johann, Y. Koren, “Obstacle avoidance with ultrasonic sensors”, IEEE Journal of Robotics and Automation, vol. 4(2), pp. 213-218, 1988.

[64] T.P. Kai, “Design and characterization of the immersion-type capacitive ultrasonic sensors fabricated in a CMOS process”, Journal of Micromechanics and Microengineering, vol. 21(2) pp. 025013, 2011.

[65] G.N. Ivan, L. Spedicato, C.D. Castri, “A new strategy for spatial reconstruction of orthogonal planes using a rotating array of ultrasonic sensors”, IEEE Sensors Journal vol. 12(5), pp. 1307-1316, 2012.

[66] B.Y. Wen, L.S. Shen, L.H. Zong, “Design and implementation of an embedded home surveillance system by use of multiple ultrasonic sensors”, IEEE Transactions on Consumer Electronics, vol. 56(1), pp. 119-124, 2010.

[67] H. Lelu, “An ultrasonic level measuring technique based on radiation dissipation and its industrial application” Flow Measurement and Instrumentation, 2014.

[68] I. Gresham, A. Jenkins, R. Egri, C. Eswarappa, N. Kinayman, N. Jain, J.P. Lanteri, “Ultra-wideband radar sensors for short-range vehicular applications” IEEE Transactions on Microwave Theory and Techniques, vol. 52(9), pp. 2105-2122, 2004.

[69] J. Hasch, E. Topak, R. Schnabel, T. Zwick, R. Weigel, C. Waldschmidt, “Millimeter-wave technology for automotive radar sensors in the 77 GHz

frequency band", IEEE Transactions on Microwave Theory and Techniques, vol. 60(3), pp. 845-860, 2012.

[70] F. Florian, H. Rohling, U. Lubbert, "An automotive radar network based on 77 GHz FMCW sensors" IEEE International Radar Conference, 2005.

[71] M. Tons, R. Doerfler, M.M. Meinecke, M.A. Obojski, "Radar sensors and sensor platform used for pedestrian protection in the EC-funded project SAVE-U" IEEE Intelligent Vehicles Symposium, pp. 813-818, 2004.

[72] B. Li, Z. Zhou, W. Zou, G. Du, "An intelligence inspired blind data detection for ultra-wideband radar sensors" Information Sciences, vol. 255, pp. 204-220, 2014.

[73] A. Kumar, L. Zhuo, L. Qilian, Z. Baoju, X. Wu, "Experimental study of through-wall human detection using ultra wideband radar sensors" Measurement, vol. 47 pp. 869-879, 2014.

[74] G.M. Tina, F. Arcidiacono, A. Gagliano, "Intelligent sun-tracking system based on multiple photodiode sensors for maximisation of photovoltaic energy production", Mathematics and Computers in Simulation, vol. 91, pp. 16-28, 2013.

[75] E.J. Klem, J. Lewis, C. Gregory, D. Temple, P.S. Wijewarnasuriya, N. Dhar, "Low-cost SWIR sensors: advancing the performance of ROIC-integrated colloidal quantum dot photodiode arrays" International Society for Optics and Photonics SPIE Defense Security, pp. 907039-907039, 2014.

[76] T. Aoyama, S. Koyama, C. Kawaura, "An in-phantom dosimetry system using pin silicon photodiode radiation sensors for measuring organ doses in x-ray CT and other diagnostic radiology" Medical physics, vol. 29(7), pp. 1504-1510, 2002.

[77] J.M. Boudry, L.E. Antonuk, “Radiation damage of amorphous silicon photodiode sensors”, IEEE Transactions on Nuclear Science, vol. 41(4), pp. 703-707, 1994.

[78] J.M. Boudry, L.E. Antonuk, “Current-noise-power-spectra for amorphous silicon photodiode sensors”, In MRS Proceedings Cambridge University Press, vol. 297, pp. 975, 1993.

[79] Y. Wang, Y. Jia, Q. Chen, Y. Wang, “A passive wireless temperature sensor for harsh environment applications” Sensors, vol. 8(12), pp. 7982-7995, 2008.

[80] J.Y. Yang, D.W. Clarke, “A self-validating thermocouple” IEEE Transactions on Control Systems Technology, vol. 5(2), pp. 239-253, 1997.

[81] A.E. Vidrio, D. Mateo, J. Altet, “Differential temperature sensors fully compatible with a 0.35μm CMOS process”, IEEE Transactions on Components and Packaging Technologies, vol. 30(4), pp. 618-626, 2007.

[82] M.J. Mattu, G.W. Small, R.J. Combs, R.B. Knapp, R.T. Kroutil, “Quantitative analysis of sulfur dioxide with passive Fourier transform infrared remote sensing interferogram data”, Applied Spectroscopy, vol. 54(3), pp. 341-348, 2000.

[83] H. Cheng, S. Ebadi, X. Gong, “A low-profile wireless passive temperature sensor using resonator/antenna integration up to 1000 C”, Antennas and Wireless Propagation Letters, IEEE, vol. 11, pp. 369-372, 2012.

[84] B.F. Spencer, M.E. Ruiz-Sandoval, N. Kurata, “Smart sensing technology: opportunities and challenges”, Structural Control and Health Monitoring, vol. 11(4), pp. 349-368, 2004.

[85] M. Ribeiro, O. Postolache, P. Girão, “A Novel Smart Sensing Platform for Vital Signs and Motor Activity Monitoring”, Springer International Publishing In Sensing Technology: Current Status and Future Trends I pp. 1-24, 2014

[86] J.A. Pickett, G.I. Aradottír, M.A. Birkett, T.J. Bruce, A.M. Hooper, C.A. Midega, Z.R. Khan, “Delivering sustainable crop protection systems via the seed: exploiting natural constitutive and inducible defence pathways” Philosophical Transactions of the Royal Society B: Biological Sciences, vol. 369(1639), pp. 20120281, 2014.

[87] D.M. Han, J.H. Lim, “Design and implementation of smart home energy management systems based on ZigBee” IEEE Transactions on Consumer Electronics, vol. 56(3), pp. 1417-1425, 2010.

[88] C.B. Yun, J. Min, “Smart sensing, monitoring, and damage detection for civil infrastructures” KSCE Journal of Civil Engineering, vol. 15(1), pp. 1-14, 2011.

[89] N. Lajnef, M. Rhimi, K. Chatti, L. Mhamdi, F. Faridazar, “Toward an integrated smart sensing system and data interpretation techniques for pavement fatigue monitoring” Computer-Aided Civil and Infrastructure Engineering, vol. 26(7), pp. 513-523, 2011.

[90] C. Perera, A. Zaslavsky, P. Christen, D. Georgakopoulos, “Sensing as a service model for smart cities supported by internet of things”, Transactions on Emerging Telecommunications Technologies, vol. 25(1), pp. 81-93, 2014.

[91] M.A. Nasir, H. Akram, Z.M. Khan, M. Shah, S. Anas, Z. Asfar, S. Nauman,” Smart sensing layer for the detection of damage due to defects in a laminated composite structure”, Journal of Intelligent Material Systems and Structures, 1045389X14554138, 2014.

[92] A. Kumar, G.P. Hancke, “An Energy-Efficient Smart Comfort Sensing System Based on the IEEE 1451 Standard for Green Buildings”, IEEE Sensors Journal, vol.14(12), pp. 4245-4252, 2014

[93] T. Denison, P. Cong, P. Afshar, “Exploring Smart Sensors for Neural Interfacing”, Smart Sensor Systems: Emerging Technologies and Applications, pp. 190-236, 2014.

[94] N. Li, B.B. Gerber, “Assessment of a Smart Phone-Based Indoor Localization Solution for Improving Context Awareness in the Construction Industry”, Bridges, vol. 10, pp. 9780784412343-0071, 2014.

[95] M.M. Baig, H. Gholamhosseini, “Smart health monitoring systems: an overview of design and modeling”, Journal of medical systems, vol. 37(2), pp. 1-14, 2013.

[96] D.G. O'Keeffe, “Development of fibre optic evanescent-wave fluorescent-based sensors”, PhD diss., Dublin City University, 1995.

[97] A.G. McNamara, “Semiconductor diodes and transistors as electrical thermometers”, Review of Scientific Instruments, vol. 33(3), pp. 330-333, 1962.

[98] D.H. Sargeant, “Note on the use of junction diodes as temperature sensors”, Journal of Applied Meteorology, vol. 4(5), pp. 644-646, 1965.

[99] S.C. Chang, “Thin-film semiconductor NOx sensor”, IEEE Transactions on Electron Devices, vol. 26(12), pp. 1875-1880, 1979.

[100] K.N. Sundaram, “Semiconductor Sensors for Automotive Instrumentation” SAE Technical Paper, 730572, 1973.

[101] H. Wohltjen, W.R. Barger, A.W. Snow, N.L. Jarvis, “A vapor-sensitive chemiresistor fabricated with planar microelectrodes and a Langmuir-Blodgett organic semiconductor film”, IEEE Transactions on Electron Devices, vol. 32, pp. 1170-1174, 1985.

[102] P.K. Clifford, D.T. Tuma, “Characteristics of semiconductor gas sensors II. Transient response to temperature change”, Sensors and Actuators, vol. 3, pp. 255-281, 1983.

[103] M. Akiyama, J. Tamaki, N. Miura, N. Yamazoe, “Tungsten Oxide-Based Semiconductor Sensor Highly Sensitive to NO and NO_2”, Chemistry Letters, vol. 9, pp. 1611-1614, 1991.

[104] N. Yamazoe, N. Miura, “Some basic aspects of semiconductor gas sensors”, Chemical Sensor Technology, vol. 4, pp. 19-42, 1992.

[105] L. Li, P. Gao, M. Baumgarten, K. Müllen, N. Lu, H. Fuchs, L. Chi, “ High performance field-effect ammonia sensors based on a structured ultrathin organic semiconductor film”, Advanced Materials, vol. 25(25), pp. 3419-3425, 2013.

[106] H. Yabuta, N. Kaji, M. Shimada, T. Aiba, K. Takada, H. Omura, H. Kumomi, “Microscopic structure and electrical transport property of sputter-deposited amorphous indium-gallium-zinc oxide semiconductor films”, Journal of Physics: Conference Series, vol. 518(1), pp. 012001, 2014.

[107] M. Acuautla, S. Bernardini, L. Gallais, T. Fiorido, L. Patout, M. Bendahan, “Ozone flexible sensors fabricated by photolithography and laser ablation processes based on ZnO nanoparticles”, Sensors and Actuators B: Chemical, vol. 203, pp. 602-611, 2014.

[108] Y. Hanazato, M. Nakako, M. Maeda, S. Shiono, “Glucose sensor based on a field-effect transistor with a photolithographically patterned glucose oxidase membrane”, Analytical chimical acta, vol. 193, pp. 87-96, 1987.

[109] D.C. Abeysinghe, S. Dasgupta, J.T. Boyd, H.E. Jackson, “A novel MEMS pressure sensor fabricated on an optical fiber”, IEEE Photonics Technology Letters, vol. 13(9), pp. 993-995, 2001.

[110] P. Nussbaum, R. Voelkel, H.P. Herzig, M. Eisner, M., S. Haselbeck, “Design, fabrication and testing of microlens arrays for sensors and microsystems” Pure

and Applied Optics: Journal of the European Optical Society Part A, vol. 6(6), pp. 617, 1997.

[111] M.W. Ahn, K.S. Park, J.H. Heo, D.W. Kim, K.J. Choi, J.G. Park, "On-chip fabrication of ZnO-nanowire gas sensor with high gas sensitivity" Sensors and Actuators B: Chemical, vol. 138(1), pp. 168-173, 2009.

[112] W. Ehrfeld, F. Gotz, D. Munchmeyer, W. Schelb, D. Schmidt, "LIGA process: sensor construction techniques via X-ray lithography", IEEE Solid-State Sensor and Actuator Workshop, pp. 1-4, 1988.

[113] H. Guckel, K.J. Skrobis, T.R. Christenson, J. Klein, S. Han, B. Choi, E.G. Lovell, "Fabrication of assembled micromechanical components via deep X-ray lithography", Micro Electro Mechanical Systems, (IEEE MEMS'91), pp. 74-79,1991.

[114] S.M. Ford, B. Kar, S. Mcwhorter, J. Davies, S.A. Soper, M. Klopf, V. Saile, "Microcapillary electrophoresis devices fabricated using polymeric substrates and X-ray lithography" Journal of Microcolumn Separations, vol. 10(5), pp. 413-422, 1998.

[115] L. Brigo, G. Grenci, A. Carpentiero, A. Pistore, M. Tormen, M. Guglielmi, G. Brusatin, "Positive resist for UV and X-ray lithography synthesized through sol–gel chemistry" Journal of sol-gel science and technology, vol. 60(3), pp. 400-407.

[116] V. Giorgis, P. Zilio, M Massari, G. Ruffato, G. Zacco, F. Romanato, "Fabrication of multiple large arrays of split ring resonators by X-ray lithographic process for sensing purposes" Microelectronic Engineering, vol. 127, pp. 68–71, 2014.

[117] G. Grenci, E. Sovernigo, A.Z. Khokhar, N. Gadegaard, M. Prasciolu, M. Tormen, “Microfabrication of sharp blazed gratings by a two-step height amplification process based on soft and deep X-ray lithography”, Sensors and Actuators A: Physical, vol. 205, pp. 111-118, 2014.

[118] K.J. Jeon, J.M. Lee, E. Lee, W. Lee, W “Individual Pd nanowire hydrogen sensors fabricated by electron-beam lithography”, Nanotechnology, vol. 20(13), pp. 135502, 2009.

[119] H. Zhou, A. Midha, G. Mills, S. Thoms, S.K. Murad, J.M.R. Weaver, “Generic scanned-probe microscope sensors by combined micromachining and electron-beam lithography” Journal of Vacuum Science & Technology B, vol. 16(1), pp. 54-58, 1998.

[120] R. Palankar, N. Medvedev, A. Rong, M. Delcea, “Fabrication of quantum dot microarrays using electron beam lithography for applications in analyte sensing and cellular dynamics”, ACS nano, vol. 7(5), pp. 4617-4628, 2013.

[121] S. Chen, M. Svedendahl, T.J. Antosiewicz, M. Käll, “Plasmon-Enhanced Enzyme-Linked Immunosorbent Assay on Large Arrays of Individual Particles Made by Electron Beam Lithography” ACS nano, vol. 7(10), pp.8824-8832, 2013.

[122] V. Tsukala, D. Kouzoudis, “Zeolite micromembrane fabrication on magnetoelastic material using electron beam lithography” Microporous and Mesoporous Materials, vol. 197, pp. 213-220, 2014.

[123] T.C. Garza, J.I. Scholtz, M.J. Gazes, I. Kymissis, N.K. Pervez, “Low-cost photonic crystals for spectral sensors fabricated using projection lithography” SPIE Sensing Technology Applications, pp. 91010F-91010F, 2014.

[124] A.N. Abbas, G. Liu, B. Liu, L. Zhang, H. Liu, D. Ohlberg, C. Zhou, “Patterning, Characterization, and Chemical Sensing Applications of Graphene Nanoribbon Arrays Down to 5 nm Using Helium Ion Beam Lithography” ACS nano, vol. 8(2), pp. 1538-1546, 2014.

[125] F.H. Ramirez, J. Rodriguez, O. Casals, E. Russinyol, A. Vila, A.R. Rodriguez, M. Abid, “Characterization of metal-oxide nanosensors fabricated with focused ion beam (FIB)”, Sensors and Actuators B: Chemical, vol. 118(1), pp. 198-203, 2006.

[126] B.N. Miles, A.P. Ivanov, K.A. Wilson, F. Doğan, D. Japrung, J.B. Edel, “Single molecule sensing with solid-state nanopores: novel materials, methods, and applications” Chemical Society reviews, vol. 42(1), pp. 15-28, 2013.

[127] C. Granata, E. Esposito, A. Vettoliere, L. Petti, M. Russo, “An integrated superconductive magnetic nanosensor for high-sensitivity nanoscale applications” Nanotechnology, vol. 19(27), pp. 275501, 2008.

[128] C.B. Freidhoff, R.M. Young, S. Sriram, T.T. Braggins, T.W. O'Keefe, J.D. Adam, J. Tunstall, “Chemical sensing using nonoptical microelectromechanical systems” Journal of Vacuum Science & Technology A, vol. 17(4), pp. 2300-2307, 1999.

[129] A.L. Trimmer, J.L. Hudson, M. Kock, R. Schuster, “Single-step electrochemical machining of complex nanostructures with ultrashort voltage pulses” Applied Physics Letters, vol. 82(19), pp. 3327-3329, 2003.

[130] X. Li, J. Tian, G. Garnier, W. Shen, “Fabrication of paper-based microfluidic sensors by printing” Colloids and Surfaces B: Biointerfaces, vol. 76(2), pp. 564-570, 2010.

[131] B. Ando, S. Baglio, “Inkjet-printed sensors: a useful approach for low cost, rapid prototyping” IEEE Instrumentation & Measurement Magazine, vol. 14(5), pp. 36-40, 2011.

[132] R.B. Tait, R. Humphries, J. Lorenz, “Thick film heater elements and temperature sensors in modern domestic appliances” IEEE Transactions on Industry Applications, vol. 30(3), pp. 573-577, 1994.

[133] M. Berggren, R. Forchheimer, J. Bobacka, P.O. Svensson, D. Nilsson, O. Larsson, A. Ivaska, “PEDOT: PSS-based electrochemical transistors for ion-to-electron transduction and sensor signal amplification” Inorganic Semiconductors in Sensor Applications pp. 263-280, 2008.

[134] M. Borghetti, E. Sardini, M. Serpelloni, “Preliminary study of resistive sensors in inkjet technology for force measurements in biomedical applications”, IEEE 11th International Multi-Conference on Systems, Signals & Devices (SSD), pp. 1-4 2014.

[135] “Printed electronics sector takes a hard look at the flexible future”, Plastemart, April 15, 2015, Available: http://www.plastemart.com/Plastic-Technical-Article.asp?LiteratureID=1944&Paper=printed-electronics-sector-flexible-future [Accessed: May 11, 2015]

[136] R. Gupta, S. Walia, M. Hösel, J. Jensen, D. Angmo, F.C. Krebs, G.U. Kulkarni, “Solution processed large area fabrication of Ag patterns as electrodes for flexible heaters, electrochromics and organic solar cells” Journal of Materials Chemistry A, vol. 2, pp. 10930-10937, 2014.

[137] M. Layani, P. Darmawan, W.L. Foo, L. Liu, A. Kamyshny, D. Mandler, P.S. Lee, “Nanostructured electrochromic films by inkjet printing on large area

and flexible transparent silver electrodes" Nanoscale, vol. 6(9), pp. 4572-4576, 2014.

[138] U. Männl, C. Van den Berg, B. Magunje, M. Härting, D.T. Britton, S. Jones, M.R. Scriba, "Nanoparticle composites for printed electronics" Nanotechnology, vol. 25(9), pp. 094004. 2014.

[139] K.J. Lee, B.H. Jun, T.H. Kim, and J. Joung, "Direct synthesis and inkjetting of silver nanocrystals toward printed electronics," Nanotechnology, vol. 17(9), pp. 2424, 2006.

[140] V. Subramanian, J.M. Fréchet, P.C. Chang, D C. Huang, J.B. Lee, S.E. Molesa, S.K. Volkman, "Progress toward development of all-printed RFID tags: materials", Proceedings of the IEEE processes, and devices, vol. 93(7), pp. 1330-1338, 2005.

[141] J. Virkki, T. Björninen, S. Merilampi, L. Sydänheimo, L. Ukkonen, "Manufacturing and Applications of Screen-printed RFID Tags on Paper Substrate" Progress in Electromagnetics Research Symposium (PIERS), 2013.

[142] J. Virtanen, J. Virkki, L. Sydanheimo, M. Tentzeris, L. Ukkonen, "Automated Identification of Plywood Using Embedded Inkjet-Printed Passive UHF RFID Tags" IEEE Transactions on Automation Science and Engineering, vol. 10(3), pp. 796-806, 2013.

[143] G. Orecchini, L. Yang, M.M. Tentzeris, L. Roselli, "Wearable battery-free active paper-printed RFID tag with human-energy scavenger", IEEE MTT-S International Microwave Symposium Digest (MTT), pp. 1-1, 2011.

[144] S. Molesa, D.R. Redinger, D.C. Huang, V. Subramanian, "High-quality inkjet-printed multilevel interconnects and inductive components on plastic for ultra-low-cost RFID applications" MRS Proceedings vol. 769, pp. H8-3, 2003.

[145] T.R. Hebner, C.C. Wu, D. Marcy, M.H. Lu, J.C. Sturm, “Ink-jet printing of doped polymers for organic light emitting devices” Applied Physics Letters, vol. 72(5), pp. 519-521, 1998.

[146] S.C Chang, J. Liu, J. Bharathan, Y. Yang, J. Onohara, J. Kido, “Multicolor organic light-emitting diodes processed by hybrid inkjet printing”, Advanced Materials, vol. 11(9), pp. 734-737, 1999.

[147] F. Villani, P. Vacca, G. Nenna, O. Valentino, G. Burrasca, T. Fasolino, D. della Sala, “Inkjet printed polymer layer on flexible substrate for OLED applications”, The Journal of Physical Chemistry C, vol. 113(30), pp. 13398-13402, 2009.

[148] G.E. Jabbour, R. Radspinner, N. Peyghambarian, “Screen printing for the fabrication of organic light-emitting devices”, IEEE Journal of Selected Topics in Quantum Electronics, vol. 7(5), pp. 769-773, 2001.

[149] R. Tajima, T. Miwa, T. Oguni, A. Hitotsuyanagi, H, Miyake, H. Katagiri, M. Takahashi, “28.2: Genuinely Wearable Display with a Flexible Battery, a Flexible Display Panel, and a Flexible Printed Circuit”, SID Symposium Digest of Technical Papers, vol. 45(1), pp. 367-370, 2014.

[150] B. Yoon, D.Y. Ham, O. Yarimaga, H. An, C.W. Lee, J.M. & Kim, “Inkjet printing of conjugated polymer precursors on paper substrates for colorimetric sensing and flexible electrothermochromic display” Advanced Materials, vol. 23(46), pp. 5492-5497, 2011.

[151] D.E. Anagnostou, A.A. Gheethan, A.K. Amert, W.K. Whites, “A direct-write printed antenna on paper-based organic substrate for flexible displays and WLAN applications” Journal of Display Technology, vol. 6(11), pp. 558-564, 2010.

[152] A.P. Tarun, B. Lahey, A. Girouard, W. Burleson, R. Vertegaal, “Snaplet: using body shape to inform function in mobile flexible display devices” ACM CHI'11 Extended Abstracts on Human Factors in Computing Systems pp. 329-334, 2011.

[153] R. Dijkstra, C. Perez, R. Vertegaal, “Evaluating effects of structural holds on pointing and dragging performance with flexible displays” Proceedings of the ACM SIGCHI Conference on Human Factors in Computing Systems pp. 1293-1302 2011.

[154] M.M. Tentzeris, S. Kim, R. Vyas, A. Traille, P. Pons, H. Aubert, A. Collado, “Inkjet-printed “Zero-Power” wireless sensor and power management nodes for IoT and “Smart Skin” applications” 20th IEEE International Conference on Microwaves, Radar, and Wireless Communication (MIKON), pp. 1-7, 2014.

[155] M.T. Carter, J.R. Stetter, M.W. Findlay, V. Patel, “Printed Amperometric Gas Sensors. ECS Transactions”, vol. 50(12), pp. 211-220, 2013.

[156] B. Andò, S. Baglio, G. L’Episcopo, “Low cost inkjet printed sensors” Sensors, pp. 31-36, 2014.

[157] B. Ando, S. Baglio, C.O. Lombardo, V. Marletta, “An inkjet printed sensor for load measurement” IEEE Sensors Applications Symposium (SAS), pp. 185-188, 2014.

[158] E. Hrehorova, “Materials and processes for printed electronics: evaluation of gravure printing in electronics manufacture”, PhD Dissertation, Western Michigan University, Ann Arbor: ProQuest, 2007.

[159] S. Khan, L. Lorenzelli, R.S. Dahiya, “Technologies for Printing Sensors and Electronics Over Large Flexible Substrates: A Review”, IEEE Sensors Journal, vol. 15(6), pp. 3164-3185,2015.

[160] H. Kipphan, Handbook of Print Media: Technologies and Production Methods. New York: Springer, 2001.

[161] J. Daniel, "Printed Electronics: Technologies, Challenges and Applications", International Workshop on Flexible and Printed Electronics (IWFPE 10), 2010.

[162] R.D. Deegan, O. Bakajin, T.F. Dupont, G. Huber, S.R. Nagel, T.A. Witten, "Capillary flow as the cause of ring stains from dried liquid drops", Nature, vol. 389(6653), pp. 827-829, 1997.

[163] Printed and Flexible Sensors Market - Global Industry Size, Share, Trends, Analysis, and Forecasts 2012 – 2018. Available: http://www.transparencymarketresearch.com/printed-and-flexible-sensors-market.html [Accessed: Nov. 10, 2014].

[164] Printed and Flexible Sensors 2014-2024: Technologies, Players, Forecasts. Available: http://www.idtechex.com/research/reports/printed-and-flexible-sensors-2014-2024-technologies-players-forecasts-000367.asp [Accessed: May. 10, 2014].

[165] Printed and Flexible Sensors 2015-2025: Technologies, Players, Forecasts. Available: http://www.idtechex.com/research/reports/printed-and-flexible-sensors-2015-2025-technologies-players-forecasts-000428.asp [Accessed: Apr. 11, 2015].

[166] P.D. Beer, "Anion selective recognition and optical/electrochemical sensing by novel transition-metal receptor systems" Chemical Communication vol.6, pp.689-696, 1996.

[167] D.B. Keith, T.B. Scheffler, M.A. Brown. "Electrochemical sensors including electrodes with diffusion barriers" U.S. Patent No. 8,702,935, 2014.

[168] S. Partel, S. Kasemann, P. Choleva, C. Dincer, J. Kieninger, G.A. Urban, "Novel fabrication process for sub-micron interdigitated electrode arrays for highly sensitive electrochemical detection" Sensors and Actuators B: Chemical, vol.205, pp. 193-198, 2014.

[169] M. Carminati, C. Caviglia, A. Heiskanen, M. Vergani, G. Ferrari, M. Sampietro, T.A.J. Emnéus, "Theoretical and experimental comparison of microelectrode sensing configurations for impedimetric cell monitoring", Lecture Notes on Impedance Spectroscopy, vol. 4, pp. 75, 2013.

[170] M. Kimura, T. Mukuda, T. Matsuda, Y. Hiroshima, "P-3: Hybrid-Type Temperature Sensor using Thin-Film Transistors" SID Symposium Digest of Technical Papers, vol. 45(1), pp. 952-955, 2014.

[171] J. Taya, A. Nakashima, M. Kimura, "Thermal sensor employing ring oscillator composed of poly-Si thin-film transistors" Solid-State Electronics, vol. 79, pp. 14-17, 2013.

[172] S.H. Ha, D.H. Kang, I. Kang, J.U. Han, M. Mativenga, J. Jang, "Channel length dependent bias-stability of self-aligned coplanar a-IGZO TFTs", Journal of Display Technology, vol. 9(12), pp. 985-988, 2013.

[173] J. Lee, J.S. Park, B.L. Lee, J.I. Park, J.W. Chung, S. Lee, "Ionic self-assembled monolayer for low contact resistance in inkjet-printed coplanar structure organic thin-film transistors" Organic Electronics, vol. 15(9), pp. 2021-2026, 2014.

[174] Nobel Media AB 2014, "The Nobel Prize in Chemistry 2000", Available: http://www.nobelprize.org/nobel_prizes/chemistry/laureates/2000/ [Accessed: Apr. 24, 2015].

[175] C.D. Dimitrakopoulos, A.R. Brown, A. Pomp, “Molecular Beam Deposited Thin Films of Pentacene for Organic Field Effect Transistor Applications”, Journal of Applied Physics, vol. 80(4), pp. 2501-2508, 1996.

[176] M. Berggren, D. Nilsson, N.D. Robinson, “Organic materials for printed electronics”, Nature Materials, vol. 6, pp. 3-5, 2007.

[177] M.A. Ali, S.S.Y. Chen, Ha. Cavaye, A.R.G. Smith, P.L. Burn, I.R. Gentle, P. Meredith, P.E. Shaw, “Diffusion of nitroaromatic vapours into fluorescent dendrimer films for explosives detection”, Sensors and Actuators B: Chemical, vol. 210, pp. 550-557, 2015.

[178] J.D. Mello1, J. Anthony, S. Lee, “Organic Electronics: Recent Developments”, ChemPhysChem Special issue - Organic Electronics, vol. 16 (6), pp. 1099–1100, 2015.

[179] B. W. D’Andrade, A. Z. Kattamis, P. F. Murphy. “Flexible organic electronic devices on metal foil substrates for lighting, photovoltaic, and other applications.” Handbook of Flexible Organic Electronics: Materials, Manufacturing and Applications, Elsevier, 2014.

[180] I. Salzmann, S. Duhm, G. Heimel, J.P. Rabe, N. Koch, M. Oehzelt, Y. Sakamoto, T. Suzuki, “Structural Order in Perfluoropentacene Thin Films and Heterostructures with Pentacene”. Langmuir vol. 24(14) pp. 7294–7298, 2008.

[181] I. Kymissis, “Organic Field Effect Transistors: Theory, Fabrication and Characterization”, Springer, 2009.

[182] I. Youji, Y. Sakamoto, T. Suzuki, M. Kobayashi, Y. Gao, S. Tokito, “Organic Thin-Film Transistors with High Electron Mobility Based on Perfluoropentacene” Japanese Journal of Applied Physics, vol. 44 (6) pp. 3663-3668, 2005.

[183] L.L Chua, J. Zaumseil, J.F. Chang, E.C.W. Ou, K.H.P. Ho, H. Sirringhaus, R.H. Friend, “General observation of n-type field-effect behaviour in organic semiconductors”, Nature, vol. 434(7030) pp. 194-199, 2005.

[184] J.H.R Gao, J Li, L.Q Li, Q. Meng, H. Jiang, H.X. Li, W.P Hu, “High-Performance Field-Effect Transistor Based on Dibenzo[d,d′]thieno[3,2-b;4,5-b′]dithiophene, an Easily Synthesized Semiconductor with High Ionization Potential”, Advanced Materials vol. 19(19), pp. 3008-3011, 2007.

[185] M.B. Herbert, “The work function of the elements and its periodicity”, Journal of Applied Physics vol. 48(11) pp. 4729-4733, 1977.

[186] M. Batzill, U. Diebold, “The surface and materials science of tin oxide”, Progress in Surface Science, vol. 79(2), pp. 47-154, 2005.

[187] J.A. Rogers, A. Dodabalapur, Z. Bao, H.E. Katz, “Low-Voltage 0.1 mm Organic Transistors and Complementary Inverter Circuits Fabricated with a Low-Cost form of Near-Field Photolithography”, Applied Physics Letters, vol. 75(7)pp. 1010-1012, 1999.

[188] N.R. Christopher, C.D. Frisbie, D.F.A. da Silva, J.L. Bredas, P.C. Ewbank, K.R. Mann, “Introduction to Organic Thin Film Transistors and Design of n-Channel Organic Semiconductors”, Chemistry of Materials vol. 16(23) pp. 4436-4451, 2004.

[189] S.O. Kasap, “Principles of electronic materials and devices” McGraw-Hill, 2006.

[190] D.K. Schroder, “Semiconductor Material and Device Characterization”, New York, NY: Wiley, 2006.

[191] S.M. Mok, F. Yan, H. L. W. Chan, “Organic phototransistor based on poly (3-hexylthiophene)/TiO2 nanoparticle composite”, Applied Physics Letters, vol. 93 (2), pp. 023310 (1–3), 2008.

[192] S.C.B. Mannsfeld, B.C. Tee, R.M. Stoltenberg, C.V.H. Chen, S. Barman, B.V. Muir, A.N. Sokolov, C. Reese, Z. Bao, “Highly sensitive flexible pressure sensors with microstructured rubber dielectric layers”, Nature materials, vol. 9(10), pp. 859-864, 2010.

[193] K.S. Johnson, J.A. Needoba, S.C. Riser, W.J. Showers, “Chemical sensor networks for the aquatic environment”, Chemical Reviews, vol. 107(2), pp. 623-640, 2007.

[194] C. Bartic, G. Borghs, “Organic thin-film transistors as transducers for (bio) analytical applications. Analytical and Bioanalytical Chemistry, vol. 384, pp. 354–365, 2006.

[195] M. Berggren, R.A. Dahlfors, “Organic bioelectronics”, Advanced Materials, vol. 19(20), pp. 3201-3213, 2007.

[196] R.M. Owens, G.G. Malliaras, “Organic electronics at the interface with biology”, MRS bulletin, vol. 35(06), pp. 449-456, 2010.

[197] P. Lin, F. Yan, “Organic Thin-Film Transistors for Chemical and Biological Sensing”, Advanced materials, vol. 24(1), pp. 34-51, 2012.

CHAPTER III

FABRICATION OF FLEXIBLE ORGANIC THIN FILM TRANSISTORS (OTFTS) BASED HUMIDITY SENSORS

3.1. Introduction

In recent years, humidity sensors have played a vital role with numerous applications in our day to day life, such as human comfort, food packaging, health monitoring, electric device storage and agricultural based industries [1-3]. Several studies on the different types of humidity sensors such as capacitive/resistive [4], optical [5], thermal [6] and surface acoustic wave sensors [7] have been reported. An important advantage of capacitive/resistive humidity sensors is the capability of integrating them into external circuits, without additional conditioning circuitry. Recently, the use of OTFTs for humidity sensing has also been reported [8]. OTFT based sensors have demonstrated higher sensitivity when compared to the two-terminal capacitive or resistive devices because combine of a two-terminal device and an amplifier, in which the drain current may be modulated with a gate bias [9]. This enables a wide range of applications for the OTFT based sensors. To name a few, biochemical detection [10-11], gas sensing [12-13], environmental monitoring [14-15] and artificial skin [16-17]. Typically, the OTFT based humidity sensors have been fabricated using Si based techniques [8]. This has led to the research of using PE techniques as an alternative for the manufacturing of OTFT based flexible humidity sensors.

In this work, an OTFT based humidity sensor is fabricated using traditional printing methods and conventional lithographic techniques on a flexible polyethylene terephthalate (PET) substrate. For first generation OTFT, the bottom gate electrode

and dielectric layers are deposited using gravure printing, which is a versatile process, known for its high throughput, high quality printing, high print speeds, uniformity of the printed layer and variable ink film thickness. For second generation OTFT, the bottom gate electrode is deposited using a thermal evaporation technique and the dielectric layer is spin coated. The source and drain interdigitated electrodes (IDE's) are deposited by means of screen printing, which is a push through process and capable of printing relatively thick layers. Inkjet printing, a non-impact printing process, is used to deposit the active semiconducting layer. The response of the printed sensor towards varying humidity levels is analyzed and reported.

3.2. Materials and Chemicals

Melinex® ST 505, a 130 µm thick flexible PET, from DuPont Teijin Films is used as a substrate. A silver nano particle ink (TEC-PR-020), with particle size ranging from 20 nm to 50 nm, from InkTec Inc, was used for metalizing the bottom gate electrodes of the first generation OTFT. A transparent UV clear coating from Ecology Coatings Inc. was employed as a dielectric ink. Acheson Electrodag 479SS silver flake ink from Henkel was used for metalizing the IDEs. Aluminum (Al) with wire diameter of 0.58 mm, 1,2-dichlorobenzene solvent and 6,13-bis(triisopropylsilylethynyl) pentacene (TIPS pentacene) (in powder form) was purchased from Sigma Aldrich Chemical company. Spring loaded small outline integrated chip (SOIC) test clips (14 pin), from Pomona® Electronics, are used to connect the OTFT to a Keithley 4200 semiconductor characterization system (SCS), which was used for measuring the output characteristics of the printed OTFT sensor. An environmental test chamber 6010 from Caron was used to control the humidity levels on the sensor.

3.3. Pentacene and TIPS Pentacene

Pentacene, a commonly used p-type organic semiconductor, is a polycyclic aromatic hydrocarbon, which consists of five linearly arranged benzene rings [18]. Pentacene suffers with low solubility issues in a wide range of organic solvents and is usually thermally evaporated [19]. Moreover, pentacene OTFTs exhibit poor device characteristics attributed to the increased injection barrier between the metal electrodes and semiconductor. The presence of a large energy barrier indicates a high contact resistance at the channel electrode interface [20]. This problem can be overcome by increasing the conductivity through the addition of two triisopropylsilylethynyl (TIPS) groups at C6 and C13 position of the pentacene molecule, yielding a molecule called TIPS Pentacene [6,13-bis (triisopropylsilylethynyl) pentacene] (shown in Fig. 3.1 (b)) [21]. Recently tremendous attention has been devoted to TIPS pentacene owing to its high mobility, increase in solubility in a range of common organic solvents and a good environmental stability at ambient conditions which makes it easy to process into devices [22-26].

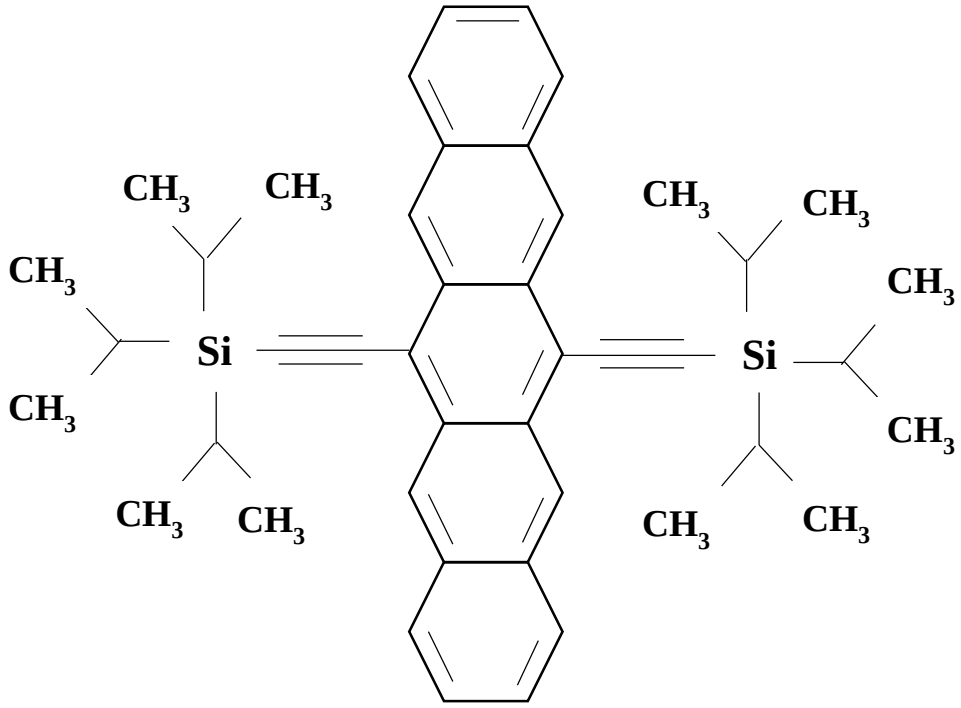

Figure 3.1. Molecular structure for TIPS pentacene.

3.4. Fabrication and Characterization of First Generation OTFTs

3.4.1. Fully Printed First Generation OTFT Fabrication

A bottom gate bottom contact configuration, known for lower off currents and better overall characteristics [27], was adopted in this work for the fabrication of an OTFT based sensors. A schematic of the OTFT design is shown in Fig. 3.2. Bottom gate electrode and dielectric layers of the OTFT were gravure printed using an AccuPress® level 3 precision gravure printer. The electrodes were design in Adobe Illustrator®. A chromium coated copper cylinder, which was employed for the gravure printing of the bottom gate electrode and dielectric layers, was engraved by RotaDyne, USA. The designs for the bottom gate electrode and dielectric layers were Scheppers and electromechanically engraved, respectively. Cells engraved for both the layers mimic a square cup with cell depth and width of 30 µm and 85 µm, respectively. The photograph of the engrave cylinder is shown in Fig. 3.3. Dimensions of the bottom electrode were designed as 12 mm × 12 mm. Silver nano particle based

ink was used as metallization of bottom gate electrode. A 22.2 mm wide and 0.15 mm thick MDC® ultra-life doctor blade from Daetwyler was used to print the bottom electrodes. A photograph of the printed electrodes is shown in Fig. 3.4

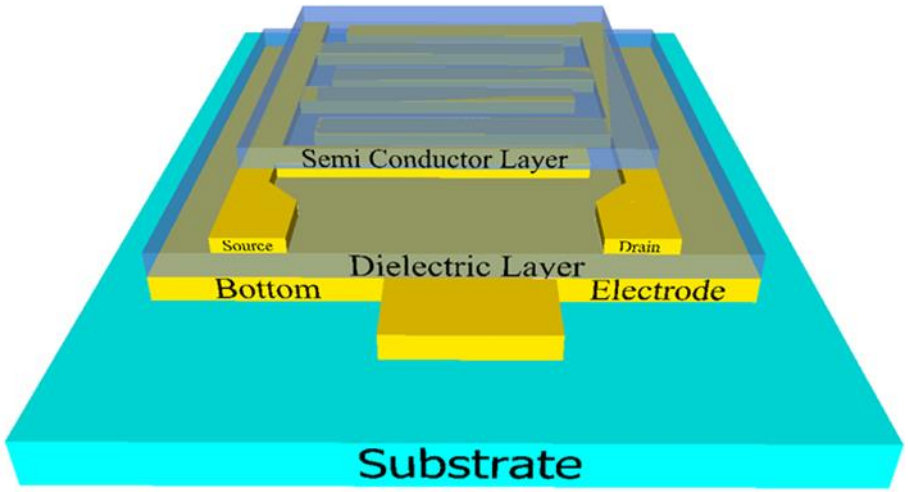

Figure 3.2. Schematic of the all printed organic thin film transistor.

Figure 3.3. Gravure cylinder showing the engraved bottom electrode and dielectric layers.

Thickness and roughness of the printed layers were measured with a vertical scanning interferometry (VSI) using a WYKO RST-Plus microscope. The average thickness and RMS roughness for the bottom gate electrode was 396 ± 28 nm and 112 ± 13 nm, respectively. The sheet resistivity of the printed layer was measured to be 0.46 ±0.07 Ω/□. UV clear coating, with dimensions of 14 mm × 14 mm, was printed as a dielectric layer. The printed layer was cured with a Fusion UV lamp at 16 rotations per minute (rpm) and two passes. The average thickness and RMS roughness

for the dielectric layer was 3.2 ±0.2 µm and 210 ±3 nm, respectively. Figure 3.5 shows the 3D image of the printed gate electrode and dielectric layers from the optical profiler.

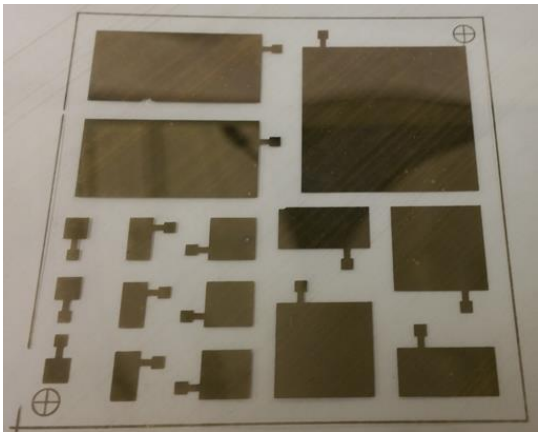

Figure 3.4. Gravure printed silver electrodes on PET.

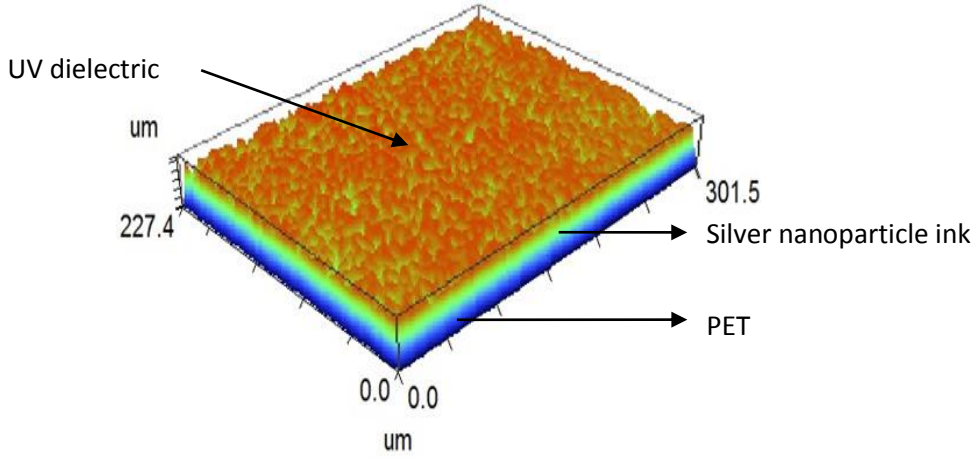

Figure 3.5. 3D output of the vertical scanning interferometry of printed silver nanoparticle ink and UV dielectric on PET.

In order to cover the higher roughness of the dielectric layer, a thick film deposition for the top electrodes was needed. A screen printing technique, which was able to deposit a thicker film, was employed to print the source and drain top electrodes. The source and drain layer, in an interdigitated geometry, was designed with 9 pair of electrodes; where each electrode has dimensions of 5200 µm length, 200 µm width and 200 µm electrode spacing, resulting in a width to length ratio (w/l)

of 26. The schematic of the IDEs is shown in Fig. 3.6 (a). A 12" ×12" stainless steel screen with 325 mesh count and 28 µm wire diameter resulting in open area of 41 % was fabricated at MicroScreen®, USA. A screen printer (AMI MSP 485) from Affiliated Manufacturers Inc. was used to deposit the source and drain top electrodes, with Ag flake ink. The printed layer was thermally cured in a conventional oven at 90 °C for 25 minutes. The average thickness, RMS roughness and sheet resistivity of the printed film were 10.5 ± 1.2 µm, 560 ± 30 nm and 0.31 Ω/□, respectively. The morphology of the screen printed silver is shown in Fig. 3.6 (b).

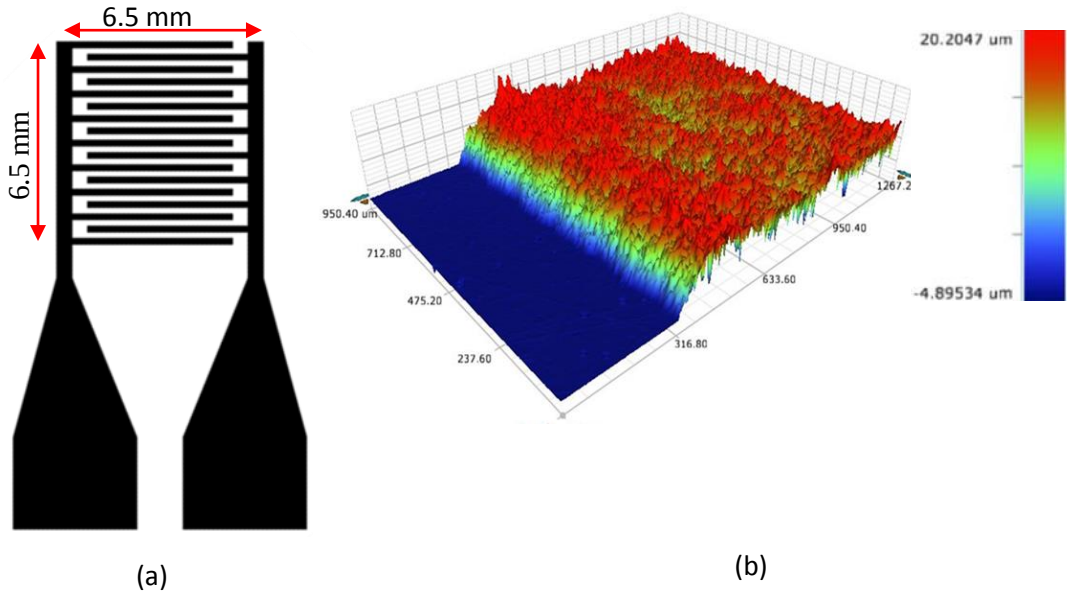

Figure 3.6. (a) Schematic of source drain IDEs, (b) screen printed silver IDEs.

TIPS pentacene (≥99% pure) in powder form was purchased from Sigma Aldrich was used without further purification. A 1 % by wt solution was obtained by dissolving 76.4 mg of TIPS pentacene in 7.6 g of 1,2-dichlorobenzene. A FUJIFILM Dimatix DMP-2831 inkjet printer was used to deposit TIPS pentacene on to the screen printed IDEs. A 10 µl cartridge was used for inkjet printing. Z number was calculated according equation 14[28].

$$Z = \frac{\sqrt{(d\rho\gamma)}}{\eta} \tag{14}$$

where ρ is the density, γ is the surface tension, d is the diameter of inkjet nozzle and η is the viscosity of the ink. The Z-number for 1% TIPS pentacene was calculated to be 40 at 20 °C. It is desirable that the surface energy of the printed UV layers be increased for better printability of the TIPS pentacene. Therefore. UV layer was exposed to a UV ozone treatment for 20 minutes. Contact angle measurements of deionized water and methyl iodide were performed before and after the surface treatment.. Surface energies were calculated using Owens Wendt Method [28]. The surface energy of the printed layer was increased from 38.9 mN/m to 48.8 mN/m. The substrate temperature for the printing was chosen as 60 °C as the higher temperatures are known to increase the uniformity in the film formation of TIPS pentacene [31]. The semiconducting layer to be printed was designed in Adobe Illustrator and imported to Dimatix software as a .bmp file. The settings used for file conversion was 1270 dpi (drops per inch) to be used as 20 ds (drop spacing). The thickness of inkjet printed layer was measured to be 432 ± 8 nm. The 3D optical profilometry picture of the printed layer is shown in Fig. 3.7. The photograph of the fully printed OTFT is shown in Fig. 3.8.

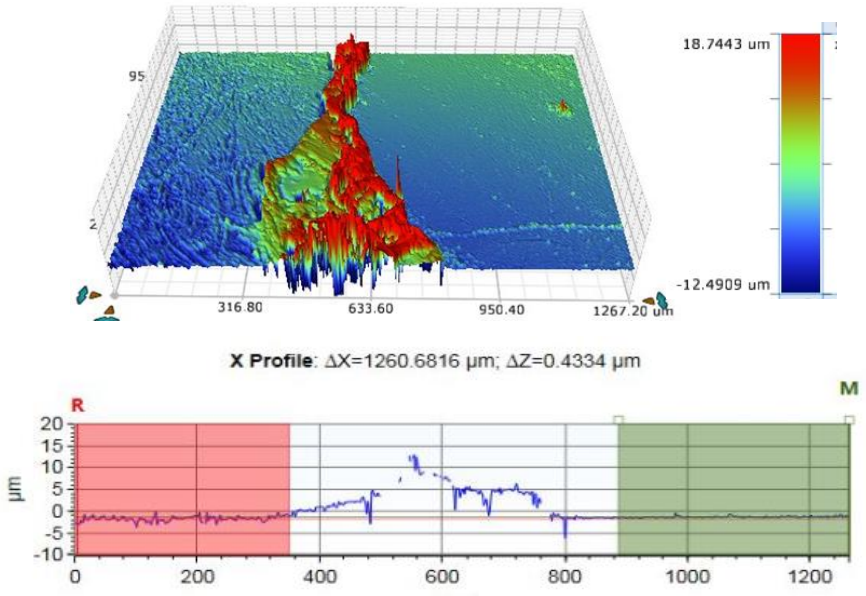

Figure 3.7. 3D morphology of inkjet printed pentacene

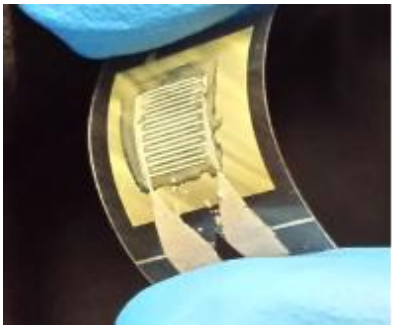

Figure 3.8. Fully printed organic thin film transistor

3.4.2. Electrical Characterization of Fully Printed OTFT

Initially, the I-V characteristics of the printed OTFT were studied at ambient conditions using a SCS over the range of -180 V to +180 V. The SCS was connected to the OTFT using SOIC test clips. The test setup is shown in Fig. 3.9.

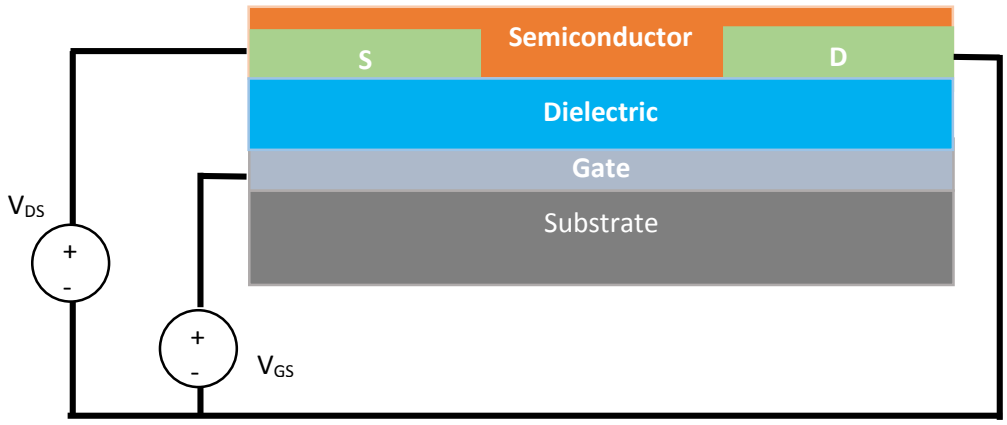

Figure 3.9. Test setup for IV characteristics of the OTFT

Figure 3.10 shows the I-V characteristics of the fully printed OTFT at ambient conditions. For this test, the OTFT was measured over a range of 180 V to -180 V for gate-to-source voltage (V_{GS}) and drain-to-source voltages (V_{DS}). It was observed that the I_D was inversely proportional to V_{GS} and directly proportional to V_{DS}, which are the typical I-V characteristics of a p-type OTFT. Figure 3.11 shows the drain current modulation with respect to gate voltage. From the fitted line in square root plot of the transistor characteristics, the threshold voltage is approximately 130 V.

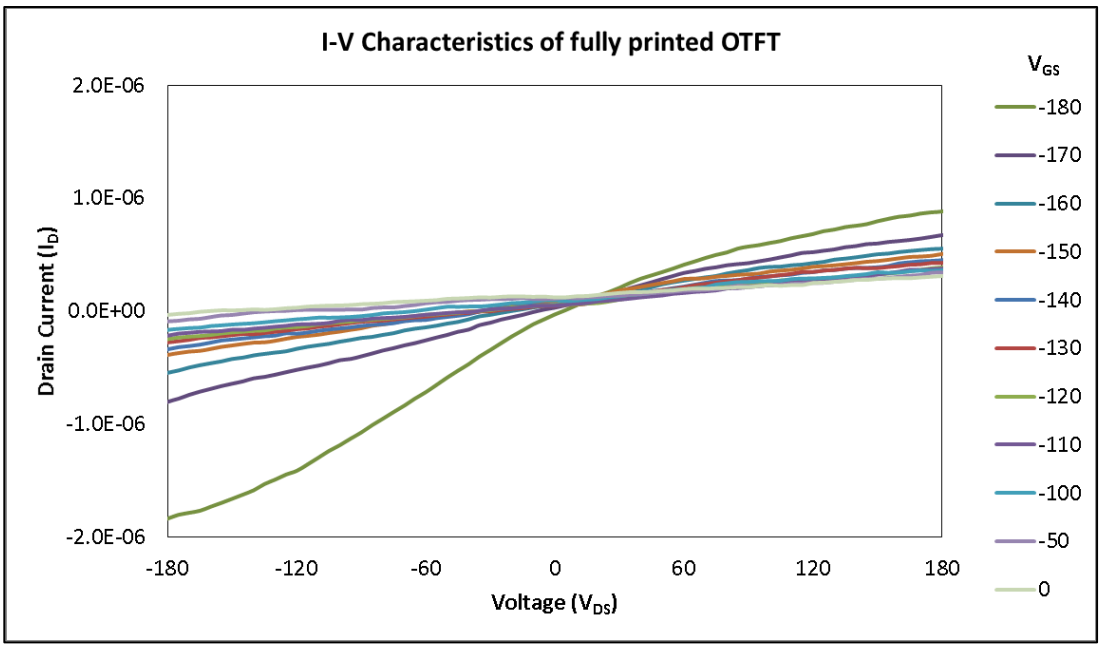

Figure 3.10. I-V characteristics of the fully printed TIPS pentacene OTFT

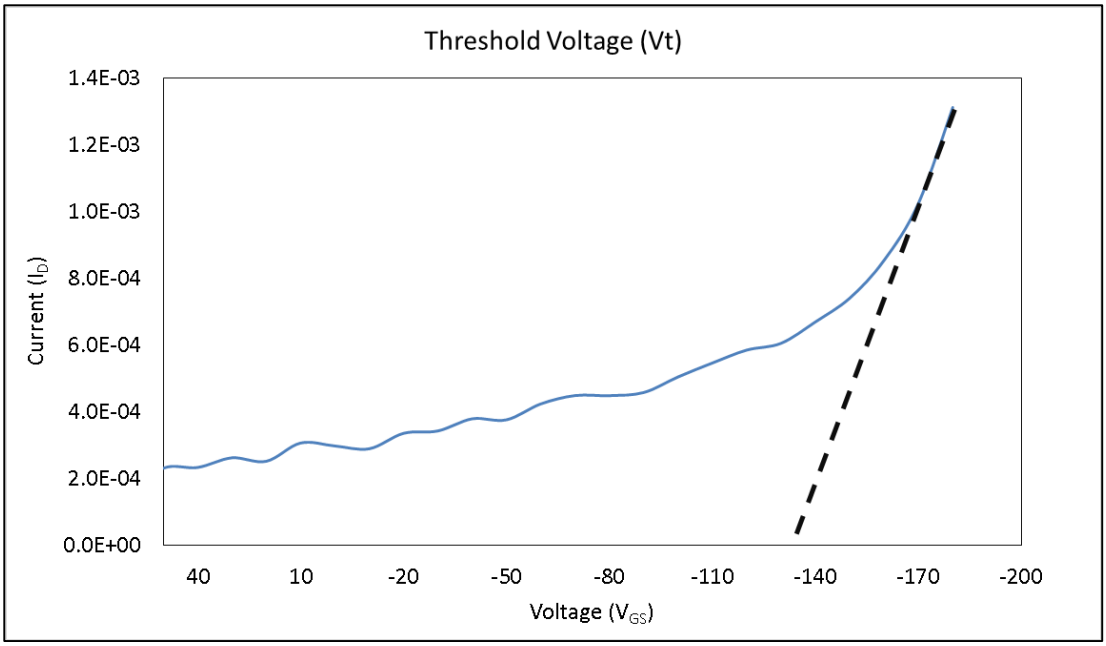

Figure 3.11. Threshold voltage from transfer characteristics

3.4.3. Issues Related First Generation OTFTs

The fabricated OTFT demonstrated the proof-of-concept of fully printed OTFTs. Measured I-V characteristics showed the working p-type behavior of the OTFT. The author fabricated a second generation OTFT with the aim of overcoming a major problem that was observed based on studies performed in the first generation OTFTs. A detailed analysis revealed the need for better fabrication of OTFT.

The operating voltages for the first generation OTFT was around 180 V. It was noticed that these voltages was very impractical for real time applications. Further investigation revealed that the higher operating voltages were due to the thickness of the dielectric layer. The measured thickness of the dielectric layer was 3.2 ±0.2 µm. The thickness dependence of the threshold voltage (V_t) is given by [31].

$$V_t = E_T t_{dielectric} + \varphi_{ms} \tag{15}$$

where E_T is the threshold field, constant for a given set of materials, $t_{dielectric}$ is the thickness of the dielectric layer and φ_{ms} is the work function difference between the dielectric layer and semiconducting layer. From eq. 2, the threshold voltage is

directly proportional to the thickness of the dielectric layer. In the second generation OTFT, the thickness of the dielectric layer was decreased by using spin coating instead of gravure printing. Spin coating is known for depositing uniform thin films. Depending upon the spin speed, the expected thickness was around a few hundred nano meters. However, with this lower thickness, the surface roughness of the bottom electrode will have a significant impact, potentially causing pinholes. To overcome this concern, in the second generation OTFT, gravure printing of the bottom electrode was replaced by thermal evaporation.

3.5. Fabrication and Characterization of Second Generation OTFT

To overcome issues mentioned in the previous section, the bottom electrode and dielectric layers in second generation OTFT were deposited using thermal evaporation and spin coating, respectively.

3.5.1. Fabrication of Second Generations OTFTs

Aluminum of 99 % purity is available commercially in amorphous form and has a sublimation temperature of approximately 1000 °C. A 0.12 cm × 5 cm Al layer was evaporated. The shadow mask used in this work was made of PET which is cut in the areas were Al needs to be deposited. Figure 3.12 shows the schematic of the thermal evaporation setup. Al wire was wrapped onto a tungsten wire for electrode connection. The sample was placed at 5 cm above the tungsten wire.

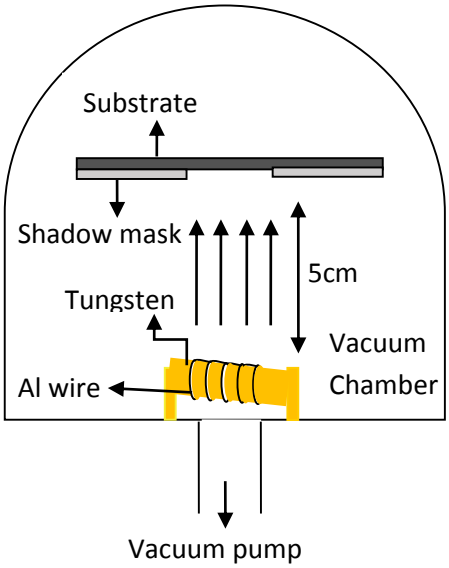

Figure 3.12. Schematic of thermal evaporator.

Then vacuum in the chamber was pumped down to 1×10^{-6} mbar. Evaporation of Al was done for 20 minutes. Average thickness and RMS roughness of the evaporated sample was measured to be 320 ± 1 nm and 183 nm, respectively. 3D output of the vertical scanning interferometry of evaporated Al layer is shown in Fig. 3.13

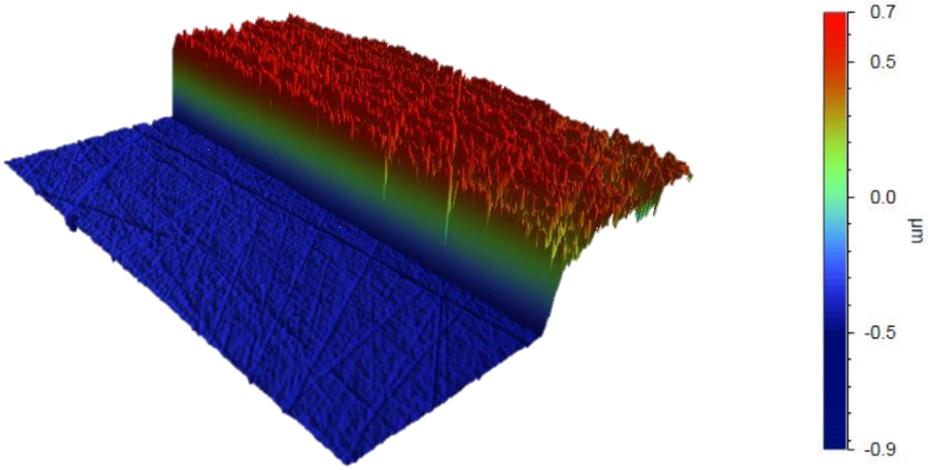

Figure 3.13. 3D output of the vertical scanning interferometry of evaporated Al layer

A thin UV clear dielectric was spin coated onto the Al coated PET at a spin speed of 2000 rpm for 20 seconds. The samples were then cured with a Fusion UV

lamp at 16 rpm and two passes. The average thickness and RMS roughness for the dielectric layer was 263 ± 15 nm and 109 ± 11 nm, respectively. Figure 3.14 shows the optical profiler output of the dielectric layer.

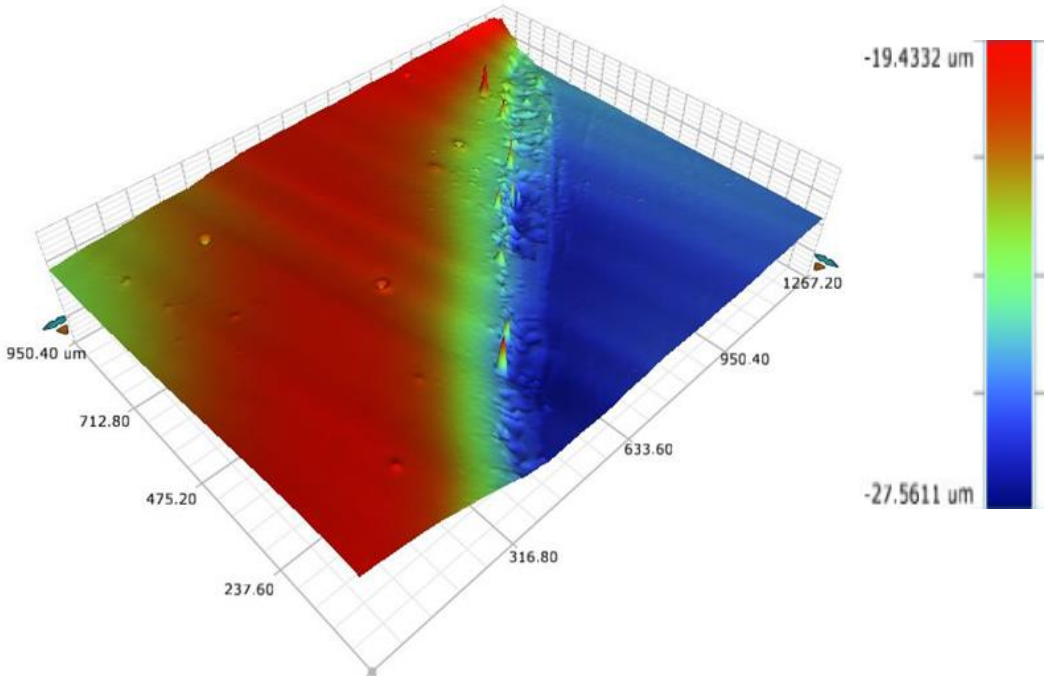

Figure 3.14. 3D output of the vertical scanning interferometry of spin coated dielectric layer.

Top source and drain electrodes and pentacene layers were printed using screen printing and inkjet printing, respectively. The materials and process variables used for these two layers were the same as the first generation OTFT. Figure 3.15 shows the picture of second generation OTFT.

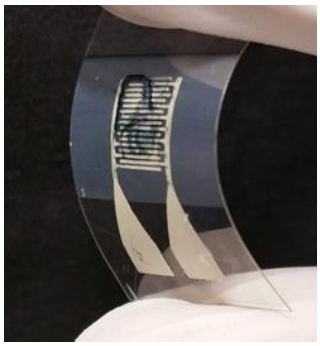

Figure 3.15. Second generation organic thin film transistor

3.5.2. Electrical Characterization of Second Generation OTFTs

The testing setup (shown in Fig 3.9) previously used for electrical characterization of the first generation OTFT was also used to characterize the second generation OTFTs. Figure 3.16 shows the IV characteristics of the second generation OTFT. It was observed that the drain current was inversely proportional to V_{GS} and directly proportional to V_{DS}, which are the typical I-V characteristics of a p-type OTFT.

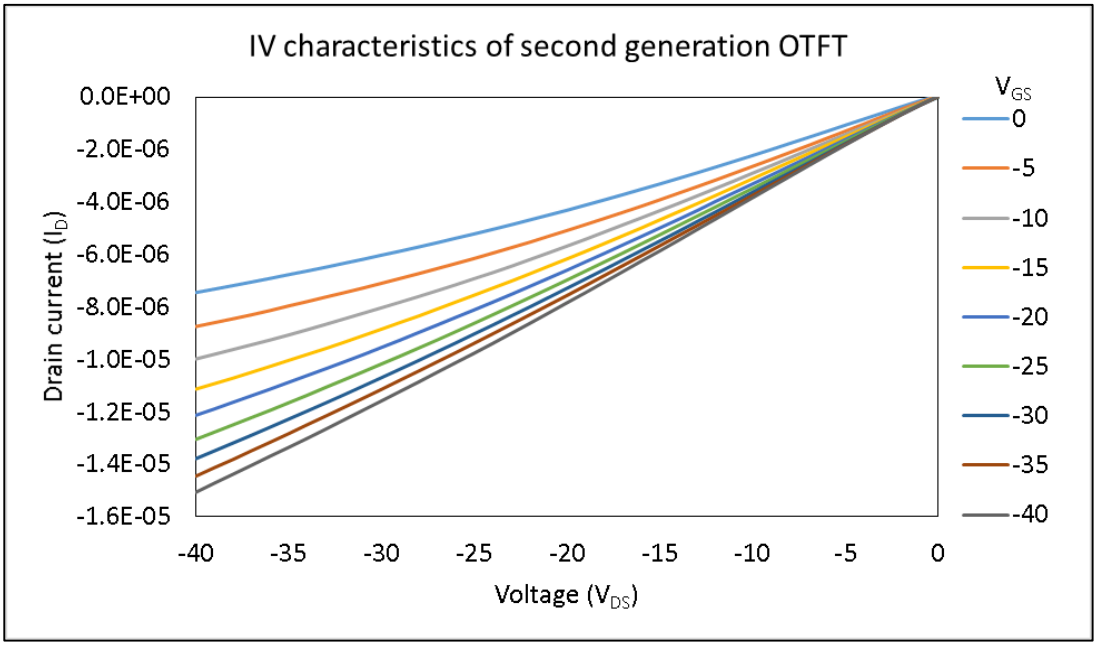

Figure 3.16. I-V characteristics of second generation TIPS pentacene OTFT

From Fig. 3.16, it can be noticed that the fabricated device does not saturate. Higher drain to source voltages were needed for the device to saturate. However, the thickness of the dielectric layer has limited the maximum voltage that can be applied. The dielectric layer is 263 nm thick and begins to breaks down at voltage exceeding 40 volts. Another reason could be the work functions of silver electrodes and semiconductor layer. The highest occupied molecular orbital (HOMO) level TIPS pentacene was reported as 5.30 eV [32]. It is far higher compared to the work function of silver, which is reported as 4.14 eV [32]. This difference leads to an increase in the

contact resistance between the TIPS pentacene layer and silver source drain electrodes. This could have a higher impact on the saturation currents. Figure 3.17 shows the square root for drain current with respect to gate voltage at drain to source voltage of -40 V. According to the fitted line cure, the threshold voltage is approximately 4 V and mobility is determined to be 0.03 $cm^2V^{-1}s^{-1}$.

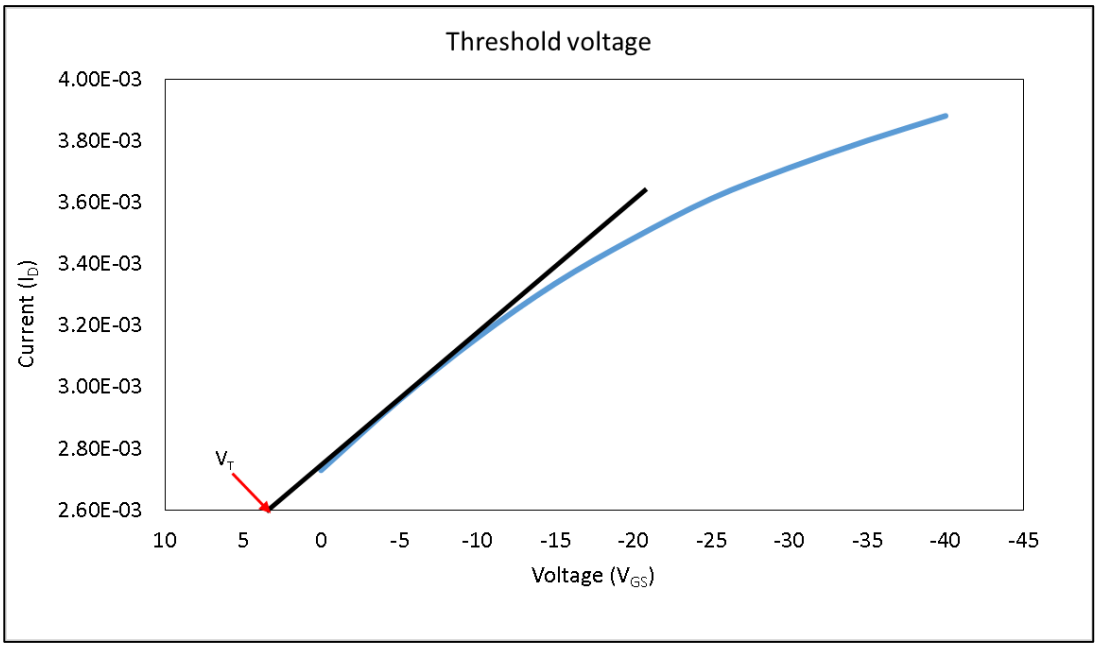

Figure 3.17. Transfer characteristics of second generation TIPS pentacene OTFT

3.6. Response of OTFT Based Sensor Towards Relative Humidity

The response of the second generation OTFTs has been tested while varying the relative humidity. The experiment setup is shown in Fig. 3.18. The individual sensors were placed in a Caron 6010 environmental chamber in order to investigate their response to humidity. The sensors were connected to a 4200 SCS using SOIC test clips. The I-V characteristics of the OTFT based humidity sensors, at different humidity levels, were studied. All measurements were conducted at room temperature. Calibration for the wires and probes was performed prior to measurements.

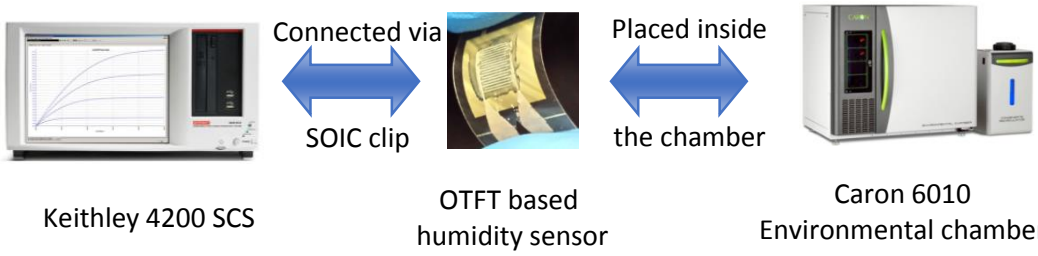

Figure 3.18. Experiment setup

Figure 3.19 and Fig. 3.20 shows the response of the second generation OTFT sensor to relative humidity at 0 V and -40 V V_{GS}, respectively. Initially, the chamber was kept at 25% RH and allowed to stabilize.. Then the relative humidity in the chamber was increased from 25 %RH to 85 %RH with the steps of 5 %RH. The I_D at different humidity levels, ranging from 25 %RH to 85 %RH was measured at -40 V gate-to-source voltage and drain-to-source voltage.

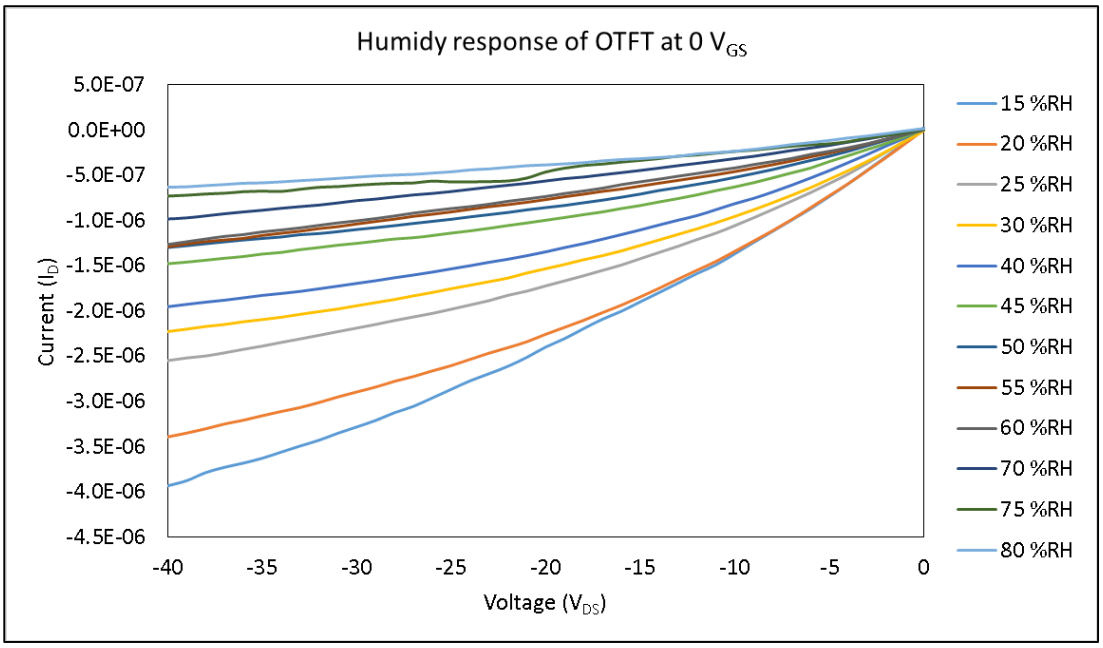

Figure 3.19. Humidity response of TIPS pentacene OTFT at 0 V V_{GS}

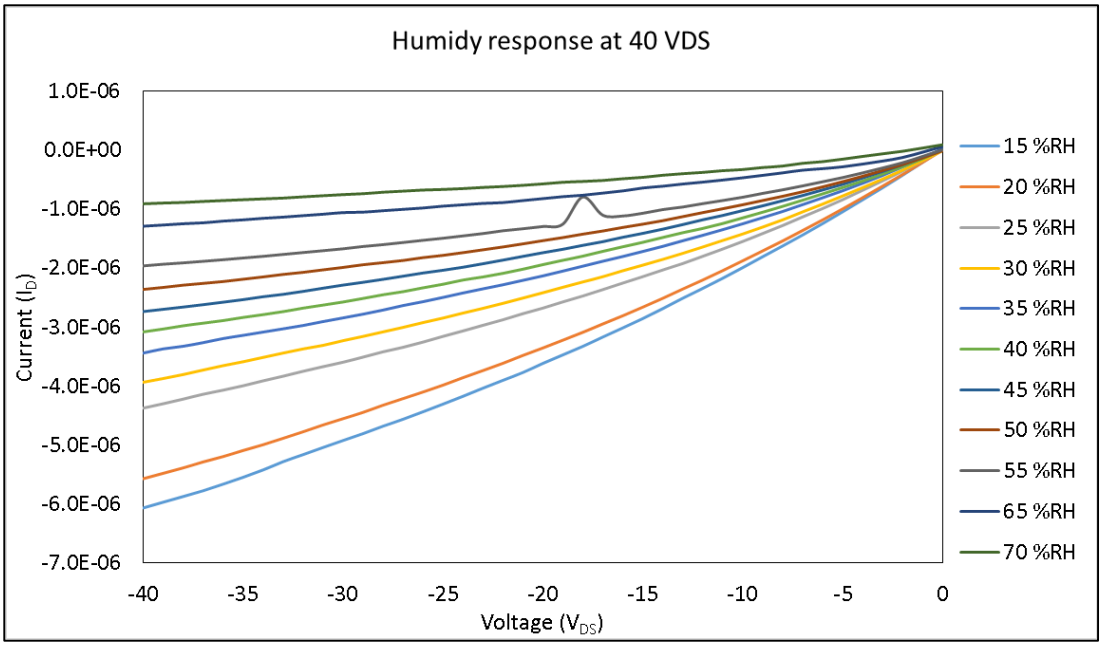

Figure 3.20. Humidity response of TIPS pentacene OTFT at -40 V V_{GS}

From these results, it was observed that the drain current is directly proportional to the drain to source voltage and inversely proportional to the relative humidity, i.e., drain current was reduced with increase in relative humidity in the chamber. This behavior was expected based on the following analysis. The structure of pentacene films is relatively amorphous, with large gaps between the grains that run nearly to the bottom of the first few monolayers on the substrate [32]. Charge transport is restricted because of the trapping of holes at the grain horizon [33-34]. As pentacene is highly hydrophobic, water molecules can easily diffuse through the gaps of pentacene and interact with the trapped carriers because the electric field is altered at the grain boundaries. The presence of a polar molecule decreases the rate of charge transport of an organic material by inducing charge–dipole interactions, and thus increasing the amount of energetic disorder [35-36]. Together, these factors contribute to the hole mobility and translate into changes in the drain current.

A statistical analysis for the reproducibility of the response was also performed by investigating the humidity response of three different sensors. Figure

3.21 shows the response of the sensor towards relative humidity at -40 V_{GS} and -40 V_{DS}. The relative response, $(I_{measured} - I_{15\,\%RH})/\, I_{15\,\%RH}$, measured for the fabricated devices resulted in an average percentage change in the drain current of 12% to 81% as the relative humidity increased from 15% RH to 85% RH. The sensitivity of the sensor is determined as 0.9% per %RH.

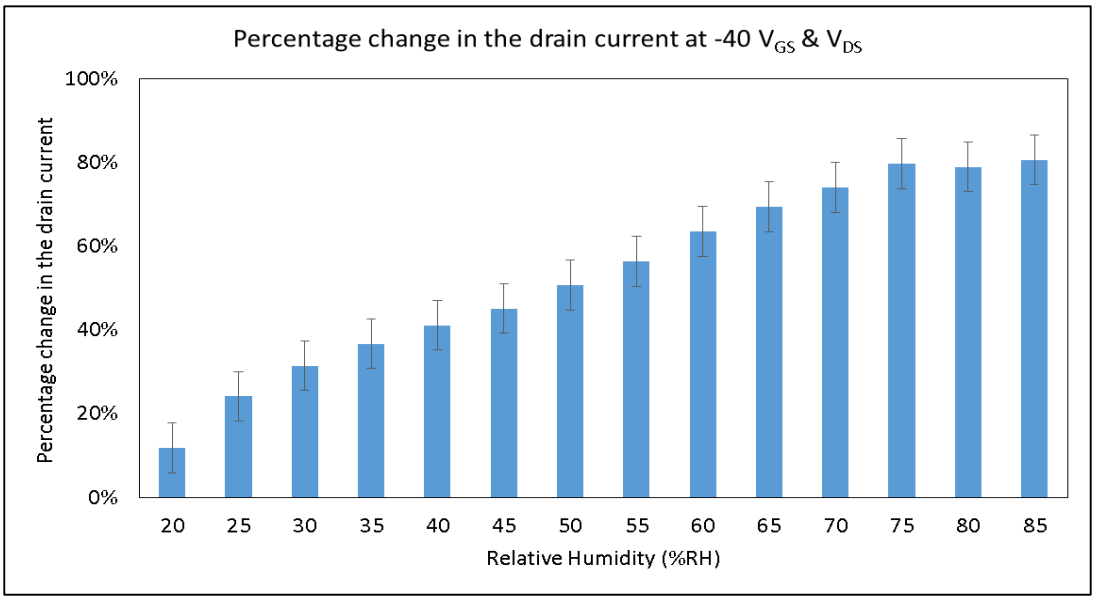

Figure 3.21. Humidity response of TIPS pentacene OTFT at -40 V_{DS} & V_{GS}

It can be noticed that the standard deviation error bars have overlaps. The accuracy of the environmental chamber for maintaining relative humidity level is 2 %RH. This will have a significant effect on the error bars. In this study, error in the humidity level maintained in the chamber has not been considered. The overlaps in error bars can be reduced by considering the humidity levels in steps of 15% RH. Figure 3.22 and Fig. 3.23 shows the average response of the sensors towards relative humidity with steps of 15% RH at -40 V_{GS} and -40 V_{DS}. It can be observed from Fig. 3.21, that the percentage change in the average drain current of the fabricated sensors was 12%, 37%, 51% 69% and 79% with an average standard deviation of 3%,

4%, 7%, 6% and 6.7% observed for 20% RH, 35% RH, 50% RH, 65% RH, and 80% RH, respectively.

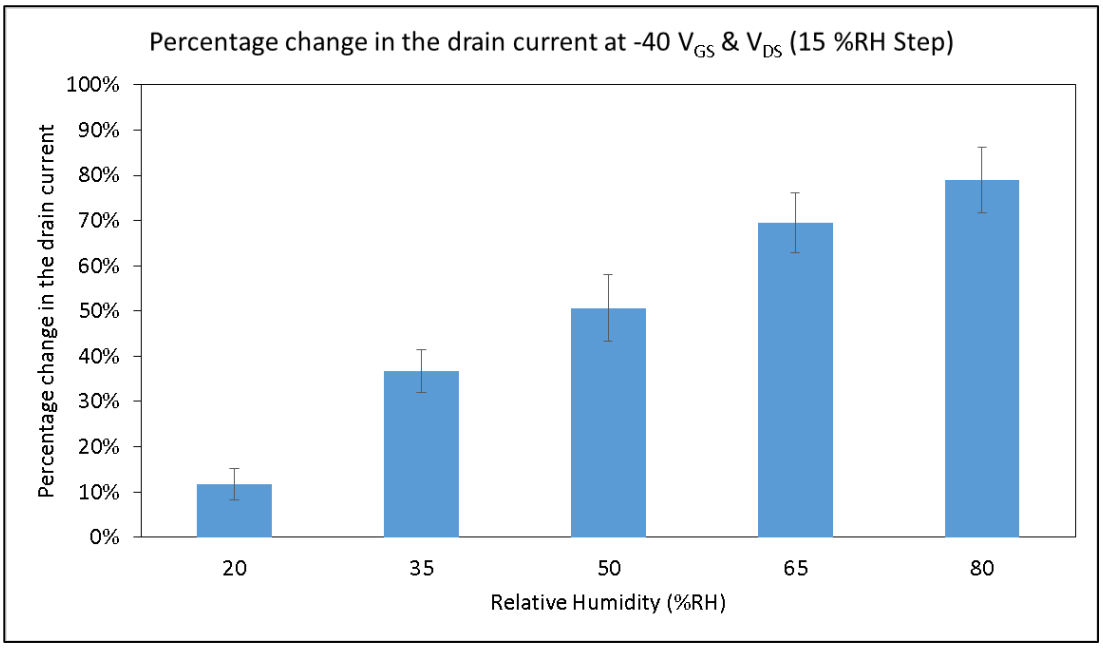

Figure 3.22. Humidity response of TIPS pentacene OTFT at -40 V_{DS} & V_{GS} (15% RH step) (Starts at 20 %RH)

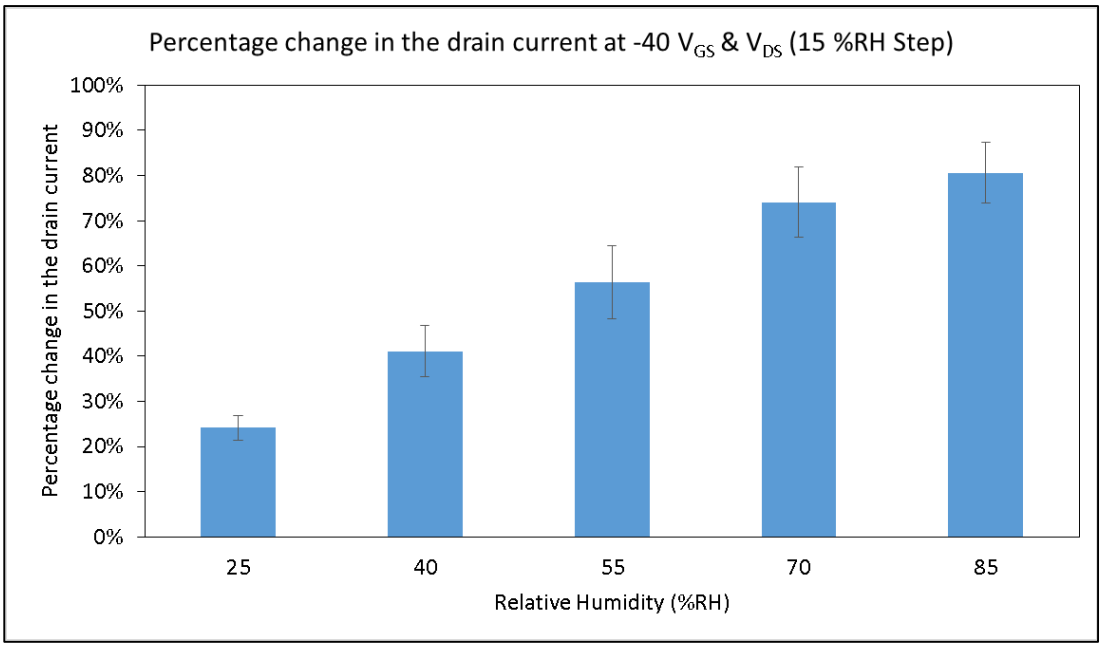

Figure 3.23. Humidity response of TIPS pentacene OTFT at -40 V_{DS} & V_{GS} (15% RH step) (Starts at 25 %RH)

Similarly, percentage change in the average drain current of the fabricated sensors of 24%, 41%, 56% 74% and 81% with an average standard deviation of 2%, 5%, 8%, 7% and 6.7% was observed for 25% RH, 40% RH, 55% RH, 70% RH, and 85% RH, respectively. From this it can be concluded that the fabricated sensor work with a resolution of 15% RH.

3.7. Summary

In this chapter, the author briefly discussed the importance of OTFT based humidity sensors. A detailed account of the experimental tasks involved in this work was then presented. This includes the materials, chemical and devices used; fabrication and electrical characterization of first and second generation OTFTs; issues related to first generation of OTFTs; and the experiment setup was presented. Finally, the response of the second generation OTFT towards relative humidity was also presented.

To summarize, a first generation OTFT was fabricated with traditional printing techniques. The response of the fully printed OTFT was studied at ambient conditions. However, from the electrical characterization of the OTFT, it was concluded that the OTFT had a very high threshold voltage of 130 V. It was noticed that this high voltage is due to the high thickness (3.2 µm) of dielectric layer. For the second generation OTFT, the printing step of the dielectric layer was replaced by spin coating. The measured thickness of the spin coated dielectric layer was 263 nm. The bottom electrode of the OTFT was also evaporated with Al to overcome pinhole issues caused by the thinner dielectric layer. Electrical characterization of the second generation OTFT resulted in a threshold voltage of 4 V. The response of the fabricated sensor towards wide range of humidity from 15 %RH to 85 %RH was studied in an environmental chamber. Sensitivity of 0.9 % change in average drain

current for 1 %RH change was recorded. It was also noticed that the fabricated sensor has a resolution of 15 %RH. The obtained results showed that the sensor is capable of sensing wide range humidity and could be used in OTFT based humidity sensing applications.

In the following chapter, the author presents a project that involved the development of an electrochemical sensor fabricated using screen. The author discusses the design, fabrication and characterization of the electrochemical sensor and synthesis of sensing layers. The experiment setup, testing and results obtained are discussed and presented.

References

[1] R. Xuan, Q. Wu, Y. Yin, J. Ge, “Magnetically assembled photonic crystal film for humidity sensing”, Journal of Materials Chemistry, vol. 21, pp.3672-3676, 2011.

[2] W. Vautz, J.I. Baumbach, M. Westhoff, K. Züchner, E.T.H. Carstens, T. Perl, “Breath sampling control for medical application”, The International Journal for Ion Mobility Spectrometry, vol.13, pp. 41-46, 2010.

[3] B. Wang; M.K. Law, A. Bermak, “A low-cost capacitive relative humidity sensor for food moisture monitoring application”, 4th Asia Symposium on Quality Electronic Design (ASQED), pp.95-99, 2012.

[4] A.S.G. Reddy, B.B. Narakathu, M.Z. Atashbar, M. Rebros, E. Rebrosova, B.J. Bazuin, M.K. Joyce, P.D. Fleming, A. Pekarovicova, “Printed capacitive based humidity sensors on flexible substrates”, Sensors Letters vol.9, pp. 869-871, 2011.

[5] Y.J. Liu, J. Shi, F. Zhang, H. Liang, J. Xu, A. Lakhtakia, S.J. Fonash, T.J. Huang, “High-speed optical humidity sensors based on chiral sculptured thin films”, Sensors and Actuators B Chemical vol.156, pp. 593-598, 2011.

[6] O. Legendre, H. Bertin, H. Mathias, F. Mailly, S. Megherbi, “Novel humidity sensing method based on the transient response of a micro-heater”, Sensors Actuators A Physical, vol.192, pp. 92-100, 2013.

[7] Y. Liu, C.H. Wang, Y. Li, “BCB film based SAW humidity sensor”, Electronic Letters vol.47, pp.1012-1014, 2011.

[8] Z.T. Zhu, J.T. Mason, R. Dieckmann, and G.G. Malliaras, “Humidity sensors based on pentacene thin-film transistors”, Applied Physics Letters, vol.81, pp.4643- 4645, 2002.

[9] P. Lin, F. Yan, “Organic thin-film transistors for chemical and biological sensing”, Advanced Materials vol.24, pp. 34-51, 2012.

[10] A. Spanu, S. Lai, P. Cosseddu, A. Bonfiglio, M. Tedesco, S. Martinoia, “Organic FET device as a novel sensor for cell bioelectrical and metabolic activity recordings”, IEEE/EMBS Conference NER pp. 937-940, 2013.

[11] F. Werkmeister, B. Nickel, “Towards flexible organic thin film transistors (OTFTs) for biosensing”, Journal of Materials and Chemistry B, vol. 1, pp. 3830-3835, 2013.

[12] W. Dan, Y. Jiang, H. Tai, G. Xie, X. Li, C. Fu, Z. Wu, “The formaldehyde OTFT sensor based on the airbrushed P3HT/ZnO composite thin film”, Key Engineering Materials, vol. 531, pp. 400-403, 2013.

[13] J.E. Royer, E.D. Kappe, C. Zhang, D.T. Martin, W.C. Trogler, A.C. Kummel, “Organic thin-film transistors for selective hydrogen peroxide and organic peroxide vapor detection”, Journal of Physical Chemistry C, vol.116, pp. 24566-24572, 2012.

[14] D. Briand, A. Oprea, J. Courbat, N. Bârsan, “Making environmental sensors on plastic foil”, Materials Today, vol.14, pp.416-423, 2011.

[15] K.S. Johnson, J.A. Needoba, S.C. Riser, W.J. Showers, “Chemical sensor networks for the aquatic environment”, Chemical Reviews vol.107, pp.623-640, 2007.

[16] S.C.B. Mannsfeld, B.C.K. Tee, R.M. Stoltenberg, C.V. H-H. Chen, S. Barman, B.V.O. Muir, A.N. Sokolov, C. Reese, Z.N. Bao, “Highly sensitive flexible pressure sensors with microstructured rubber dielectric layers”, Nature Materials vol.9, pp.859-864, 2010.

[17] S.J. Benight, C. Wang, J.B.H. Tok, Z. Bao, “Stretchable and self-healing polymers and devices for electronic skin, Progress in Polymer Science vol.38, pp. 1961-1977, 2013.

[18] Afzali, C.D. Dimitrakopoulos, T.L. Breen, “High-Performance, Solution-Processed Organic Thin Film Transistors from a Novel Pentacene Precursor” Journal of the American Chemical Society, vol. 124 (30), pp. 8812-8813, 2002.

[19] M.R. Perez, “Organic thin-film transistors for flexible CMOS integration” 2013

[20] K.S. Lee, “Water-dispersible, conductive polyaniline for organic thin-film electronics”, ProQuest, 2007.

[21] M.H. Choi, J. Jang, “Effect of SAM layer on bias-stability of inkjet printed TIPS pentacene thin-film transistor”, Current Applied Physics, vol. 12, pp. 6-9, 2012.

[22] M.W. Lee, G.S. Ryu, Y.U. Lee, C. Pearson, M.C. Petty, C.K. Song, “Control of droplet morphology for inkjet-printed TIPS-pentacene transistors”, Microelectronic Engineering, vol. 95, pp. 1-4, 2012.

[23] G. Giri, S. Park, M. Vosgueritchian, M.M. Shulaker, Z. Bao, “High-Mobility, Aligned Crystalline Domains of TIPS-Pentacene with Metastable Polymorphs Through Lateral Confinement of Crystal Growth” Advanced Materials, vol. 26(3), pp. 487-493, 2014.

[24] Z. He, J. Chen, J.K. Keum, G. Szulczewski, D. Li, “Improving performance of TIPS pentacene-based organic thin film transistors with small-molecule additives” Organic Electronics, vol. 15(1), pp. 150-155, 2014.

[25] S.M. Ryno, C. Risko, J.L. Brédas, “Impact of molecular packing on electronic polarization in organic crystals: the case of pentacene vs tips-pentacene”, Journal of the American Chemical Society, vol. 136(17), pp. 6421-6427, 2014.

[26] J.A. Rogers, A. Dodabalapur, Z. Bao, H.E. Katz, “Low-Voltage 0.1 mm Organic Transistors and Complementary Inverter Circuits Fabricated with a Low-Cost form of Near-Field Photolithography”, Applied Physics Letters, vol. 75(7), pp. 1010 – 1012, 1999

[27] V. Fakhfouri, G. Mermoud, J.Y. Kim, A Martinoli, J. Brugger, “Drop-on-demand inkjet printing of SU-8 polymer. Micro and Nanosystems”, vol. 1(1), pp. 63-67, 2009.

[28] D.K. Owens, R. Wendt, “Estimation of the surface free energy of polymers”, Journal of applied polymer science, vol. 13, pp. 1741-1747, 1969.

[29] S.H. Lee, M.H. Choi, S.H. Han, D.J. Choo, J. Jang, S.K. Kwon, “High-performance thin-film transistor with 6, 13-bis (triisopropylsilylethynyl) pentacene by inkjet printing”, Organic Electronics, vol. 9(5), 721-726, 2008.

[30] Y. Kuo, “Thin Film Transistor Technologies: Proceedings of the Fourth Symposium on Thin Film Transistor Technologies”, The Electrochemical Society, Technology & Engineering, 1999.

[31] H.J. Pyo, P.A. Young, L. Seonghoon, K. Jihoon S. Nayool, Y.Y. Do, “Tuning of Ag work functions by self-assembled monolayers of aromatic thiols for an efficient hole injection for solution processed triisopropylsilylethynyl pentacene organic thin film transistors”, Applied Physics Letters, vol. 92, pp. 143311, 2008.

[32] C.D Dimitrakopoulos, D.J. Mascaro, “Organic thin-film transistors: A review of recent advances”, IBM Journal of Research and Development, vol. 45(1), 11-27, 2001.

[33] D.J. Gundlach, T.N Jackson, D.G. Schlom, S.F. Nelson, “Solvent-induced phase transition in thermally evaporated pentacene films”, Applied Physics Letters, vol. 74 (22), pp. 3302-3304, 1999.

[34] J.H. Schön, B. Batlogg, “Modeling of the temperature dependence of the field-effect mobility in thin film devices of conjugated oligomers”, Applied physics letters, vol. 74(2), pp. 260-262, 1999.

[35] D.H. Dunlap, P.E. Parris, V.M. Kenkre, “Charge-dipole model for the universal field dependence of mobilities in molecularly doped polymers”, Physical review letters, vol. 77(3), pp. 542, 1996.

[36] S.V. Novikov, D.H. Dunlap, V.M. Kenkre, P.E. Parris, A.V. Vannikov, “Essential role of correlations in governing charge transport in disordered organic materials”, Physical Review Letters, vol. 81(20), pp. 4472, 1998.

CHAPTER IV

A SCREEN PRINTED FLEXIBLE ELECTROCHEMICAL SENSOR FOR SELECTIVE DETECTION OF TOXIC HEAVY METALS

4.1. Introduction

In recent years, much attention has been given towards the development of cost effective sensors for the heavy metal detection in agricultural, environmental and medical industries [1-3]. Heavy metals, such as mercury (Hg), lead (Pb), cadmium (Cd), chromium (Cr) and arsenic (As), are highly toxic and carcinogenic, even at trace levels [4]. Among heavy metal contaminants, Pb and Hg are considered as the more toxic chemicals and therefore are of a global health concern [5]. These heavy metals are non-biodegradable and accumulate in the food chain, which causes severe threats to human health by affecting the metabolic processes resulting in neuromuscular, neurological, nephritic physiological disorders [6]. Exposure to these heavy metals causes acute chronic poisoning, which affects several organs in the body, including kidneys, liver, brain and heart [7-9]. Hg ions (Hg^{2+}) and Pb ions (Pb^{2+}) are widely distributed in water, air and soil in organic, inorganic and metallic forms [10]. Thus, rapid and highly sensitive monitoring of heavy metals such as Pb and Hg in the environment and food is very crucial.

Several detection techniques such as inductively coupled plasma mass spectrometry (ICP-MS) [11], X-ray fluorescence (XRF) spectroscopy [12], and cold vapor atomic absorption spectrometry (CV-AAS) [13] have been reported for the detection of heavy metals. However, these methods are typically time consuming, relatively expensive, laborious, require tedious sample preparation and require a degree of expertise and experience to handle safely. Advancements in research have

demonstrated the usage of cyclic voltammetry (CV), which is a rapid, simple and inexpensive process for the detection of bio/chemicals [14-15]. In CV, the surface of the electrode is usually pretreated or coated with a sensing layer for increasing the selectivity and/or sensitivity of the electrochemical sensors. 1,10-Phenanthroline-based compounds are well known for their effectiveness in binding with metal ions to form inorganic complexes [16-26]. However, the use of their derivatives in the detection of metal ions and other molecular substrates, have not been well explored [27-29]. Moreover, CV is traditionally performed with conventional electrodes as shown in fig. 2.16 of section 2.5 in chapter 2 or on an electrochemical sensor that is fabricated by means of silicon technologies. Advancements in the fabrication techniques lead to direct printing of electrodes on flexible substrates using functional inks.

In this work, a printed electrochemical sensor was used for selective detection of Pb^{2+} and Hg^{2+} ions. The conventional screen printing technique was used to print the sensor on a flexible polyethylene terephthalate (PET) substrate. The sensor consisted of carbon working electrode (WE), silver (Ag) counter electrode (CE) and silver/silver chloride (Ag/AgCl) reference electrode (RE). 1,10-phenanthroline and its derivative naphtho[2,3-a]dipyrido[3,2-h:2',3'-f]phenazine-5,18-dione (QDPPZ) was used as a sensing layers for the detection of Pb^{2+} and Hg^{2+}. The CV response of the sensor was studied, to demonstrate the selectivity towards Pb^{2+} and Hg^{2+}, and the results are reported.

4.2. Materials, Chemicals and Sample Preparation

A flexible PET of 130 μm thickness (Melinex ST 505) from DuPont Teijin Films was used as a substrate. Henkel Electrodag 479SS, a silver flake ink, was used for metalizing the counter electrode. The material used for the working electrode was

a carbon conductive ink from DuPont® 7105. A DuPont® 5874 ink, consisting of Ag/AgCl with a ratio of 65/35, was used for reference electrode. $Pb(NO_3)_2$, $Hg(NO_3)_2$ (in powder form), 1,10-phenanthroline, potassium bromide, 9,10-diaminoanthroquinone, tetrabutylammonium hexafluorophosphate, ethanol, sulfuric acid and nitric acid were purchased from Sigma Aldrich Chemical Company. All chemicals were used without further purification. Different concentrations of $Pb(NO_3)_2$, and $Hg(NO_3)_2$ (1 nM, 1 µM, 50 µm, 250 µm, 500 µm, 750 µm and 1 mM) were prepared by dissolving in deionized (DI) water and stored in 10 mL aliquots at 2 °C. A spring loaded small outline integrated circuit (SOIC) test clips (14 pin) was acquired from Pomona® Electronics.

4.3. Design and Screen Printing of Electrochemical Sensor

Advancements in fabrication techniques have led to the research of the screen printing for the direct printing of electrochemical sensors [30-34]. Screen printed electrodes (SPE) are usually printed in planar form on a single substrate. SPE's demonstrated the ability to replace the conventional bulky electrodes used in the traditional CV setup. Moreover, much lower volumes of analyte are required with SPEs for assessing the electrochemical response [35]. Studies on the optimization SPEs has revealed that the key parameters of the SPE geometry, such as electrode area, electrode shape and electrode placement, play a major role with respect to sensor performance [36-37]. Research by Garcia *et.al* showed the effect of electrode area on the sensor signal to noise ratio. It was shown that the electrode area near to 10^8 μm^2 has a higher signal to noise ration compared to 10^6 μm^2 and 10^4 μm^2 [36]. Studies by Lambrechts *et.al*, demonstrated that the circular electrode generates lower noise compared to the rectangular electrode. From the same study, it was also recommended that the area of counter electrode has to be at least 1.4 times larger than the working

electrode area as it improves current density at the counter electrode [37]. Taking these factors into consideration and with an aim of miniaturizing the electrochemical sensor, an overall device dimensions of 2 cm × 1 cm, with a circular working electrode radius of 1700 µm, a counter electrode outer and inner radius of 3900 µm and 2900 µm, respectively and a reference electrode width of 1000 µm was chosen by the author for designing the electrochemical sensor. Figure 4.1 (a) shows the schematic of the electrochemical sensor. The sensor artwork was designed in Adobe Illustrator. A screen containing the sensor designs were fabricated at Microscreen®, Indiana with a stainless steel mesh count of 325 and MS-22 emulsion with a thickness of 12.7 µm. The screen had a wire diameter of 28 µm and an angle of 22.5°.

An MSP 485 precision screen printer from Hary Manufacturing Inc. (HMI) was used to print the electrochemical sensor. The PET was cleaned with isopropyl alcohol before printing the electrodes. Initially, a working electrode was printed using DuPont® 7105 and cured at 120°C for 5 min in a conventional oven. Then Electrodag 479SS was printed and cured at 90 °C for 20 minutes to form a counter electrode. Finally, a reference electrode was printed using a DuPont® 5874 ink and cured at 120 °C for 3 min. A photograph of the screen printed sensor is shown in Fig. 4.1 (b).

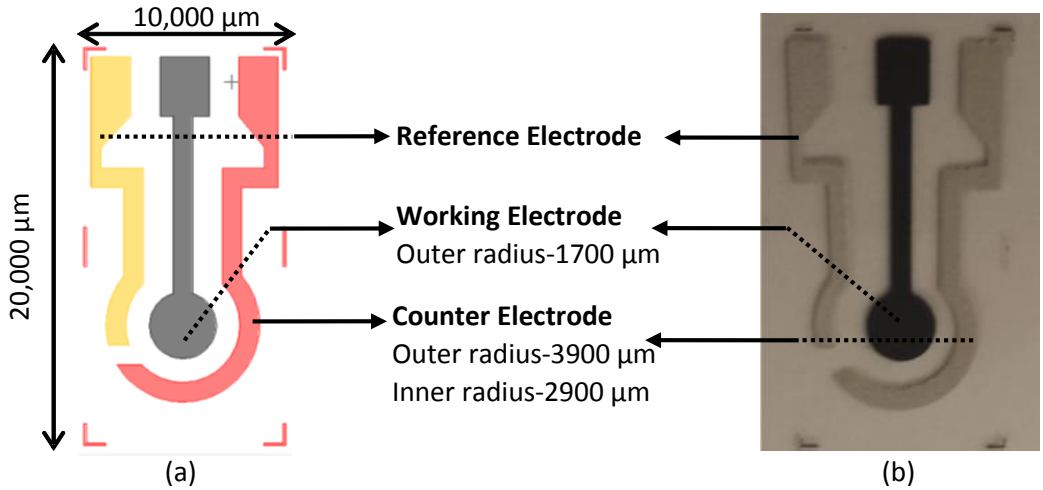

Figure 4.1. (a) Schematic and (b) photograph of the printed electrochemical sensor

Figure 4.2 shows the vertical scanning interferometry 3D topography of the printed electrodes, which was measured using a Bruker Contour GT-K profilometer (Bruker Biosciences Corporation, USA), with Bruker Vision software operating in hybrid mode. The average thickness of the printed electrodes were measured as 6.7±1.4 µm (Fig. 2(a)), 5.1±0.1 µm (Fig. 2(b)) and 17.1±1.3 µm (Fig. 2(c)); and root mean square (RMS) roughness of the printed layers were measured as 0.84 ±0.1 µm (Fig. 2(d)), as 0.73 ±0.1 µm (Fig. 2(e)) and as 1.0±0.1 µm (Fig. 2(f)) for the counter, working and reference electrodes, respectively.

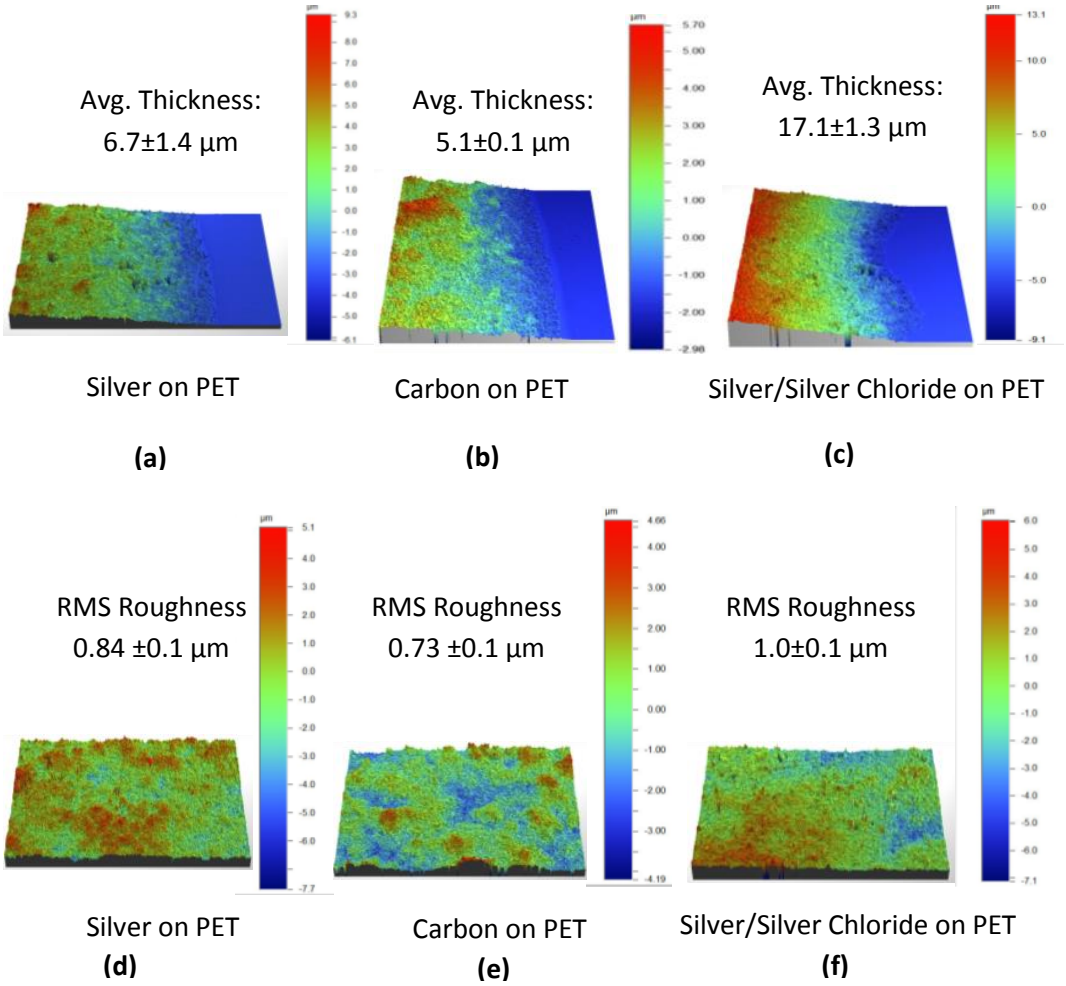

Figure 4.2. Vertical scanning interferometry 3D topography of printed electrodes on PET showing the average thickness of (a) silver, (b) carbon, (c) silver/silver chloride and RMS roughness of (d) silver, (e) carbon, and (f) silver/silver chloride.

4.4. Synthesis of Sensing Layers

After printing the electrodes, sensing layers were added to increase the selectivity and sensitivity of the sensor. 1,10-Phenanthroline and its derivative naphtho[2,3-a]dipyrido[3,2-h:2',3'-f]phenazine-5,18-dione (QDPPZ) were added as sensing layers for the detection of heavy metal ions. The synthesis of these compounds has been previously reported [38-41]. A brief description of the synthesis is presented in the following section.

QDPPZ was synthesized in a two step process. First, 1,10-phenanthroline was oxidized to 1,10-phenanthroline-5,6-dione, then the dione was coupled with 1,2-diaminoanthraquinone in a condensation reaction.

Synthesis of 1,10-phenanthroline-5,6-dione

20 mL of concentrated sulfuric acid (H_2SO_4) and 10 mL of concentrated nitric acid (HNO_3) were added drop wise to a mixture of 1,10-phenanthroline (1.00 g, 5.56 mmol) and potassium bromide (5.95 g, 50 mmol) at 0°C. The mixture was refluxed at 80°C for 2 hours, then cooled to room temperature. The contents of the reaction flask were then diluted with 400 mL deionized water, and neutralized with sodium bicarbonate ($NaHCO_3$). The product was extracted with methylene chloride, and dried over anhydrous $MgSO_4$. All solvents were removed using a rotary evaporator. The product was concentrated in vacuum, resulting in a yellow solid. The product was purified using recrystallization from methanol. The average yield was 95% (1.11 g, 5.31 mmol). ^{1}H NMR ($CDCl_3$, 400 MHz) δ: 9.12-9.10 (t, 2H, J = 2.85 Hz), 8.51-8.48 (d, 2H, J = 1.83 Hz), 7.60-7.55 (m, 2H, J = 4.71 Hz).

Synthesis of QDPPZ

Figure 4.3 shows the synthesis of QDPPZ. 1,10-phenanthroline-5,6-dione (0.50 g, 2.38 mmol) was refluxed in ethanol for 15 min. 1,2-diaminoanthraquinone

(0.57 g, 2.38 mmol) was added to the reaction flask and the mixture was refluxed for 4 hrs. The solution changed color from yellow to dark purple. The solution was allowed to cool to room temperature and then filtered to collect the solid product. The product was washed with methanol and concentrated in vacuum. The product was further dried in a vacuum over at 60°C for 12 hrs. The reaction yield was 80%.

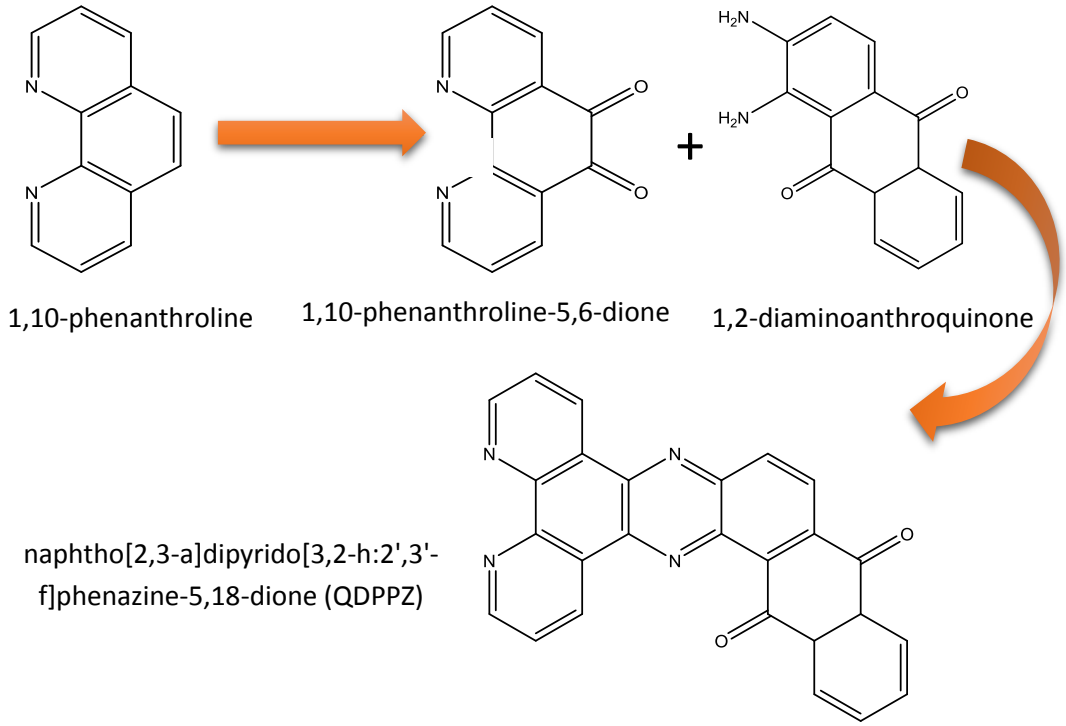

Figure 4.3. Synthesis of naphtho[2,3-a]dipyrido[3,2-h:2',3'-f]phenazine-5,18-dione (QDPPZ).

4.5. Sensor Preparation and Experiment Setup

First, the sensor surface was prepared for the selective detection of the Pb^{2+} and Hg^{2+}. Solutions were then prepared with the synthesized chemicals by dissolving 41.4 mg of tetrabutylammonium hexafluorophosphate in 20 mL of ethanol to form a 7 mM solution. This solution was used as the electrolyte solution through out the remaining experiments. A 1 mM QDPPZ solution was formed by dissolving 4.1 mg synthesized QDPPZ in 10 mL electrolyte solution. Similarly, a 1 mM of 1,10-phenanthroline solution was prepared by dissolving 1.8 mg in electrolyte solution.

40 µL of 1,10-phenanthroline and QDPPZ solutions were then individually drop casted onto the working carbon electrodes at 100 °C to form the sensing layers for Hg^{2+} and Pb^{2+} detection, respectively.

The electrochemical sensors coated with the sensing layers were connected to the PARSTAT 2273 potentiostat (Princeton Applied Research) using a SOIC test clip. Next, the wires and probes were calibrated before taking measurements. CV studies were recorded on the printed device using a potentiostat, which was connected to a PC via USB for controlling and post processing of the data. The experimental setup is shown in Fig. 4.4. All measurements were conducted at room temperature.

Figure 4.4. Experiment setup.

4.6. Results and Discussion

The response of the heavy metal ions was first tested on the 1,10-phenanthroline drop casted sensor. The CV based response of the sensors was recorded from -0.5 V to 0.5 V at 50 mV/s for Pb^{2+} and Hg^{2+}. Initially, a reference signal was established by loading the 50 µL of DI water on to the sensor using a pipette. Then, test sample solutions with 50 µM concentrations of Hg^{2+} and Pb^{2+} were introduced onto the sensor. The response of the printed electrochemical sensor towards Pb^{2+} and Hg^{2+} is shown in Fig. 4.5. It was observed that the 1,10-phenanthroline drop casted sensor was sensitive to only Hg^{2+}. The reduction peak potential at 0.2 eV was registered for Hg^{2+} which is comparable to the reported

literature values [42-43]. This behavior of the sensor can be explained by considering the molecular structure of the 1,10-phenanthroline. The molecule has two phenazine nitrogen atoms on one end. Two molecules of 1,10-phenanthroline with four nitrogen atoms together form dative covalent bonds with Hg. The schematic illustration is shown in Fig 4.6.

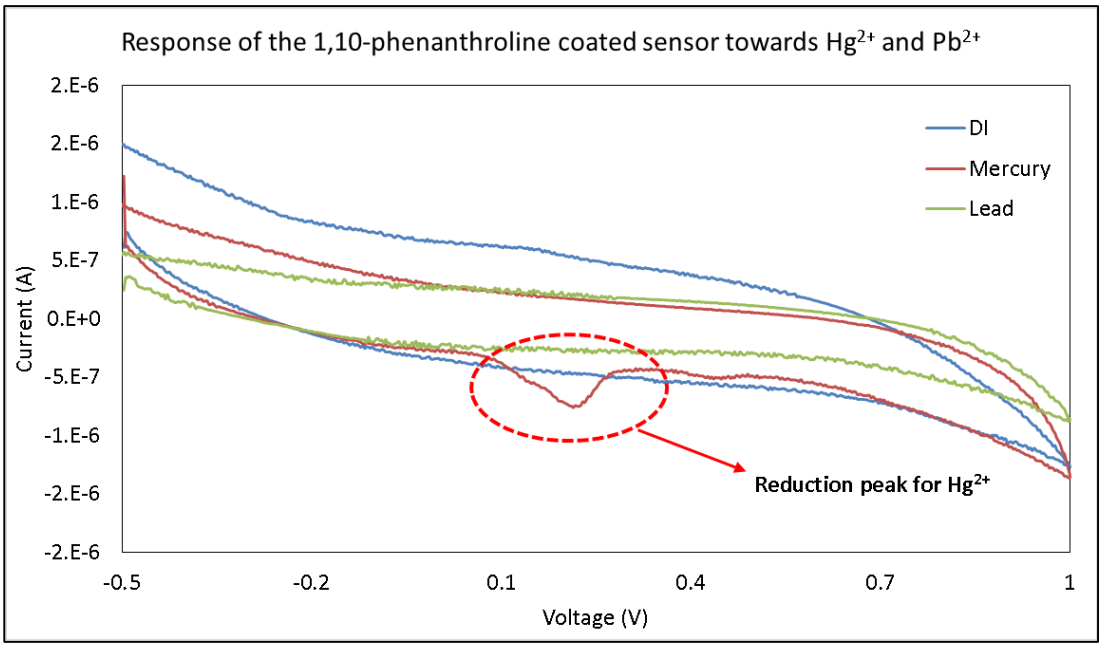

Figure 4.5. Response of the 1,10-phenanthroline coated sensor towards Hg^{2+} and Pb^{2+}.

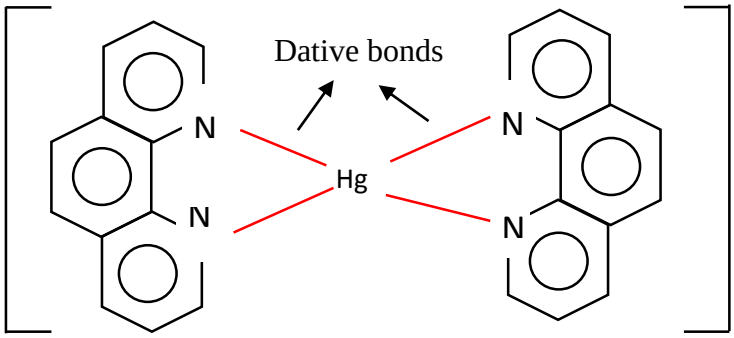

Figure 4.6. Formation of dative bonds between 1,10-phenanthroline and Hg^{2+}.

Figure 4.7 shows the response of the sensors towards varying concentrations of the Hg^{2+}. An average peak current value of -0.43 µA, -0.59 µA, -1.28 µA, -2.38 µA and -3.78 µA, with an average standard deviation of 96 nA, 0.14 µA, 0.25 µA,

0.48 µA and 0.87 µA was observed for the 50 µM, 100 µM, 500 µM, 750 µM and 1 mM concentrations, respectively. This corresponds to an average current percentage change ($(I_{Concentration} - I_{DI})/I_{DI}$) of 9 %, 49 %, 225 %, 506 % and 888 % with an average standard deviation of 5 %, 28 %, 47 %, 106 % and 331 % for the 50 µM, 100 µM, 500 µM, 750 µM and 1 mM concentrations, respectively (Fig. 4.8), when compared to the base current of DI. Using the results obtained, it is clear that the CV response of the electrochemical sensor could be used to quantify the different concentrations of Hg^{2+} and also selectively detect Hg^{2+} as there was no crossover in the overall current values, among all five sensors tested.

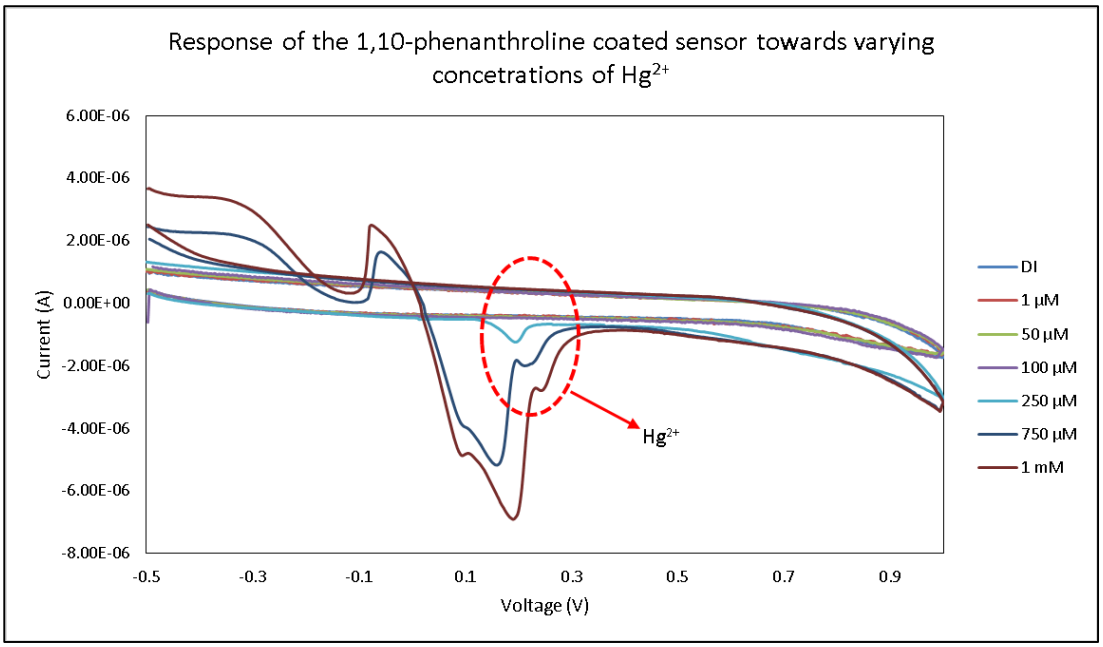

Figure 4.7. Response of the 1,10-phenanthroline drop casted sensor towards increasing concentrations of Hg^{2+}.

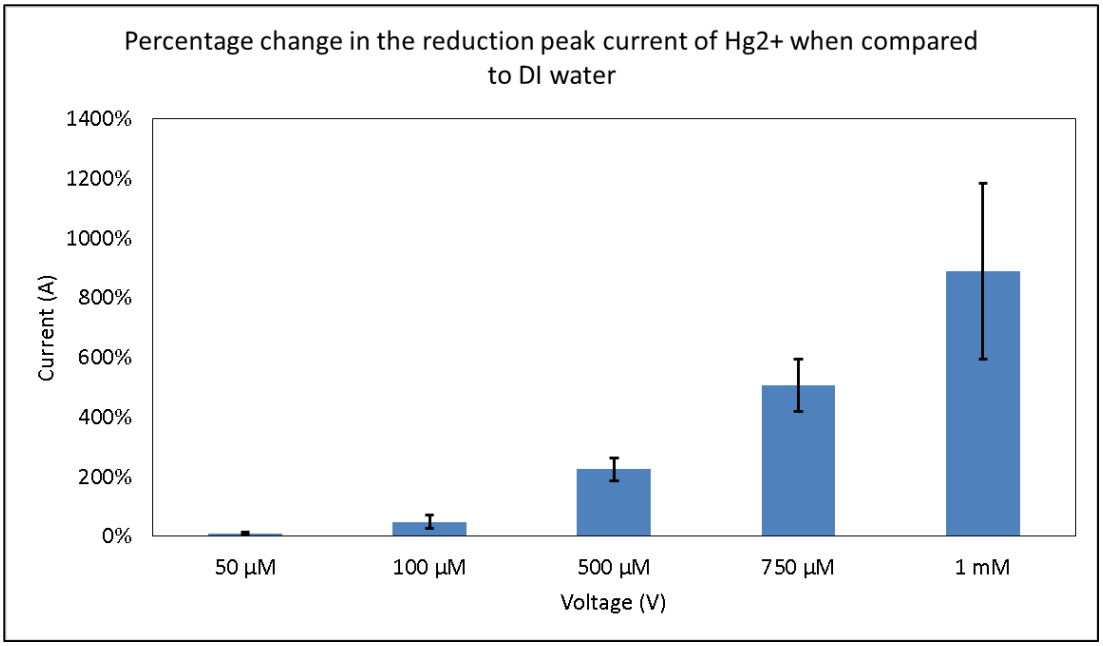

Figure 4.8. Percentage change in the reduction peak current of Hg^{2+} when compared to the DI water in presence of 1,10-phenanthroline.

The sensor, which consisted of QDPPZ deposited on the working electrode, was also tested towards $Pb^{2+}$and Hg^{2+}. Figure 4.9 shows the CV based response of the electrochemical sensor recorded from -1 V to 0 V at 50 mV/s for Pb^{2+} and Hg^{2+}. 50 µL of DI water was loaded on to the sensor for recording the reference signal. Then, 50 µL of test sample solutions with 50 µM concentrations of Hg^{2+} and Pb^{2+} was introduced onto the sensor. It was observed that the reduction potential of −0.6 eV obtained for Pb^{2+} with the printed sensor was comparable to reported literature values [44]. These results indicate that the sensor responds to only towards Pb^{2+}. This behavior could be explained by examining the structure of QDPPZ, the molecule consists of a 1,10-phanthroline unit on one end and a quinolone unit on the opposite end. While 1,10-phenanthroline alone does not exhibit selectivity toward Pb^{2+}, its derivative QDPPZ showed excellent selectivity toward Pb^{2+}. The selectivity is thought to result from the quinoline oxygen and the phenazine nitrogen forming a pocket that has a cavity of the right size to hold Pb^{2+} ions. This results in a complex

formation that generates the signal. Interestingly, this complex formation does not occur in the presence of Hg^{2+} ions.

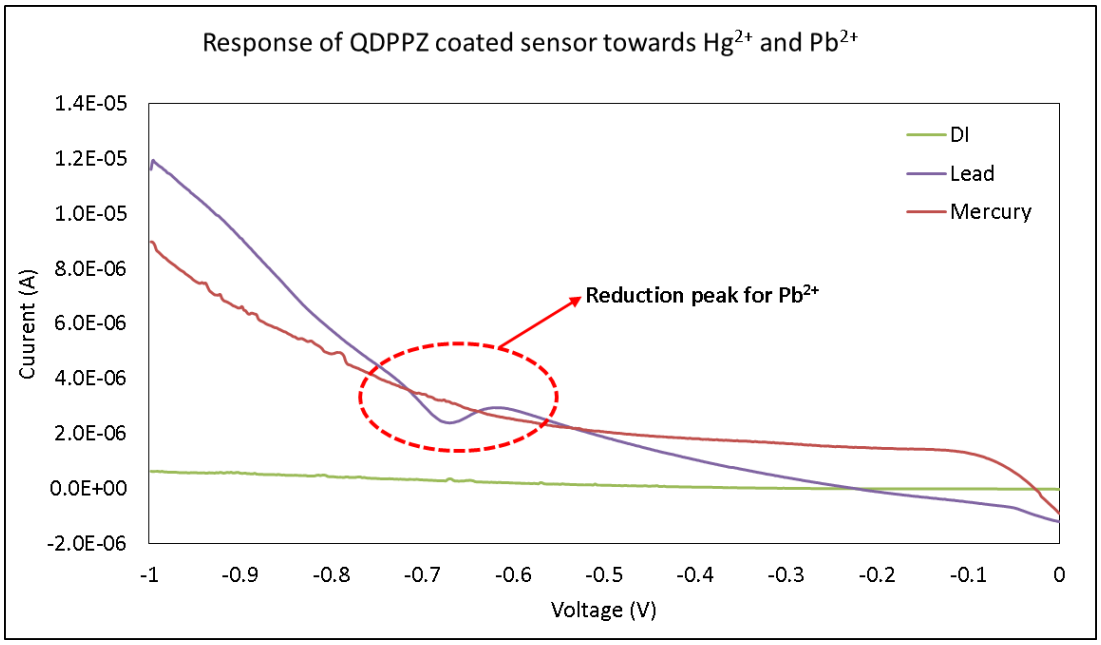

Figure 4.9. Response of the QDPPZ coated sensor towards Hg^{2+} and Pb^{2+}.

Figure 4.10 shows the response of the QDPPZ drop casted sensor towards varying concentrations of the Pb^{2+} ions. It was observed that the average peak current in the sensor increased from -0.41 µA to -2.6 µA to -7.2 µA to -15.9 µA and to -24.4 µA as the concentration of the Pb^{2+} increased from 50 µM to 250 µM to 500 µM to 750 µM and to 1 mM, respectively. The relative standard deviations at 50 µM, 250 µM, 500 µM, 750 µM and 1 mM is 0.3 µA, 1.2 µA, 2.3 µA, 4.5 µA and 3.2 µA, respectively (shown in Fig. 4.11). These results indicate that the electrochemical sensor was able to distinguish between the varying concentrations of Pb^{2+}. Detection levels of 50 µM were possible for the Pb^{2+} solution, which is well below the United States Food and Drug Administration (USFDA) limits of 5 mM for Pb^{2+} [45].

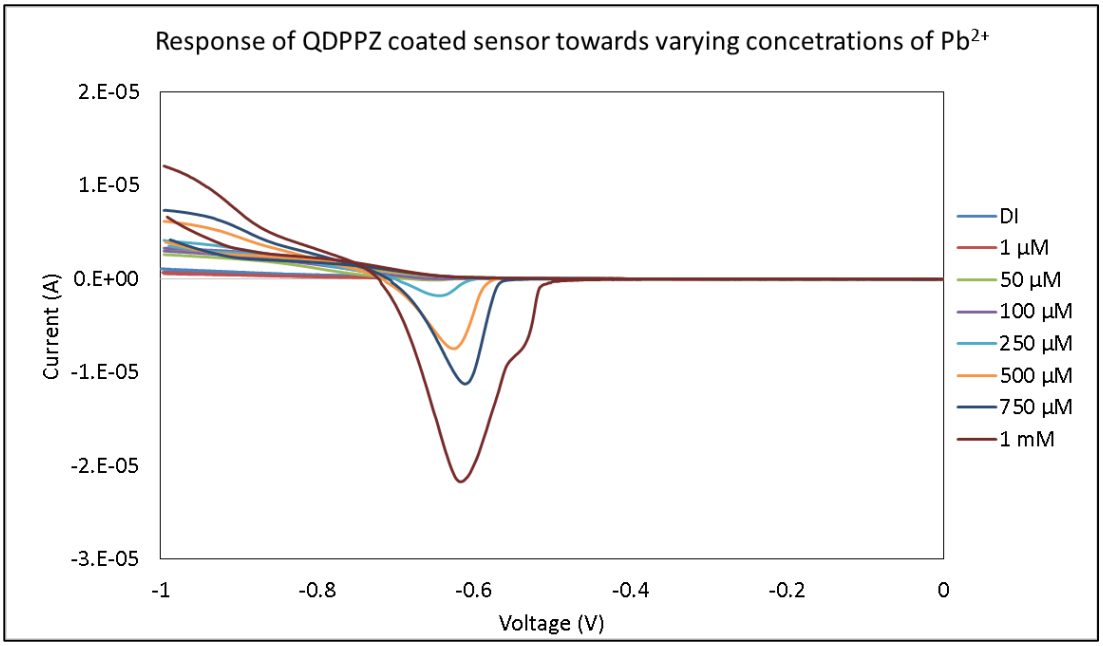

Figure 4.10. Response of the QDPPZ drop casted sensor towards increasing concentrations of Pb^{2+}.

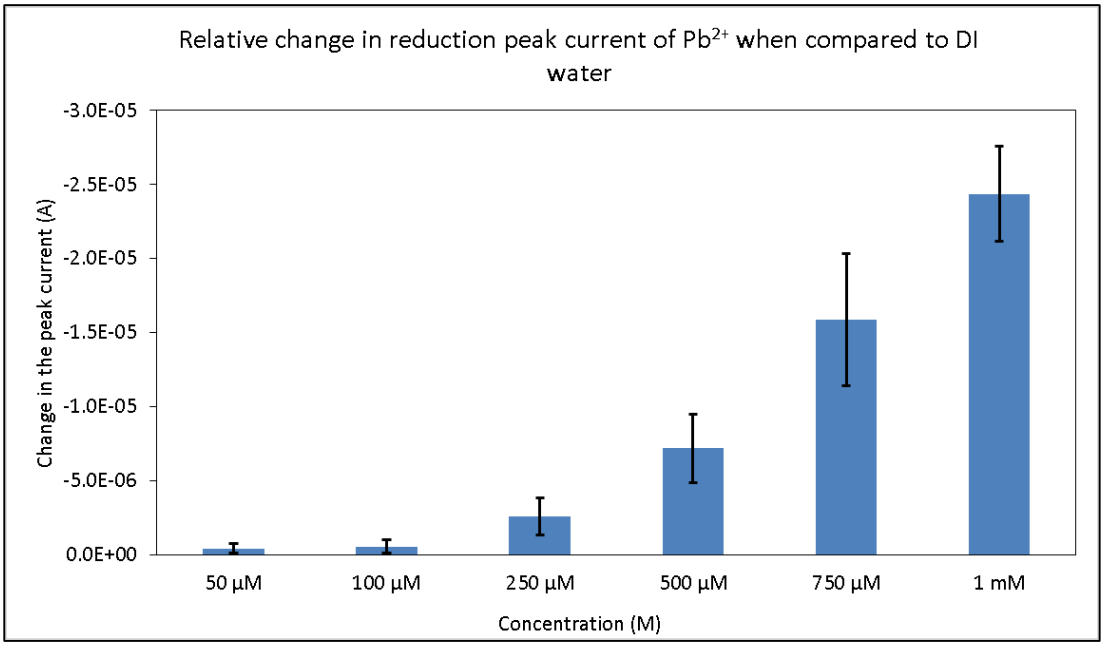

Figure 4.11. Percentage change in the reduction peak current of Pb^{2+} when compared to the DI water in presence of QDPPZ.

4.7. Summary

In this chapter, the author briefly discussed the importance of heavy metal detection. A detailed account of the experimental tasks involved in this work was then presented. This includes the materials, chemicals used and synthesis of the sensing

layer for selective detection of heavy metals. Finally, the electrochemical response of the printed sensor towards heavy metals was presented.

To summarize, a printed electrochemical sensor was successfully fabricated on a flexible PET substrate using a traditional screen printing process. Carbon, Ag and Ag/AgCl inks were used for metallizing the sensor, which had a working electrode dimension of 1,700 µm radius, counter electrode dimensions of 3900 µm and 2900 µm outer and inner radius and reference electrode of 1000 µm wide. 10-phenanthroline was used as sensing layer for Hg^{2+}. QDPPZ was synthesized from 1,10-phenanthroline and used as sensing layer for Pb^{2+}. The CV based response of the sensor towards Hg^{2+} and Pb^{2+} was investigated. Reduction peaks at 0.23 eV and -0.6 eV were observed, demonstrating the selective detection of Hg^{2+} and Pb^{2+}, respectively. The sensor also provided concentration specific signals toward Pb^{2+} and Hg^{2+}, which is necessary for devices that can determine the amount of possible exposure levels.

In the following chapter, the author presents a project that involved the development of a wireless LC sensor fabricated by the screen printing process. The author discusses the design, fabrication and characterization of a flexible wireless sensor. The experiment setup, testing and results obtained are discussed and presented.

References

[1] Y. Shan, M. Tysklind, F. Hao, W. Ouyang, S. Chen, C. Lin, "Identification of sources of heavy metals in agricultural soils using multivariate analysis and GIS", Journal of Soils and Sediments, vol.13 pp.720-729, 2013.

[2] A.I. Zia, M.A. Rahman, S.C. Mukhopadhyay, P.L. Yu, I.H. Al-Bahadly, P.C. Gooneratne, J. Kosel, T.S. Liao, "Technique for rapid detection of phthalates in water and beverages", Journal of Food Engineering, vol. 116, pp. 515-523, 2013.

[3] S. Zhuiykov, K. Kalantar-zadeh, "Development of antifouling of electrochemical solid-state dissolved oxygen sensors based on nanostructured $Cu_{0.4}Ru_{3.4}O_7$ + RuO_2 sensing electrodes", Electrochimica Acta, vol. 73, pp.105-111, 2012.

[4] M. Li, H. Gou, I.A. Ogaidi, N. Wu, "Nanostructured sensors for detection of heavy metals: A Review", ACS Sustainable Chemical Engineering, vol. 1 pp. 713−723, 2013.

[5] P. Wongsasuluk, S. Chotpantarat, W. Siriwong, M. Robson, "Heavy metal contamination and human health risk assessment in drinking water from shallow groundwater wells in an agricultural area in Ubon Ratchathani province", Thailand Environmental Geochemistry and Health, vol. 1, pp. 169-182, 2014.

[6] B. Ibarlucea, C.D. Gil, J.R.I, Veciana, A. Caballero, F. Zapata, A. Tárraga, P.S. Molina, S. Demming, S. Büttgenbach, C.S. Fernández, A. Llobera, "PDMS based photonic lab-on-a-chip for the selective optical detection of heavy metal ions", Analyst, vol. 138, pp.839-844, 2013.

[7] H. Zheng, J. Ma, Z. Zhu, Z. Tang, S. Hu, Dielectric barrier discharge micro-plasma emission source for the determination of lead in water samples b tungsten coil electro-thermal vaporization, Talanta. 132 (2015) 106-111.

[8] T.W. Clarkson, L. Magos, G.J. Myers, "The toxicology of mercury–current exposures and clinical manifestations" The New England Journal of Medicine, vol. 349, pp. 1731–1737, 2003.

[9] Y. Wang, F. Yang, X. Yang "Colorimetric biosensing of mercury(II) ion using unmodified gold nanoparticle probes and thrombin-binding aptamer", Biosensors and Bioelectronics, vol. 25, pp. 1994–199, 2010.

[10] F.A. Cotton, G. Wilkinson, C.A. Murillo, M. Bochmann, "Advanced Inorganic Chemistry", (6th ed.) John Wiley & Sons, New York, 1999

[11] E. M. Krupp, B. F. Milne, A. Mestrot, A. A. Meharg, J. Feldmann, "Investigation into mercury bound to biothiols: structural identification using ESI-ion-trap MS and introduction of a method for their HPLC separation with simultaneous detection by ICP-MS and ESI-MS", Analytical and Bioanalytical Chemistry, vol. 390, pp.1753-1764, 2008.

[12] S. Arzhantsev, X. Li, J.F. Kauffman, "Rapid limit tests for metal impurities in pharmaceutical materials by X-ray fluorescence spectroscopy using wavelet transform filtering", Analytical Chemistry vol. 83, pp. 1061-1068, 2011.

[13] F.A. Duarte, C.A. Bizzi, F.G. Antes, V.L. Dressler, E.M. de Moraes-Flores, "Organic, inorganic and total mercury determination in fish by chemical vapor generation with collection on a gold gauze and electrothermal atomic absorption spectrometry", Spectrochimica Acta Part B: Atomic Spectroscopy, vol. 64 pp. 513-519, 2009.

[14] Y.A. Gao, N. Li, L. Zheng, X. Zhao, S. Zhang, B. Han, G. Li, "A cyclic voltammetric technique for the detection of micro-regions of bmimPF_6/Tween 20/H_2O microemulsions and their performance characterization by UV-Vis spectroscopy", Green Chemistry, vol. 8(1), pp. 43-49, 2006.

[15] K. Tybrandt, S.B. Kollipara, M. Berggren, "Organic electrochemical transistors for signal amplification in fast scan cyclic voltammetry", Sensors and Actuators B: Chemical, vol. 195, pp. 651-656, 2014.

[16] B. Abraham, C.V. Sastri, B.G. Maiya, S. Umapathy, "Resonance Raman spectroscopic studies of $[Ru(phen)_2qdppz]^{2+}$ and its interactions with calf thymus DNA", Journal of Raman Spectroscopy, vol. 35 pp. 13-18, 2004.

[17] A. Ambroise, B.G. Maiya, "Ruthenium(II) complexes of redox-related, modified dipyridophenazine ligands: Synthesis, characterization, and DNA interaction", Inorganic Chemistry, vol. 39 pp. 4256-4263, 2000.

[18] S. Arounaguiri, B.G. Maiya, "Electro-photo switch and molecular light switch devices based on ruthenium(II) complexes of modified dipyridophenazine ligands: Modulation of the photochemical function through ligand design", Inorganic Chemistry, vol. 38, pp. 842-843, 1999.

[19] D.T. Breslin, J.E. Coury, J.R. Anderson, L. McFail-Isom, Y. Kan, L.D. Williams, L.A. Bottomley, G.B. Schuster, "Anthraquinone photonuclease structure determines its mode of binding to DNA and the cleavage chemistry observed" Journal of American Chemical Society, vol. 119, pp. 5043-5044, 1997.

[20] N. Dupont, Y. Ran, H. Jia, J. Grilj, J. Ding, S. Liu, S. Decurtins, A. Hauser, "A. Effect of the addition of a fused donor-acceptor ligand on a Ru(II) complex:

Synthesis, characterization, and photoinduced electron transfer reactions of $[Ru(TTF\text{-}dppz)_2(Aqphen)]^{2+}$", Inorganic Chemistry, vol. 50 pp. 3295-3303, 2011.

[21] R.B. López, B.L. Loeb, T. Boussie, T.J. Meyer, "Synthesis of a new phenanthroline derived ligand with acceptor properties", Tetrahedron Letters vol. 37 pp. 5437-5440, 1996.

[22] E. Norambuena, C. Olea-Azar, A. Delgadillo, M. Barrera, B. Loeb, "Comparative evaluation of the acceptor properties of quinone derivatized polypyridinic ligands", Chemical Physics, vol. 359, pp. 92-100, 2009.

[23] E.M. Regan, A.J. Hallett, L.C.C. Wong, I.Q. Saeed, E.E. Langdon-Jones, N.J. Buurma, S.J.A. Pope, P. Estrela, "A novel cobalt complex for enhancing amperometric and impedimetric DNA detection", Electrochimica Acta, vol. 128, pp. 10-15, 2014.

[24] C.V Sastri, D. Eswaramoorthy, L. Giribabu, B.G. Maiya, "DNA interactions of new mixed-ligand complexes of cobalt(III) and nickel(II) that incorporate modified phenanthroline ligands", Journal of Inorganic Biochemistry, vol. 94, pp. 138-145, 2003.

[25] R.A. Smith, E.C. Stokes, E.E. Langdon-Jones, J.A. Platts, B.M. Kariuki, A.J. Hallett, S.J.A. Pope, "Cyclometalated cinchophen ligands on iridium(iii): Towards water-soluble complexes with visible luminescence", Dalton Transactions, vol.42, pp. 10347-10357, 2013.

[26] U.P. Maheswari, M. Palaniandavar, "DNA binding and cleavage properties of certain tetrammine ruthenium(II) complexes of modified 1,10-phenanthrolines - Effect of hydrogen-bonding on DNA-binding affinity" , Journal of Inorganic Biochemistry, vol. 98, pp. 219-230, 2004.

[27] W. Guo, B.J. Engelmann, T.J. Haywood, N.G. Blok, D.S. Beaudion, S.O. Obare, "Dual Fluorescence and Electrochemical Detection of the Organophosphorus Pesticides - Ethion, Malathion and Fenthion", Talanta vol. 87, pp. 276-283, 2011.

[28] D.S. Beaudoin, S.O. Obare, "Dual optical and electrochemical glucose detection based on a dipyridophenazine ligand", Tetrahedron Letters, vol. 49, pp. 6054-6057, 2008.

[29] S.O. Obare, C.J. Murphy, "A Two-Color Fluorescent Lithium Ion Sensor", Inorganic Chemisty, vol. 40, pp. 6080-6082, 2001.

[30] F. Arduini, C. Zanardi, S. Cinti, F. Terzi, D. Moscone, G. Palleschi, R. Seeber, "Effective electrochemical sensor based on screen-printed electrodes modified with a carbon black-Au nanoparticles composite, Sensors and Actuators B: Chemical, vol. 212, pp. 536-543, 2015.

[31] P.T. Lee, D. Lowinsohn, R.G. Compton, "The Use of Screen-Printed Electrodes in a Proof of Concept Electrochemical Estimation of Homocysteine and Glutathione in the Presence of Cysteine Using Catechol, Sensors, vol. 14(6), pp. 10395-10411, 2014.

[32] A.R. Fakhari, A. Sahragard, H. Ahmar, "Development of an Electrochemical Sensor Based on Reduced Graphene Oxide Modified Screen-Printed Carbon Electrode for the Determination of Buprenorphine", Electroanalysis, vol. 26(11), pp. 2474-2483, 2014.

[33] A. Erdem, G. Congur, "Dendrimer modified 8-channel screen-printed electrochemical array system for impedimetric detection of activated protein C", Sensors and Actuators B: Chemical, vol. 196, pp. 168-174, 2014.

[34] C.W. Foster, J.P. Metters, D.K. Kampouris, C.E. Banks, “Ultraflexible Screen-Printed Graphitic Eelectroanalytical Sensing Platforms”, Electroanalysis, vol. 26(2), pp. 262-274, 2014.

[35] J. Wang, P.V.A. Pamidi, C.L. Renschler, C. White, “Metal-dispersed porous carbon films as electrocatalytic sensors”, Journal of Electroanalytical Chemistry, vol. 404 (1), pp. 137-142, 1996.

[36] D.E. Garcia, T.H. Chen, F. Wei, C.M. Ho, “A parametric design study of an electrochemical sensor”, Journal of the Association for Laboratory Automation, vol. 15(3), 179-188, 2010.

[37] M. Lambrechts, W. Sansen, “Biosensors: microelectrochemical devices”, CRC Press, 1992.

[38] M. Li, H. Gou, I.A. Ogaidi, N. Wu, “Nanostructured sensors for detection of heavy metals: A Review”, ACS Sustainable Chemical Engineering vol. 1 pp. 713−723, 2013.

[39] Z. Ramshani, A.S.G. Reddy, B.B. Narakathu, J.T. Wabeke, S.O. Obare, M.Z. Atashbar, “SH-SAW sensor based microfluidic system for the detection of heavy metal compounds in liquid environments:, Sensors and Actuators B: Chemical, (In press) 2014.

[40] A.I. Zia, M.A. Rahman, S.C. Mukhopadhyay, P.L. Yu, I.H. Al-Bahadly, P.C. Gooneratne, J. Kosel, T.S. Liao, “Technique for rapid detection of phthalates in water and beverages”, Journal of Food Engineering, vol. 116, pp. 515-523, 2013.

[41] S. Zhuiykov, K. Kalantar-zadeh, “Development of antifouling of electrochemical solid-state dissolved oxygen sensors based on nanostructured $Cu_{0.4}Ru_{3.4}O_7$ + RuO_2 sensing electrodes”, Electrochimica. Acta. vol. 73, pp. 105-111, 2012.

[42] P. Ugo, L.M. Moretto, G.A. Mazzocchin, “Voltammetric determination of trace mercury in chloride media at glassy carbon electrodes modified with polycationic ionomers”, Analytica chimica acta, vol. 305(1), pp. 74-82, 1995.

[43] A. Manivannan, L. Ramakrishnan, M.S. Seehra, E. Granite, J.E. Butler, D.A. Tryk, A. Fujishima, “Mercury detection at boron doped diamond electrodes using a rotating disk technique”, Journal of Electroanalytical Chemistry, vol. 577(2), pp. 287-293, 2005.

[44] J.M. Jian, Y.Y. Liu, Y.L. Zhang, X.S. Guo, Q. Cai, “Fast and sensitive detection of Pb^{2+} in foods using disposable screen-printed electrode modified by reduced graphene oxide, Sensors, vol. 13(10), pp. 13063-13075, 2013.

[45] S. E. Musson, “Characterization of lead leachability from cathode ray tubes using the Toxicity Characteristic Leaching Procedure”,Environmental Science Technology, vol. 34, pp. 4376-4381, 2000.

CHAPTER V

DETECTION OF TOXIC HEAVY METALS USING PRINTED WIRELESS LC SENSORS

5.1. Introduction

Over the past decade, there has been increasing demand for the development of reliable and cost effective portable sensing systems for the detection of toxic heavy metals in the environmental and food processing industries [1-4]. Heavy metals are major environmental pollutants in land and water. Heavy metal contamination is one of the most severe life threats to the living world as they are toxic and non-biodegradable and therefore remain in the ecosystem and food chain [5]. The toxicity of these heavy metals depends on their concentration. For example, low concentrations of heavy metals such as zinc, iron and copper, are biologically essential; however, they can lead to toxicity at higher concentrations [6]. Heavy metals such as mercury and lead are not biologically essential and have a high potential of causing various diseases in humans and animals at even very low concentrations [6]. Various conventional techniques such as colorimetric analysis [7], electrochemical impedance spectroscopy [8] and titration [9] have been widely used for the detection of heavy metals. Although these techniques are sensitive enough, they require complicated instrumentation along with high manufacturing and operational costs.

Recent advancements in the sensor industry have led to the emergence of wireless sensors [10-11]. Wireless sensors have been used in both active and passive modes [12-13]. Passive sensors have more advantages over active wireless sensors as they use a basic inductive capacitor (LC) circuit as a sensor [12]. On the other hand,

active sensors use batteries, amplifiers, antennas and radio frequency (RF) circuits that make the sensor systems complex and expensive [13]. Most of the LC sensors reported in the literature are fabricated using traditional photolithography techniques, which requires complex fabrication steps, needs high operating temperatures and ultimately is a costly process [14]. The recent trend in the fabrication of electronics using conventional printing techniques has provided a promising solution for the fabrication of low cost wireless passive sensors.

In this work, screen printing was used for the fabricating the LC sensor on flexible substrates. Planar inductor and interdigitated electrode (IDE) capacitor were printed using silver ink as metallization layer. Palladium nanoparticles (Pd Nps) were synthesized and coated on to IDEs as a sensing layer for the detection of heavy metal ions. Change in resonant frequency of the LC sensor with varying concentrations of the heavy metal ions was studied and presented in this chapter.

5.2. Sensor Operation

A typical passive wireless sensor uses LC resonant circuit as a sensing element. Figure 5.1 shows the equivalent circuit of an LC sensor with inductor and capacitor in parallel. Usually, in LC sensor, capacitor is a sensing element whereas inductor is mainly used as a coupling device to read the sensor output by means of mutual inductance coupling [15].

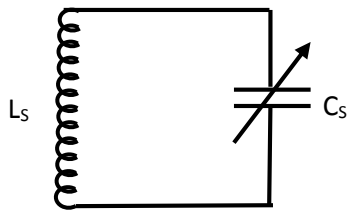

Figure 5.1. Equivalent circuit of LC sensor

The resonant frequency of the LC sensor is given by

$$f = \frac{1}{2\pi\sqrt{L_s C_s}} \tag{16}$$

Where f is the resonant frequency, L_s and C_s are the inductance and capacitance of the LC sensor, respectively. The resonant frequency of the LC sensor is a function of variable sensing capacitor i.e., the resonant frequency changes with respect to change in input stimuli. This change can be wirelessly monitored using a detection coil [16]. The inductive coupling link of the LC sensor with a detection coil is shown in Fig. 5.2.

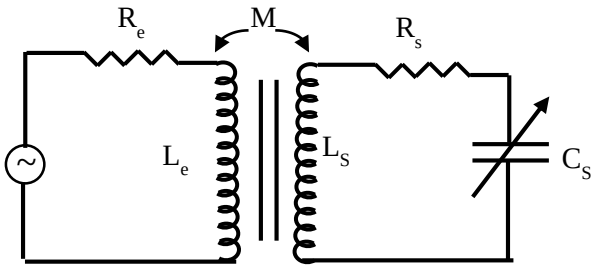

Figure 5.2. Inductive coupling of LC sensor

Impedance of the LC sensor (Z_s) is given by

$$Z_s(\omega) = R_s + j\left(\omega L_s - \frac{1}{\omega C_s}\right) \tag{17}$$

where R_s is the series resistance of the inductor and ω is the angular frequency. The detection coil energizes the LC sensor through inductive coupling resulting in a reflected load impedance. This reflected impedance (X_1) in the detection coil can be expressed as a function of LC sensor impedance (Z_s).

$$X_1 = \frac{(\omega M)^2}{Z_s(\omega)} \tag{18}$$

where M is the mutual inductance between sensor inductor (L_s) and detection coil (L_e). The mutual inductance with coupling coefficient (k) between L_s and L_e is given by

$$M = k\sqrt{L_e L_s} \tag{19}$$

The equivalent circuit at the detection coil with the reflected load impedance is shown in Fig 5.3. Overall reflected detection coil impedance (Z_e) as a function of sensor impedance is given by [17]

$$Z_e = R_e + j\omega L_e + \frac{(\omega M)^2}{Z_s(\omega)} \tag{20}$$

where L_e and R_e are the inductance and the series resistance of the detection coil, respectively.

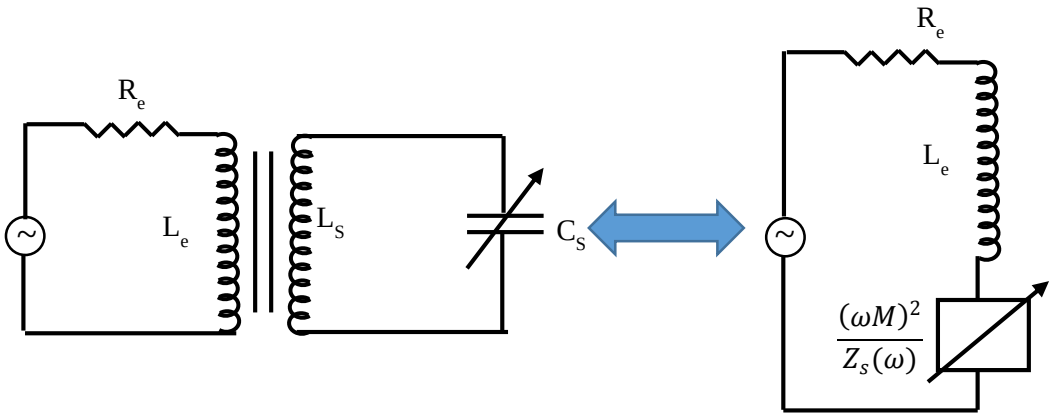

Figure 5.3. Equivalent circuit model of the detection coil with reflected load impedance.

The quality factor of the LC sensor determines the quality of the measurements performed. Quality factor is defined as the ratio of peak energy to the energy dissipated [18]. In LC sensor, it shows the effect of series resistance on the measurements. The quality factor of the LC sensor is given by

$$Q = \frac{1}{R_s}\sqrt{\frac{L_s}{C_s}} \tag{21}$$

In LC sensors, the Q factor also determines the sharpness of the resonant peak [18]. As per the equation 21, it is noticed that the Q factor is inversely proportional to the series resistance. Therefore, it is important to reduce the series resistance of the circular spiral, which can be achieved by reducing the number of turns in the coil and increasing the thickness of the coil. Reducing the number of turns

of a coil will decrease the inductance of the spiral. So, depositing thick metal films with low specific resistivity will be good choice for fabrication of LC sensor. For this reason, the author has chosen the screen printing technique, which is known for depositing thick films, to fabricate the LC sensors.

The response of the LC sensor can be analyzed by measuring S_{11} which is defined as the ratio of applied signal to the reflected signal at Port 1 [19].

$$S_{11} = \frac{V_{reflected}}{V_{applied}} \tag{22}$$

This ratio is the same as the reflection coefficient Γ in transmission theory and can be given as

$$S_{11} = \frac{V_{reflected}}{V_{applied}} = \frac{Z_L - Z_S}{Z_L + Z_S} \tag{23}$$

where Z_L and Z_S are the load and source impedances, respectively. For measuring S_{11}, the detection coil is energized by applying a time-varying excitation signal. According to the Ampere's Law, the applied signal produces a magnetic flux in the detection coil, which is then induced into the sensor coil. As per the Faraday's Law of Induction, a small current will be generated in the sensor coil due to this magnetic flux. This small current in the sensor coil result in a secondary magnetic flux in opposition to the primary magnetic flux in the detection coil. Due to this secondary magnetic flux there would be secondary induced voltage on the detection coil [20]. Therefore S_{11} of the detection coil will be influenced by both detection coil impedance and the LC sensor impedance.

5.3. Design of Planar Inductor and Capacitor

Planar Inductor

Planar spiral inductors are widely used as coupling elements for LC sensors. Various shapes, such as rectangular, hexagonal, octagonal and circular planar

inductors, have been reported [21-23]. Design parameters such as number of turns in coil, outer dimension, inner dimension, pitch of the lines play a major role in determining the value of inductance [24-25]. Choice of the planar inductors depend mainly on available fabrication methods. Rectangular spirals are widely used planar inductors because of their simplicity in shape [26-29]. Circular planar spirals are hard to design, but have been proved to have lower resistive and capacitive loses compared to the rectangular spirals and other designs [30]. Studies have shown that the series resistance of circular spirals are 10% smaller than that of rectangular spirals [31]. It was also reported that the quality factor increases with number of ends in a spiral [32]. Circular spiral ideally has infinite edges. Due to these advantages, the author has chosen circular spirals in this study. The schematic of the circular planar spiral is shown in Fig. 5.4.

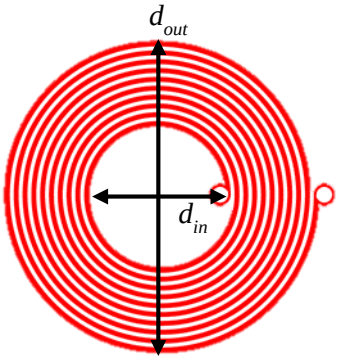

Figure 5.4. Circular spiral coil with inner and outer diameters

The inductance of the planar circular spiral is theoretically computed using [24]

$$L_S = \frac{\mu_0 n^2 d_{avg}}{2}\left(\ln\left(\frac{2.46}{\Delta}\right) + 0.2\Delta^2\right) \tag{24}$$

$$d_{avg} = \frac{d_{out} + d_{in}}{2} \tag{25}$$

$$\Delta = \frac{d_{out} - d_{in}}{d_{out} + d_{in}} \tag{26}$$

where μ_0 is permeability of the vacuum, n is number of turns, d_{out}, d_{in} and d_{avg} are the outer, inner and average diameters of the coil, respectively. Δ is the fill ratio as given in eq. 26. The length of the spiral is given by [33]

$$l = \frac{\pi}{2}[4d_{in}n + n(2n-1)(W+S)] \quad (27)$$

where W and S are the width and length of metal trace, respectively. If *l* is higher than the wavelength (λ) of the signal propagating through the inductor, then the spiral inductor can be considered as a transmission line [34]. λ is given by

$$\lambda = \frac{c}{f} \quad (28)$$

In equation 28, *c* is the speed of the electrons which can be approximated to speed of the light and *f* is the frequency of the signal propagating though the inductor. The dimensions of the planar inductor used in this work have chosen to have *l* smaller than the λ to overcome the transmission line losses.

Planar Capacitors

Interdigitated electrodes (IDEs) are the most commonly used planar form of capacitors. The use of IDEs has also been reported for sensing applications [35-37]. Studies on the optimization of IDE's by J. Min and A. J. Baeummer has revealed that key parameters of the IDE's geometry, such as electrode height (h), electrode finger spacing (s), electrode finger width (w) and number of electrode (N), play a major role with respect to signal-to-noise ratio of the output result [38]. It was also proved that the lower number of electrodes gives optimized output when compared to the larger number of electrodes. The capacitance of the IDE's can be calculated as given in [39-40]. The cross sectional view of the IDE's is shown in Fig. 5.5.

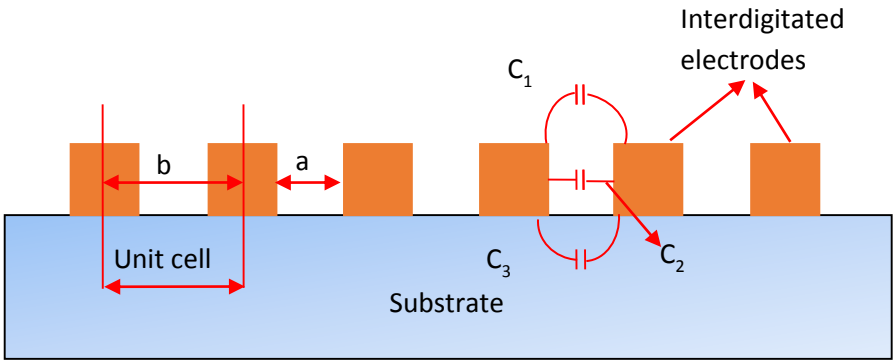

Figure 5.5. Cross sectional view of interdigitated electrodes

The total capacitance of the IDE's (C_{IDEs}) after omitting the edge effects is given by

$$C_{IDEs} = C_{uc} \times (n-1) \times l \tag{29}$$

Where n is the number of the unit cells. l is the length of the electrode. C_{uc} is the capacitance of unit cell given by

$$C_{uc} = C_1 + C_2 + C_3 \tag{30}$$

C_1, C_2 and C_3 are the partial capacitances of the unit cell. The capacitance C_2 can be treated as parallel plate capacitor whose capacitance is given by.

$$C_2 = \varepsilon_0 \times \varepsilon_1 \times \frac{h}{a} \tag{31}$$

ε_0 *and* ε_1 are the permittivities of vacuum and air, respectively. h is the thickness of the electrodes and a is the distance between electrodes. C_1 and C_3 are calculated using the complete elliptic integral of the first kind (K(k)) [40].

$$C_1 + C_2 = \varepsilon_0 \frac{\varepsilon_1 + \varepsilon_2}{2} \frac{K\left[\left(1 - (a/b)^2\right)^{1/2}\right]}{2K\left[(a/b)\right]} \tag{32}$$

ε_2 is the permittivity of the substrate. The complete elliptic integral of first kind is given by

$$K(k) = \int_0^1 \frac{dt}{\sqrt{(1-t)^2(1-k^2t^2)}} \tag{33}$$

The schematic of the designed coplanar inductor with electrode dimensions of 175 µm line width and 350 µm spacing, 43,000 µm outer diameter (d_{out}), 22,000 µm inner diameter (d_{in}) and 20 turns, is shown in Fig. 5.6(a). For the capacitor, the IDE's will have 9 pair of electrodes with 5200 µm electrode length, 200 µm electrode width and spacing. Figure 5.6(b) shows the schematic of the capacitor. The calculated IDEs capacitance and circular spiral inductance are 1.19 pF and 13.7 µH, respectively.

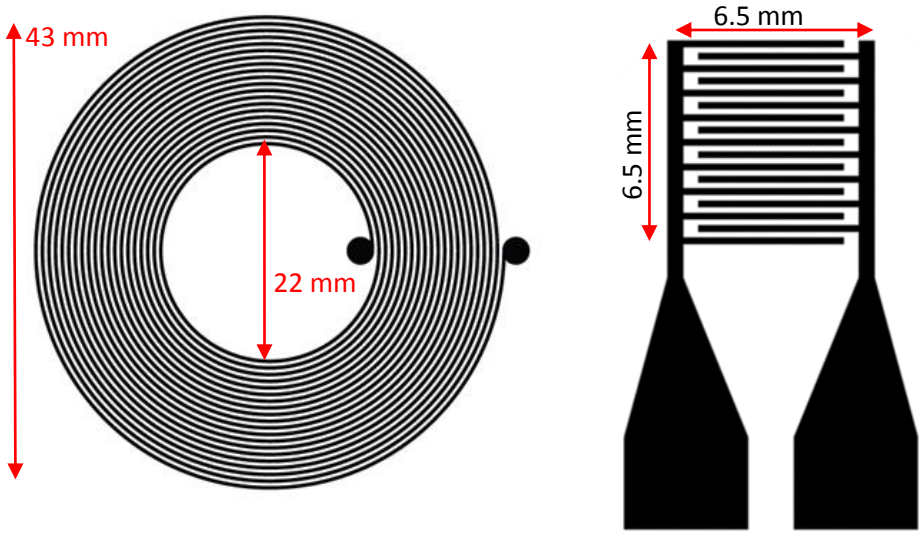

Figure 5.6. Schematic of the (a) coplanar inductor and (b) IDE's

5.4. Materials and Chemicals

Melinex ST 505, a flexible PET of 130 µm thickness, from DuPont Teijin Films was used as a substrate. Henkel Electrodag 479SS, a silver flake ink, was used for metalizing the coplanar LC sensor. Dodecyl sulfide, $Hg(NO_3)_2$ and $Pb(NO_3)_2$ (all in powder form) were purchased from Sigma–Aldrich chemical company. Palladium acetate [$Pd_3(OAc)_6$] was purchased from Strem Chemicals (Newbury Port, MA). Various concentrations of Hg^{2+} and Pb^{2+} (1 nM, 1 µM, 50 µm, 250 µm, 500 µm,

750 µm and 1 mM) were prepared by dissolving $Hg(NO_3)_2$ and $Pb(NO_3)_2$ in de-ionized (DI) water. The prepared solutions were stored in 10 mL aliquots at 2 °C.

5.5. Fabrication of the wireless LC sensor and synthesis of Pd Nps

A 12" ×12" stainless steel screen with 325 mesh count and 28 µm wire diameter resulting in open area of 41 % was fabricated at MicroScreen®, USA. A screen printer (AMI MSP 485) from Affiliated Manufacturers Inc. was used to deposit the coplanar inductor and IDE's, on PET with Ag flake ink. PET was cleaned with isopropyl alcohol (IPA) before printing. The printed layer was thermally cured in a conventional oven at 90 °C for 25 minutes. Screen printed planar inductors and capacitors are shown in Fig. 5.7. Figure 5.8 shows the vertical scanning interferometry 3D topography of the printed electrodes, which was measured using a Bruker Contour GT-K profilometer (Bruker Biosciences Corporation, USA), with Bruker Vision software operating in hybrid mode. The average thickness and RMS roughness of the printed electrodes were measured as 6.7±1.4 µm and 0.84 ±0.1 µm, respectively. The measured value of inductance and capacitance are 4.8 ± 0.15 µH and 4.21 ± 0.1 pF. The resonant frequency from the measured capacitance and inductace value is 35.3 ± 1.2 MHz. For this resonanting frequency, the losses due transmission line can be ignored as the wavelength of the porpagating signal through the inductor is ≈5 times larger than length of the inductor.

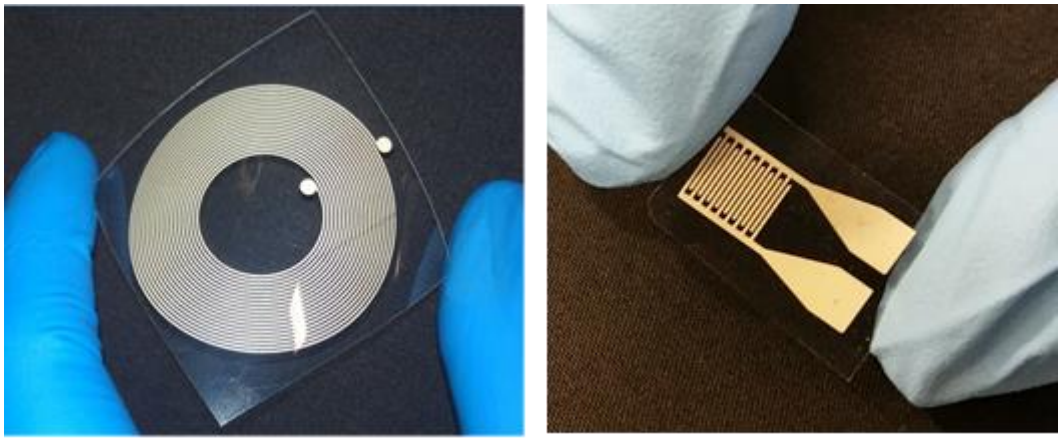

(a) (b)

Figure 5.7. Screen printed (a) planar inductor and (b) IDE's

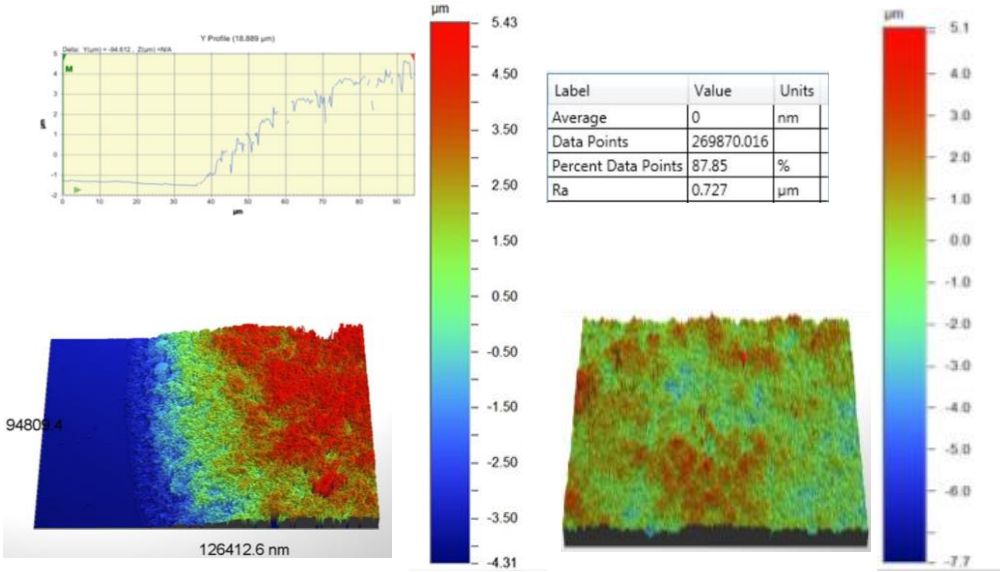

(a) (b)

Figure 5.8. 3D topography of the printed electrodes showing (a) average thickness and (b) RMS roughness of the screen printed electrodes

Synthesis of Pd Nps

The author demonstrates the use of palladium nanoparticles (Pd Nps) as sensing layers for the detection of heavy metal ions. The synthesis of these compound was previously reported [41-42]. Pd NPs are synthesized by modified pyrolysis reaction. 0.05 g of 0.075 mM $Pd_3(OAc)_6$ and 0.14 g of 0.37 mM n-dodecyl sulfide was added to 30 mL of ethanol. The reaction mixture was heated at 90°C for 1 hour

resulting in a color change of the solution from orange to dark brown indicating NP formation. The solution was then diluted with 300 mL of milli-Q water (18 MΩ·cm). Synthesized Pd NPs have a spherical shape with 2 nm diameter [41].

5.6. Sensor Preparation, Experiment Setup and Background Noise Subtraction

First, the sensor surface was prepared for the detection of the Pb^{2+} and Hg^{2+}. 40 µL of Pd NPs in ethanol was drop casted onto the IDEs at 100 °C to form sensing layers for Hg^{2+} and Pb^{2+} detection. Then, the IDEs were attached to the screen printed inductors using jumper wires and conductive silver epoxy from CircuitWorks® (CW-2400). The printed wireless sensor was remotely interrogated with a printed detection coil (screen printed planar inductor) by measuring S_{11} using an Agilent network analyzer (4395A). Figure 5.9 shows the experiment setup. Calibration for wires and probes was done before taking measurements.

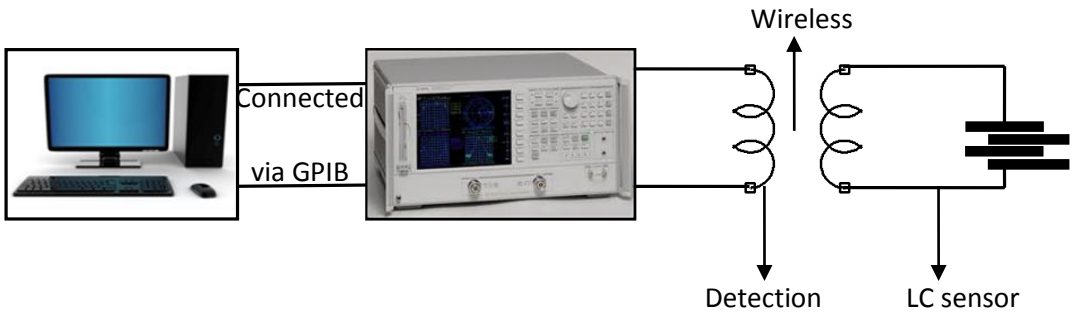

Figure 5.9. Experiment setup

The passive LC sensor and the detection coil were placed in the same axis with separation distance of ≈3 mm. The response of the LC sensor in this chapter was studied by interrogation of the impedance of a detection coil using an S- parameter test setup connected to network analyzer. The S_{11} response of the detection coil with and without the presence of the LC sensor was recorded and shown in Fig. 5.10. The resonant frequency of the sensor was measured at 34.2 MHz. As shown in Fig. 5.10,

the recorded signal a significant amount of what at first appears to be noise. By collecting the data without the sensor, the noise like term is also present; suggesting that is a measurement and instrumentation computation bias. To overcome this, the signal has been subtracted from the background coil response (S_{11} response of the detection coil without the sensor). The instrument measurements have also been averaged 50 times before recording each value. This resulted in a pure sensor response as shown in Fig. 5.11.

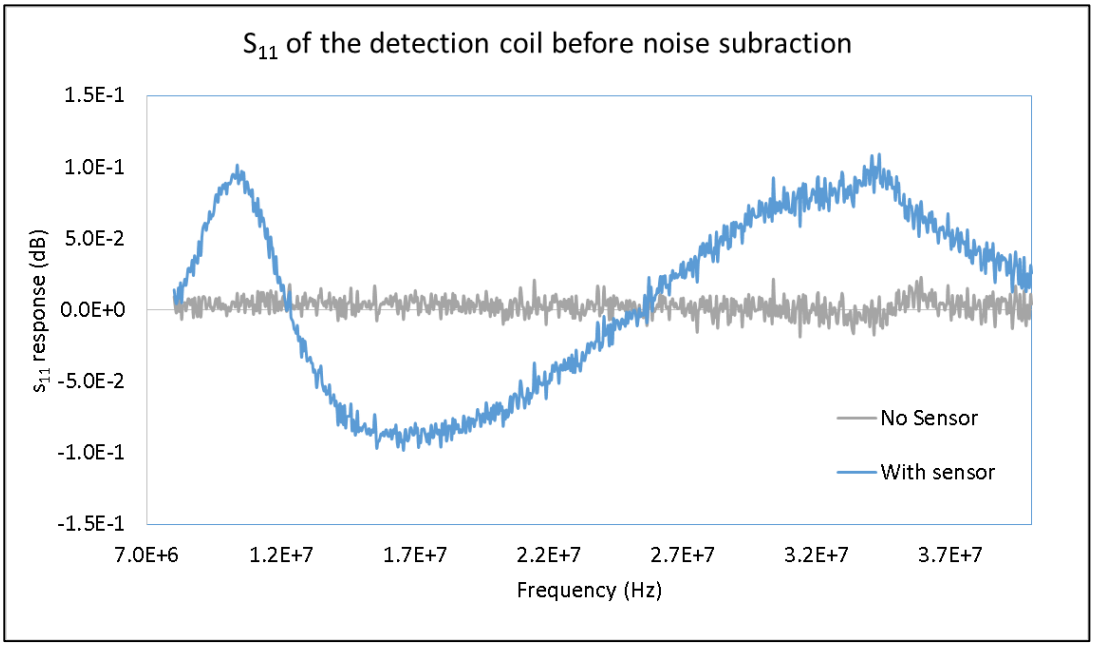

Figure 5.10. Measured S_{11} of the detection coil before noise subtraction

50 µl of varying concentrations of Pb^{2+} and Hg^{2+} were then loaded onto the IDE's of LC sensor using a pipette. The frequency spectrum from 8 MHz to 38 MHz was observed using the network analyzer. The LC sensor was rinsed with DI water before each experiment. All measurements were conducted at room temperature.

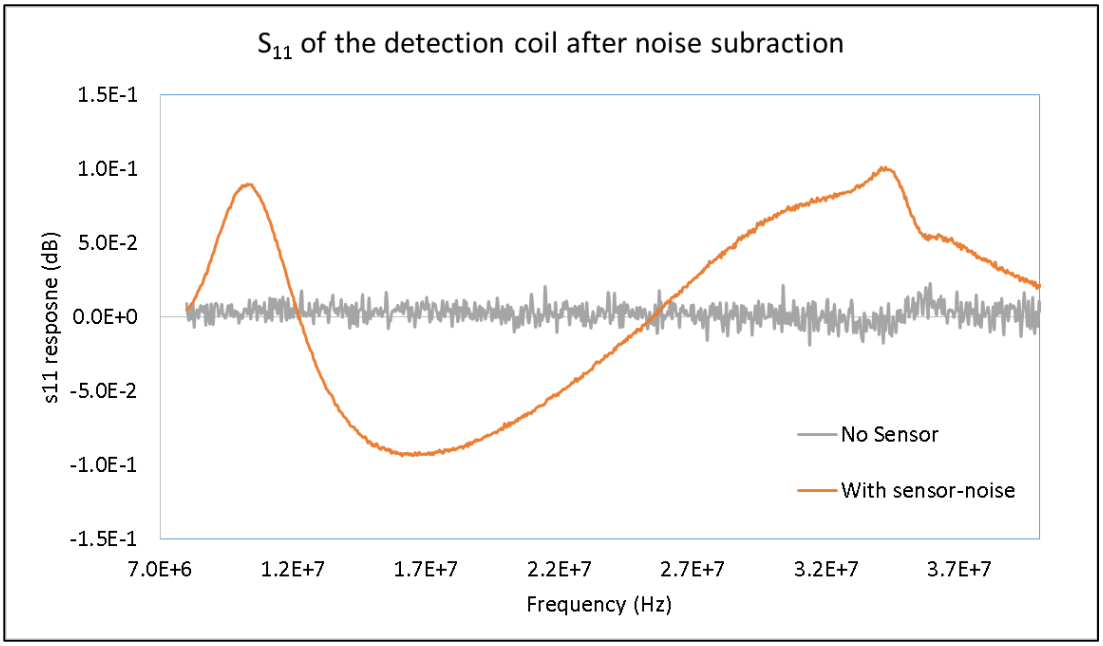

Figure 5.11. Measured S_{11} of the detection coil after noise subtraction showing the pure sensor response

5.7.Response of the Sensor Towards Heavy Metals

The S_{11} response of the Pd Np drop casted sensor was first tested towards different concentrations of Pb^{2+} (shown in Fig. 5.12). Initially, a reference signal was established by loading 50 µL of DI water on to the sensor using a pipette. Then, 50 µL of test sample solutions with varying concentrations of Pb^{2+} were introduced onto the sensor. Average changes in frequency measurements of around 4.2 kHz, 33.3 kHz, 125 kHz and 177 kHz were measured for the 50 µM, 100 µM, 500 µM and 1 mM concentrations of Pb^{2+}, respectively. The wireless frequency response of the printed LC sensor demonstrated a detection level as low as 50 µM and the capability of the printed LC sensor to distinguish among a wide range (micro and milli level) of sample concentrations. A statistical analysis for the reproducibility of the printed LC sensor response was performed by investigating the S_{11} response of three different sensors, towards varying concentrations of Pb^{2+}. Figure 5.13 shows the response of the sensor towards varying concentrations of Pb^{2+}. The standard deviation in the

frequency response was 2.9 kHz, 25.7 kHz, 26.5 kHz and 39.6 kHz for 50 µM, 100 µM, 500 µM and 1 mM concentrations of Pb^{2+}. From these results demonstrated by LC sensor, it can be concluded that the printed sensor could be used to quantify the different concentrations of Pb^{2+} as there was no cross-over in the overall change in frequency values, among all three sensors tested.

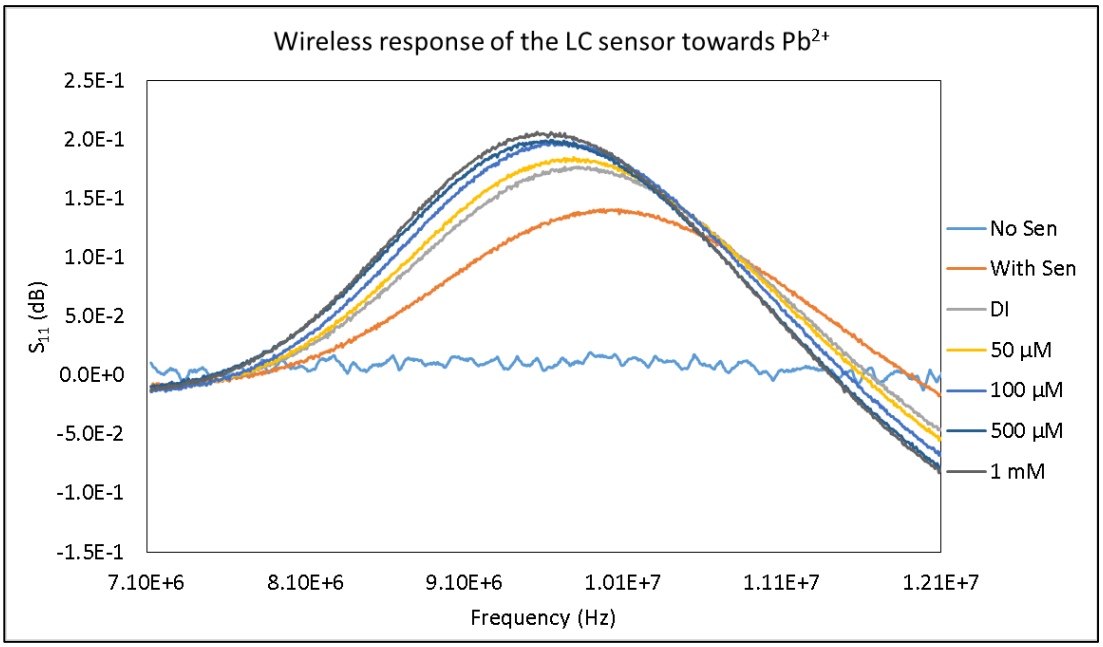

Figure 5.12. Response of the Pd NPs drop cated LC sensor towards varying concentrations of Pb^{2+}

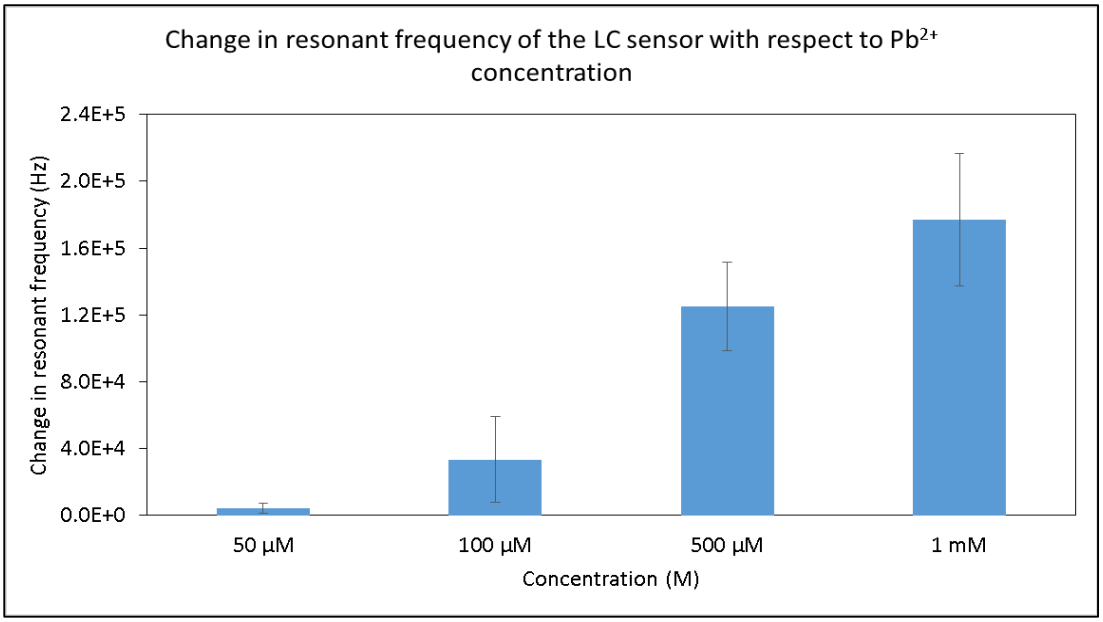

Figure 5.13. Change in the resonant frequency of the LC sensor towards varying concentrations of the lead ions

The response and sensitivity of the Pd NP drop casted sensor was then tested towards Hg^{2+}. Test sample solutions with varying concentrations of Hg^{2+} were introduced onto the sensor. The response of the printed LC sensor towards Hg^{2+} is shown in Fig. 5.14. It was observed that an average change in the resonant frequency of the LC sensor was 86.9 kHz, 92.6 kHz, 0.4 MHz and 0.93 MHz, with an average standard deviation of 9 kHz, 2.9 kHz, 58.9 kHz and 0.29 MHz was observed for the 50 µM, 100 µM, 500 µM and 1 mM concentrations, respectively, with respect to established reference signal of DI water (shown in Fig. 5.15).

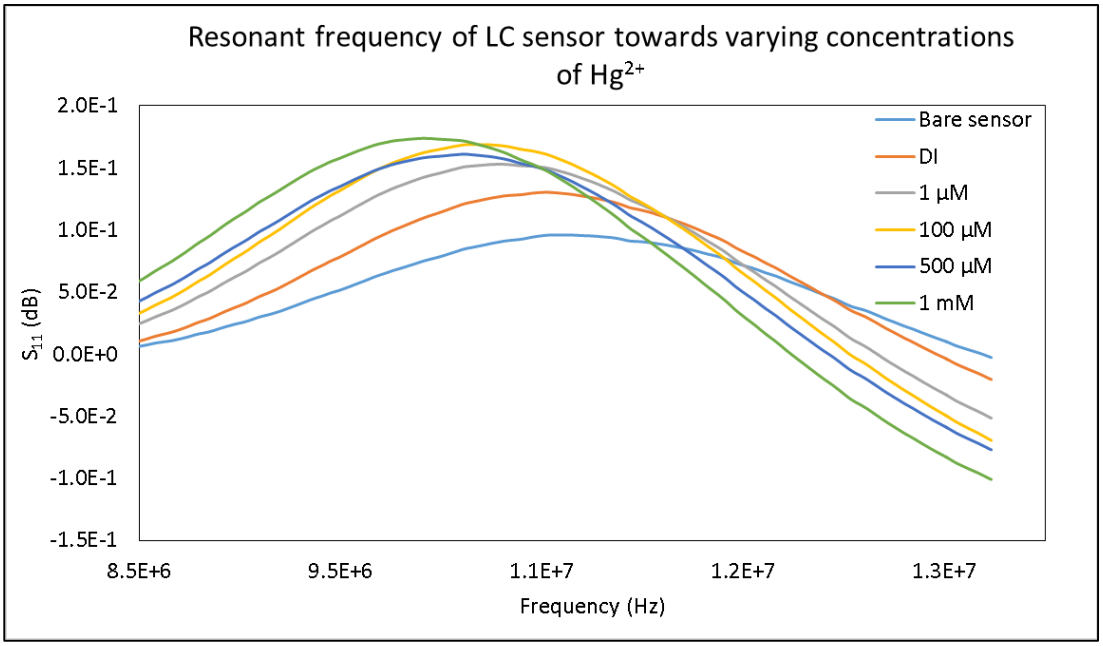

Figure 5.14. Response of the Pd NPs drop cated LC sensor towards varying concentrations of Hg^{2+}

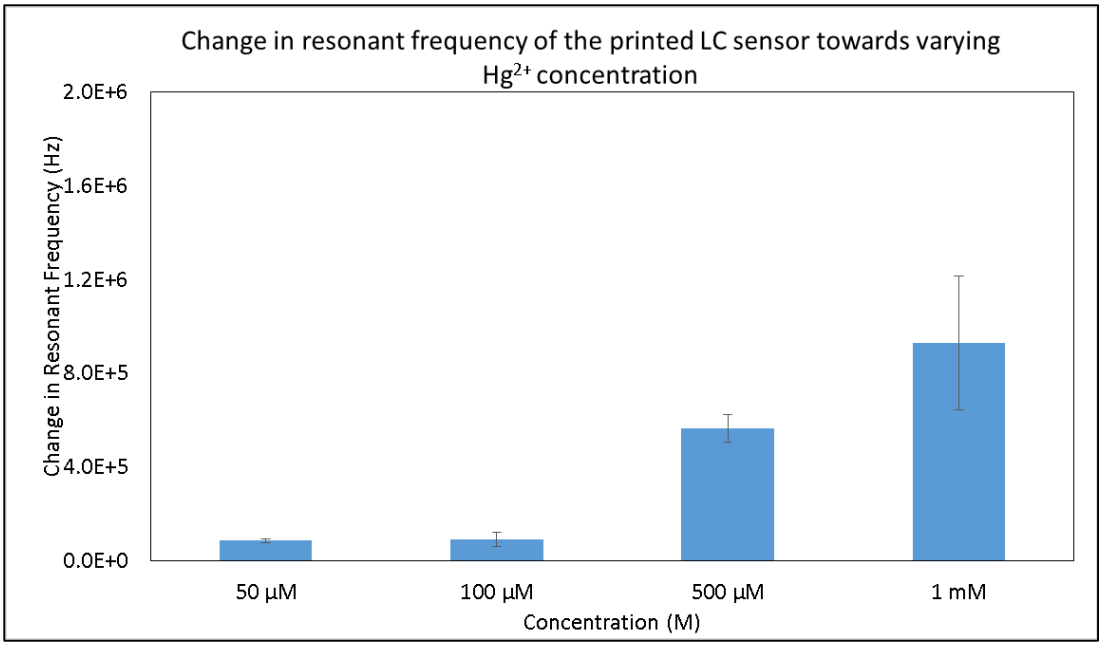

Figure 5.15. Change in the resonant frequency of the LC sensor towards varying concentrations of the mercury ions

The change in the resonant frequency of the Pd NP based sensor towards varying concentrations of heavy metal ions can be related to the change in dielectric constant of the Pd NPs. Increase in the concentration of the Hg^{2+} influences and changes the dielectric constant of the metallic nanoparticle surface, which in turn changes the capacitance of the sensor. This change in the dielectric constant is due to the formation of metal oxides when the metallic nanoparticles react with the heavy metals, which in turn was reported to be indirectly measured using the surface plasmon resonance (SPR) technique [43-44]. Literature shows that the SPR wavelength of gold and silver nanoparticles shift with respect to concentration of the heavy metal ions [45-46]. This shift can be theoretically quantized and is explained by Mie theory [47]. According to this theory, factors that affect the electron charge density of the particle surface will have a high impact on the SPR wavelength. Some of these factors include: particle size, dielectric constant of the surrounding medium,

metal type and shape. The SPR of nanoparticles smaller than 20 nm can be quantitatively explained by equation 34 [43, 47].

$$\sigma_{ext} = \frac{9\,V\,\varepsilon_m^{3/2}}{\lambda}\,\frac{\omega\,\varepsilon_2(\omega)}{(\varepsilon_1(\omega)+2\varepsilon_m)^2+\varepsilon_2(\omega)^2} \tag{34}$$

where λ and ω are the wavelength and angular frequency of the incident light, respectively. ε is the complex dielectric constant of the metal given by $\varepsilon(\omega) = \varepsilon_1(\omega) + i\,\varepsilon_2(\omega)$, $\varepsilon_1(\omega)$ is the real part and $\varepsilon_2(\omega)$ is the imagery part of the dielectric function of the metal, ε_m is the dielectric constant of the surrounding medium, which is related to the refractive index of the medium.

From the studies reported in the literature [45-46], it is clear that the surface of metallic nanoparticles are influenced by introducing varying concentrations of heavy metals. According to Mie theory, the surface effects, in the case of gold and silver, change in wavelength, which is directly related to the change in dielectric constant of the nanoparticles as all other parameters in the equation are maintained constant throughout the experiment in this study. Thus, it can be concluded that the properties of metallic nanoparticles are sensitive to changes in their dielectric constant, which can be brought about by different concentrations of the heavy metals. This change directly corresponds the resonant peak shift in the LC sensor as shown in Fig. 5.14.

5.8. Summary

In this chapter, the author briefly discussed the importance of heavy metal ions and wireless LC sensor. The working principle of the LC sensor was briefly covered. A detailed account of the experimental tasks involved in this work was then presented. This includes the materials, chemical used and brief synthesis of the sensing layer for selective detection of heavy metal ions. Experiment setup is also

presented. Finally, the change in resonant frequency of the printed sensor towards heavy metals is presented.

To summarize, a printed LC sensor was successfully fabricated on flexible PET substrate using a traditional screen printing process. Silver based flake ink was used for metallizing the planar inductor and capacitor. The planar inductor consists of 20 turns, 175 µM line width and spacing, 43 mm outer width and 22 mm inner width. IDE has 9 pair of electrodes with each electrode dimensions of 5200 µm length, 200 µm width and spacing. Pd Nps were synthesized and used as sensing layer for Pb^{2+} and Hg^{2+}. Change in resonant frequency of the LC sensor with varying concentrations of heavy metals ions was recorded. Quantitative detection of Pb^{2+} and Hg^{2+} was made possible as low as 50 µM detection level. The sensor also has concentration specific signals toward Pb^{2+} and Hg^{2+}, which is necessary for devices that can determine the amount of possible exposure levels.

In the following chapter, the author concludes the dissertation by summarizing all the three projects. The author also provides suggestions for future work.

References

[1] J. Morton, N. Havens, A. Mugweru, A.K. Wanekaya, “Detection of trace heavy metal ions using carbon nanotube- modified electrodes”, Electroanalysis, vol. 21 pp. 1597–1603, 2009.

[2] I. Gammoudi, H. Tarbague, A. Othmane, D. Moynet, D. Rebière, R. Kalfat, C. Dejous, “Love-wave bacteria-based sensor for the detection of heavy metal toxicity in liquid medium”, Biosensors and Bioelectronics vol. 26, pp. 1723–1726, 2010.

[3] Q.H. Zheng, C.H. Jang, “Liquid crystal-based sensors for the detection of heavy metals using surface-immobilized urease”, Colloids and Surfaces B: Biointerfaces, vol. 88, pp.622– 626, 2011.

[4] M. Souiri, I. Gammoudi, H.B. Ouada, L. Mora, T. Jouenne, N.J. Renault, C. Dejous, A. Othmane, A.C. Duncan, “Escherichia coli-functionalized magnetic nanobeads as an ultrasensitive biosensor for heavy metals”, Procedia Chemistry, pp.1027–1030, 2009.

[5] G. Aragay, J. Pons, A. Merkoci, “Recent trends in macro-, micro-, and nanomaterial-based tools and strategies for heavy-metal detection”, Chemical Reviews, vol. 111, pp. 3433–3458, 2011.

[6] C.S. Wu, M.K.O. Khaing, X. Fan, “Highly sensitive multiplexed heavy metal detection using quantum-dot-labeled DNAzymes”, ACS Nano, vol. 4, pp.5897-5904, 2010.

[7] A. Abbaspour, M.A. Mehrgardi, A. Noori, M.A. Kamyabi, A.K. Nezhad, M.N.S. Rad, “Speciation of iron(II), iron(III) and full-range pH monitoring using paptode: A simple colorimetric method as an appropriate alternative for optodes”, Sensors and Actuators B Chemical, vol. 113, pp.857-865, 2006.

[8] B.B. Narakathu, M.Z. Atashbar, B.E. Bejcek, “Improved detection limits of toxic biochemical species based on impedance measurements in electrochemical biosensors”, Biosensors and Bioelectronics, vol.26, pp.923–928, 2010.

[9] K.V. Raju, G.D. Sudhakar, T.B. Patrudu, “Spectrophotometric titration of resorufin and resazurin with iron(II) in strong phosphoric acid medium and resorufin as a new redox indicator in the reductimetric titration of some metal ions”, Asian Journal of Chemistry, vol. 19, pp. 683-692, 2007.

[10] C. Fay, K.-T. Lau, S. Beirne, C. ÓConaire, K. McGuinness, B. Corcoran, N.E. O’Connor, D. Diamond, S. McGovern, G. Coleman, R. Shepherd, G. Alici, G. Spinks, G. Wallace, “Wireless aquatic navigator for detection and analysis (WANDA)”, Sensors and Actuators B Chemical, vol. 150, pp. 425-435, 2010.

[11] F. Mieyeville, M. Ichchou, G. Scorletti, D. Navarro, W. Du, “Wireless sensor networks for active vibration control in automobile structures”, Smart Materials and Structures, vol. 21, pp.075009 (1-13), 2012.

[12] S.T.J. Kaiser, “Passive telemetric readout system”, Journal of IEEE Sensors, vol.6, pp. 1340–1345, 2006.

[13] W. Mokwa, “Medical implants based on microsystems”, Measurement Science and Technology, vol. 18, pp. 47–57, 2007.

[14] C. Reese, M. Roberts, M.M Ling, Z. Bao, “Organic thin film transistors”, Materials Today, vol.7, pp.20-207, 2004.

[15] T.J. Harpster, B. Stark, K. Najafi, “A passive wireless integrated humidity sensor,” Sensors and Actuators A Physical, vol. 95, pp. 100-107, 2002.

[16] R. Nopper, R. Niekrawietz, L. Reindl, “Wireless Readout of Passive LC Sensors”, IEEE Transactions on Instrumentation and Measurement, vol. 59 (9), pp.2450-2457, 2010.

[17] O. Akar, T. Akin, K. Najafi, “A wireless batch sealed absolute capacitive pressure sensor”, Sensors and Actuators A: Physical, vol. 95(1), pp. 29-38, 2001.

[18] T.J. Harpster, B. Stark, K. Najafi, “A passive wireless integrated humidity sensor”, Sensors and Actuators A: Physical, vol. 95 (2–3), pp. 100-107, 2002.

[19] D.M. Pozar, “Microwave Engineering, Second Edition,” John Wiley and Sons, Inc., pp. 56-213, 1998.

[20] A.J. DeRouin, “Inductive-capacitive resonant circuit sensors for structural health and environmental monitoring”, 2014.

[21] S. Raju, R. Wu, M. Chan, M., C.P. Yue, “Modeling of mutual coupling between planar inductors in wireless power applications”, IEEE Transactions on Power Electronics, vol. 29(1), pp. 481-490, 2014.

[22] I. Papagiannopoulos, G. De Mey, V. Chatziathanasiou, “Current distribution in circular planar coil”, Engineering Analysis with Boundary Elements, vol. 37(4), pp. 747-756, 2013.

[23] J.W. Kim, “Frequency Characteristics of Octagonal Spiral Planar Inductor”, Journal of the Korea Academia-Industrial cooperation Society, vol. 13(3), pp. 1284-1287, 2012.

[24] M. Zolog, D. Pitica, O. Pop, “Characterization of Spiral Planar Inductors Built on Printed Circuit Boards”, 30th International Spring Seminar on Electronics Technology, pp.308-313, 2007.

[25] J. Uei-Ming, M. Ghovanloo, “Design and Optimization of Printed Spiral Coils for Efficient Transcutaneous Inductive Power Transmission”, IEEE Transactions on Biomedical Circuits and Systems, vol. 1(3), pp.193-202, 2007.

[26] L. Wei Y. Ze-Hong Z. Yi-Bo, L.V. Miao, “A single-arm rectangular spiral antenna with a tilted beam”, International Workshop on Microwave and Millimeter Wave Circuits and System Technology (MMWCST), pp. 79-82, 2013.

[27] X. Zhang, Y. Han, W. Li, X. Duan, “A Rectangular Planar Spiral Antenna for GIS Partial Discharge Detection”, International Journal of Antennas and Propagation, vol. 985697, pp. 1-7, 2014.

[28] L. Gong; K.Y. Chan, R. Ramer, “A beam steering single-arm rectangular spiral antenna with large azimuth space coverage”, IEEE 14th Annual Wireless and Microwave Technology Conference (WAMICON), pp. 1-4, 2013

[29] N.A. Hadi, K. Ismail, S. Sulaiman, M.A. Haron, “Design of a rectangular spiral antenna for Wi-Fi application”, 13th International Conference In Advanced Communication Technology (ICACT), pp. 30-34, 2011.

[30] T.H. Lee, “The design of CMOS radio-frequency integrated circuits”, Cambridge university press, 2004.

[31] J. Chen, J.J. Liou, “On-chip spiral inductors for RF applications: an overview”, Journal of semiconductor technology and science, vol. 4(3), pp. 149-167, 2004.

[32] S. Chaki, S. Aono, N. Anodoh, Y. Sasaki, N. Tanino, O. Ishihara, “Experimental study on spiral inductors, Digest of IEEE International Microwave Theory and Techniques Symposium, pp. 753-756, 1995.

[33] K.K. Samanta, I.D. Robertson, “Layout efficient and high performance circular spiral inductors for multilayer multichip modules”, European Microwave Integrated Circuits Conference (EuMIC), , pp.596,599, 2011.

[34] M. Radulescu, “Spiral chip inductors design modelling overview”, Application Note USM, http://www.usmicrowaves.com/appnotes/usm_an_105.htm [Accessed: May. 10, 2015]

[35] N. Chidambaram, D. Balma, R. Nigon, A. Mazzalai, R. Matloub, C.S. Sandu, P. Muralt, “Converse mode piezoelectric coefficient for lead zirconate titanate thin film with interdigitated electrode”, Journal of Micromechanics and Microengineering, vol. 25(4), pp. 045016, 2015.

[36] R. Kamath, M.J. Madou, “Selective Detection of Dopamine against Ascorbic Acid Interference Using 3D Carbon Interdigitated Electrode Arrays”, ECS Transactions, vol. 61(7), pp. 65-73, 2014

[37] M. Bäcker, F. Kramer, C. Huck, A. Poghossian, A. Bratov, N. Abramova, M.J. Schöning, “Planar and 3D interdigitated electrodes for biosensing applications: The impact of a dielectric barrier on the sensor properties”, physica status solidi (a), vol. 211(6), pp. 1357-1363, 2014.

[38] J. Min and A.J. Baeumner, “Characterization and optimization of interdigitated ultramicroelectrode arrays as electrochemical biosensor transducers”, Electroanalysis, vol. 16, pp. 724-729, 2004.

[39] K.G. Ong, C.A. Grimes, “A resonant printed-circuit sensor for remote query monitoring of environmental parameters”, Smart Materials and Structures vol. 9, pp. 421–428, 2000.

[40] H.E. Endres, S. Drost, “Optimization of the geometry of gas-sensitive interdigital capacitors”, Sensors and Actuators B Chemical vol. 4 pp.95–98, 1991.

[41] C.P. Adams, K.A. Walker, S.O. Obare, K.M. Docherty, “Size-dependent antimicrobial effects of novel palladium nanoparticles”, PloS one, vol. 9(1), pp. e85981(1-11), 2014.

[42] M. Ganesan, R.G. Freemantle, S.O. Obare, “Monodisperse thioether-stabilized palladium nanoparticles: synthesis, characterization, and reactivity”, Chemistry of materials, vol. 19(14), pp. 3464-3471, 2007.

[43] S. Link, M.A. El-Sayed, “Optical properties and ultrafast dynamics of metallic nanocrystals”, Annual review of physical chemistry, vol. 54(1), pp. 331-366, 2003.

[44] Y.L. Hung, T.M. Hsiung, Y.Y. Chen, Y.F. Huang, C.C. Huang, “Colorimetric detection of heavy metal ions using label-free gold nanoparticles and alkanethiols”. The Journal of Physical Chemistry C, vol. 114(39), pp. 16329-16334, 2010.

[45] M. Annadhasan, T. Muthukumarasamyvel, V.R. Sankar Babu, N. Rajendiran, “Green synthesized silver and gold nanoparticles for colorimetric detection of Hg^{2+}, Pb^{2+}, and Mn^{2+} in aqueous medium”, ACS Sustainable Chemistry & Engineering, vol. 2(4), pp. 887-896, 2014.

[46] T. Morris, H. Copeland, E. McLinden, S. Wilson, G. Szulczewski, “The effects of mercury adsorption on the optical response of size-selected gold and silver nanoparticles”, Langmuir, vol. 18 (20), pp. 7261−7264, 2002.

[47] X. Huang, M.A. El-Sayed, “Gold nanoparticles: optical properties and implementations in cancer diagnosis and photothermal therapy”, Journal of Advanced Research, vol. 1(1), pp. 13-28, 2010.

CHAPTER VI

CONCLUSION AND FUTURE WORK

6.1 Conclusion

In the course of this dissertation, the successful fabrication of planar flexible sensors using traditional printing processes such as gravure, screen and inkjet printing has been demonstrated. Organic thin film transistor (OTFT) based humidity sensors fabricated using conventional lithographic techniques and traditional printing processes have also been demonstrated. . In addition, the possibility of screen printed electrochemical sensors for selective detection of heavy metal ions was investigated. Fabrication of flexible wireless LC sensors for quantitative detection of heavy metal ions was also part of the current work. The outcomes of each of the three research projects are listed below:

In the first project, traditional printing techniques were successfully used for the direct printing of OTFTs. Bottom gate electrode and dielectric layer were gravure printed on flexible polyethylene terephthalate (PET) using silver nanoparticle ink and UV clear dielectric ink, respectively. Source drain interdigitated electrodes (IDEs) were screen printed using a silver flake ink. TIPS pentacene, a humidity sensitive semiconductor, was inkjet printed onto the IDEs. The current voltage (I-V) characteristics of the fully printed OTFT were studied at ambient conditions. From the electrical characterization, it was noticed that the OTFT has a very high threshold voltage of 130 V which is not suitable for practical applications. It was concluded that this high voltage is due to the thickness (3.2 μm) of the dielectric layer. To overcome this, a second generation OTFT was successfully fabricated in which spin coating was used for the fabrication of the dielectric layer. The measured thickness of the spin

coated dielectric layer was 263 nm. The bottom electrode of the OTFT was also evaporated with Al to overcome the pinhole issues caused due to a thinner dielectric layer. Electrical characterization of the second generation OTFT was resulted in threshold voltage of 4 V. The response of the fabricated sensor towards a wide range of humidity of 15 %RH to 85 %RH was studied in an environmental chamber. Sensitivity of 0.9 % change in average drain current for 1 %RH change is recorded. A statistical analysis for the repeatability of the sensor response was also performed by investigating the humidity response of three different OTFTs. It was noticed that the fabricated sensor has a resolution of 15 %RH. The obtained results showed that the sensor is capable of sensing a wide range humidity and may readily be used as an OTFT based humidity sensor for various applications.

In the second project, a screen printed electrochemical sensor on flexible PET substrate was successfully developed for selective detection of heavy metal ions. Carbon and silver based inks were used for metallizing the electrodes. The fabricated device consisted of 1,700 µm radius working electrode, 1000 µm wide reference electrode and counter electrode with outer and inner radius of 3900 µm and 2900 µm, respectively. Author also successfully implemented 1,10-phenanthroline and its derivative naphtho[2,3-a]dipyrido[3,2-h:2',3'-f]phenazine-5,18-dione (QDPPZ) as sensing layer for selective detection of mercury (Hg^{2+}) and lead (Pb^{2+}) ions, respectively. Author has recorded the response of the electrochemical sensor using cyclic voltammetry (CV) technique. The CV based response showed the reduction peaks at 0.23 eV and -0.6 eV demonstrating the selective detection of Hg^{2+} and Pb^{2+}, respectively. In addition, concentration specific signals towards the Pb^{2+} and Hg^{2+} through statistical analysis was also recorded. From the results obtained, the potential of screen printed sensor for selective detection of heavy metal ions was shown.

In the third project, a passive wireless sensor printed on flexible PET for the quantitative detection of heavy metal ions was successfully developed. The wireless sensor consisted of an inductor-capacitor (LC) resonant circuit in planar form. Screen printing technique with silver flake ink was used for fabricating the planar inductor and IDE capacitor. The planar inductor consists of 20 turns, 175 µM line width and spacing, 43 mm outer diameter and 22 mm inner diameter. IDE has 9 pair of electrode with each electrode dimensions of 5200 µm length, 200 µm width and spacing. The use of palladium nano particles as a sensing layer for the quantitative detection of heavy metal ions was then demonstrated. The change in resonant frequency of the LC sensor towards varying concentrations of heavy metal ions was recorded and statistically analyzed. The quantitative detection of Pb^{2+} and Hg^{2+} with as low as 50 µM detection level was shown to be possible. From the results, the potential for a screen printed LC sensors for detection of heavy metal ions has been shown.

6.2 Future Work

Depending on the experiences gained during the course of this dissertation, there are several opportunities for improving the current projects as discussed below:

- ***Fabrication of Flexible Organic Thin Film Transistors (OTFTs) based Humidity sensors:***
    - Dielectric based inks could be printed using inkjet printing, which is known for depositing thinner films. This could lead to OTFTs with lower threshold voltages in which all layers could be deposited using printing processes.
    - The work function of the silver can be improved by treating the electrode surfaces with self-assembled monolayers (SAMs) such as thiophenol, 4-fluorothiophenol and pentafluorothiophenol [1]. In addition, gold

electrodes (work function: 5.1 eV) could be used to match the work function of source drain IDEs with semiconducting layer.

- OTFT can be fabricated in bottom gate and top contact form which is proved to have larger drain currents and smaller contact resistance compared to the bottom gate and bottom contact OTFT [2].
- Moreover humidity sensitive dielectric materials such as polymethyl methacrylate (PMMA) and poly (2-hydroxyethyl methacrylate) (PHEMA) [3] could be used to improve the sensitivity of OTFT based humidity sensors.

- ***A Screen Printed Flexible Electrochemical Sensor for the Detection of Toxic Heavy Metals:***
  - The sensing layer synthesis could be modified to improve the selectivity of the sensor. As per the present study, lead ions bind with the oxygen molecule of QDPPZ resulting in a reduction peak. The peak current could be increased by adding more oxygen molecules to QDPPZ. This might also help in detecting the lead ions lower than micro level concentrations.
  - Moreover the sensing layers can be developed as functional inks that can be directly printed on the working electrode.
  - The functional inks used for the counter electrode could be replaced with platinum to increase catalytic activity and chemical stability of the electrodes [4], resulting in possibility of detecting wide range concentrations of heavy metal ions.
  - The sensor can be optimized for better performance by designing it in COMSOL™ which could lead to lower detection levels.

- In addition, with the success of the OTFT, a flexible fully printed read out circuit for recording the cyclic voltammetry output of the sensor could be developed. This could lead to fully printed lab-on-chip system for the detection of heavy metal ions.

- ***Detection of Toxic Heavy Metals Using Printed Wireless LC Sensors:***
  - The functional inks used for the printed inductors could be replaced with nickel iron (NiFe) which is known for high permeability [5] resulting in higher inductance values with same dimensions.
  - Different materials for sensing layers such as gold nanoparticles and silver nanoparticles could be used to study and optimize the response of the LC sensor.
  - In addition, these metallic nanoparticles could be synthesized as functional inks and directly printed as sensing layers on IDEs.

References

[1] H.J. Pyo, P.A. Young, L. Seonghoon, K. Jihoon S. Nayool, Y.Y. Do, "Tuning of Ag work functions by self-assembled monolayers of aromatic thiols for an efficient hole injection for solution processed triisopropylsilylethynyl pentacene organic thin film transistors", Applied Physics Letters, vol. 92, pp. 143311, 2008.

[2] Z. He, "Tips pentacene crystal alignment for improving performance of solution processed organic thin film transistors", PhD dissertation, The University of Alabama Tuscaloosa, 2014.

[3] G. Harsányi, "Polymer films in sensor applications: a review of present uses and future possibilities", Sensor Review, vol. 20(2), pp. 98-105, 2000.

[4] Y. Gentian, J. Wu, Y. Xiao, M. Huang, J. Lin, L. Jeng-Yu, "High performance platinum-free counter electrode of molybdenum sulfide–carbon used in dye-sensitized solar cells", Journal of Materials Chemistry A vol. 1(4), pp. 1495-1501, 2013.

[5] Y.H. Chen, H.C. Chang, C.C. Lai, I.N. Chang, "Fabrication and application of a wireless inductance-capacitance coupling microsensor with electroplated high permeability material NiFe", Journal of Physics vol. 266(1), pp. 012066(1-5), 2011.

Appendices

Appendix

A1. Journal Papers:

1. *Z. Ramshani, **A.S.G. Reddy**, B.B. Narakathu, M.Z. Atashbar, "SH-SAW sensor based microfluidic system for the detection of heavy metal compounds in liquid environments", Sensors and Actuators B: Chemical, *(In Press).*
2. S. Emamian, A. Eshkeiti, **A.S.G. Reddy**, B.B. Narakathu, M.Z. Atashbar, "Gravure printed flexible surface enhanced Raman spectroscopy (SERS) substrate for detection of 2,4-dinitrotoluene (DNT) vapor", Sensors and Actuators B: Chemical, *(In Press).*
3. A. Eshkeiti, **A.S.G. Reddy**, S. Emamian, B.B. Narakathu, M. Joyce, M.K. Joyce, P.D. Fleming, B.J. Bazuin, M.Z. Atashbar, "Screen printing of multi-layered hybrid printed circuit boards (PCB) on different substrates", IEEE Transactions on Device and Materials Reliability, vol. 5(3), pp. 415-421, 2015.
4. B.B. Narakathu, M.S. Devadas, **A.S.G. Reddy**, A. Eshkeiti, A. Moorthi, I.R. Fernando, B. Miller, G. Ramakrishna, E. Sinn, M.K. Joyce, M. Rebros, E. Rebrosova, G. Mezei, M.Z. Atashbar, "Novel fully screen printed flexible electrochemical sensor for the investigation of electron transfer between thiol functionalized viologen and gold clusters", Sensors and Actuators B: Chemical, vol. 176, pp. 768-774, 2013.
5. A. Eshkeiti, B.B. Narakathu, **A.S.G. Reddy**, A. Moorthi, M.Z. Atashbar, "Detection of toxic heavy metals using A novel inkjet printed surface

enhanced Raman spectroscopy (SERS) substrate", Sensors and Actuators B: Chemical, vol. 171-172, pp. 705-711, 2012.

6. **A.S.G. Reddy**, B.B. Narakathu, M.Z. Atashbar, M. Rebros, E. Hrehorova, B.J. Bazuin, M.K. Joyce, P.D. Fleming, A. Pekarovicova, "Printed capacitive based humidity sensors on flexible substrates", Sensor Letters, vol. 9, pp. 869-871, 2011.
7. M.J. Joyce, **A.S.G. Reddy**, P.D. Fleming, S.Emamian, A. Eshkeiti, M.Atashbar, T. Donato, "Contribution of Flexo Process Variables to Fine Line Ag Electrode Performance", International Journal of Engineering Research & Technology, vol. 3 (8), 1645-1656, 2014.
8. B.B. Narakathu, **A.S.G. Reddy**, A. Eshkeiti, S. Emamian, M.Z. Atashbar, "A printed and flexible microfluidic sensing platform for the detection of heavy metal compounds", IEEE Sensors Journal, (Submitted).

A2. Conference Papers:

9. B.B. Narakathu, **S.G.R. Avuthu**, D. Maddipatla, S. Emamian, A. Eshkeiti, A.A. Chlaihawi, B.J. Bazuin, M.Z. Atashbar, "Rapid prototyping of a flexible microfluidic sensing system using inkjet and screen printing processes", 14th IEEE Sensors Conference, November 1-4, Busan, South Korea, 2015(Submitted).
10. ***S.G.R. Avuthu**, J.T. Wabeke, B.B. Narakathu, D. Maddipatla, S. Emamian, A. Eshkeiti, A.A. Chlaihawi, M.K. Joyce, S.O. Obare, M.Z. Atashbar, "Development of screen printed electrochemical sensors for selective detection of heavy metals", 14th IEEE Sensors Conference, November 1-4, Busan, South Korea, 2015 (Submitted).

11. A.A. Chlaihawi, B.B. Narakathu, S. Emamian, A. Eshkeiti, **S.G.R. Avuthu**, B.J. Bazuin, M.Z. Atashbar, “Development of flexible dry ECG electrodes based on MWCNT/PDMS composite”, 14th IEEE Sensors Conference, November 1-4, Busan, South Korea, 2015 (*Submitted*).
12. ***S.G.R. Avuthu**, J.T. Wabeke, B.B. Narakathu, D. Maddipatla, S. Emamian, A. Eshkeiti, A.A. Chlaihawi, B.J. Bazuin, S.O. Obare, M.Z. Atashbar, “Detection of heavy metal ions using screen printed wireless LC sensor”, 14th IEEE Sensors Conference, November 1-4, Busan, South Korea, 2015 (*Submitted*).
13. D. Maddipatla, B.B. Narakathu, **S.G.R. Avuthu**, S. Emamian, A. Eshkeiti, A.A. Chlaihawi, B.J. Bazuin, M.K. Joyce, C.W. Barrett, M.Z. Atashbar, “A novel flexographic printed strain gauge on paper platform”, 14th IEEE Sensors Conference, November 1-4, Busan, South Korea, 2015 (*Submitted*).
14. S. Emamian, **S.G.R. Avuthu**, B.B. Narakathu, A. Eshkeiti, A.A. Chlaihawi, B.J. Bazuin, M.Z. Atashbar, “Fully printed and flexible piezoelectric based touch sensitive skin”, 14th IEEE Sensors Conference, November 1-4, Busan, South Korea, 2015 (*Submitted*).
15. A. Eshkeiti, Z. Ramshani, S. Emamian, B.B. Narakathu, **A.S.G. Reddy**, M.M. Ali, A. Chlaihawi, M.K. Joyce, D.P. Fleming, B.J. Bazuin, M.Z. Atashbar, “A stretchable and wearable printed sensor for human body motion monitoring”, 14th IEEE Sensors Conference, November 1-4, Busan, South Korea, 2015 (*Submitted*).
16. A.A. Chlaihawi, B.B. Narakathu, A. Eshkeiti, S. Emamian, **A.S.G. Reddy**, M.Z. Atashbar, “Screen printed MWCNT/PDMS based dry electrode sensor for electrocardiogram (ECG) measurements”, IEEE International Conference

on Electro/Information Technology (EIT), May 21-23, Dekalb, Illinois, USA, 2015 (*Accepted*).

17. Z. Ramshani, B.B. Narakathu, **A.S.G. Reddy**, S. Obare, M.Z. Atashbar, "SH-SAW sensor based heavy metal detection", Joint Conference of the IEEE International Frequency Control Symposium & European Frequency and Time Forum (IFCS-EFTF), April 12-16, Denver, Colorado, USA, 2015 (*Accepted*).
18. S. Emamian, A. Eshkeiti, B.B. Narakathu, **A.S.G. Reddy**, M.Z. Atashbar, "Detection of 2,4-dinitrotoluene (DNT) using gravure printed surface enhancement Raman spectroscopy (SERS) flexible substrate", Flexible and Printed Electronics Conference (FlexTech), February 23-26, Monterey, California, USA, 2015.
19. B.B. Narakathu, **A.S.G. Reddy**, A. Eshkeiti, S. Emamian, M.Z. Atashbar, "Development of a novel printed flexible microfluidic sensing platform based on PCB technology", 13th IEEE Sensors Conference, November 2-5, Valencia, Spain, pp. 665-668, 2014.
20. A. Eshkeiti, B.B. Narakathu, **A.S.G. Reddy**, S. Emamian, M.K. Joyce, B.J. Bazuin, M.Z. Atashbar, "Screen printed flexible capacitive pressure sensor", 13th IEEE Sensors Conference, November 2-5, Valencia, Spain, pp. 1192-1195, 2014.
21. A. Eshkeiti, M. Joyce, B.B. Narakathu, **A.S.G. Reddy**, S. Emamian, M.K. Joyce, M.Z. Atashbar, "A novel self-supported printed flexible strain sensor for monitoring body movement", 13th IEEE Sensors Conference, November 2-5, Valencia, Spain, pp. 1615-1618, 2014.
22. S. Emamian, A. Eshkeiti, B.B. Narakathu, **A.S.G. Reddy**, M.Z. Atashbar, "Gravure printed flexible SERS substrate for rapid and sensitive detection of

2,4-dinitrotoluene (DNT)", 13th IEEE Sensors Conference, November 2-5, Valencia, Spain, pp. 1069-1072, 2014.

23. ***A.S.G. Reddy**, B.B. Narakathu, A. Eshkeiti, S. Emamian, B.J. Bazuin, M. Joyce, M.Z. Atashbar, "Detection of heavy metal compounds using fully printed three electrode electrochemical sensor", 13th IEEE Sensors Conference, November 2-5, Valencia, Spain, pp. 669-672, 2014.
24. B.B. Narakathu, **A.S.G. Reddy**, A. Eshkeiti, S. Emamian, M.Z. Atashbar, "A novel flexible microfluidic platform: Integration of conventional printed circuit board technology and inkjet printing", 24th Anniversary World Congress on Biosensors (BIOSENSORS), May 27-30, Melbourne, Australia, pp. 120-121, 2014.
25. B.B. Narakathu, **A.S.G. Reddy**, A. Eshkeiti, B.J. Bazuin, M.Z. Atashbar, "A novel flow cell for opto-electrochemical based dual sensing of heavy metal compounds", 15th International Meeting on Chemical Sensors (IMCS), March 16-19, Beunos Aires, Argentina, pp. 48, 2014.
26. ***A.S.G. Reddy**, B.B. Narakathu, S. Emamian, A. Eshkeiti, B.J. Bazuin, M.K. Joyce, M.Z. Atashbar, "All printed pentacene organic thin film transistors for humidity sensing", 15th International Meeting on Chemical Sensors (IMCS), March 16-19, Beunos Aires, Argentina, pp. 107, 2014.
27. ***A.S.G. Reddy**, B.B. Narakathu, A. Eshkeiti, S. Emamian, B.J. Bazuin, M.K. Joyce, M.Z. Atashbar, "All screen printed circular electrodes as electrochemical sensors", 15th International Meeting on Chemical Sensors (IMCS), March 16-19, Beunos Aires, Argentina, pp. 98, 2014.
28. Z. Ramshani, B.B. Narakathu, **A.S.G. Reddy**, M.Z. Atashbar, "Heavy metal detection using shear horizontal surface acoustic wave (SH-SAW) sensors",

15th International Meeting on Chemical Sensors (IMCS), March 16-19, Beunos Aires, Argentina, pp. 88, 2014.

29. B.B. Narakathu, A. Eshkeiti, **A.S.G. Reddy**, S. Emamian, M.K. Joyce, P.D. Fleming, B.J. Bazuin, M.Z. Atashbar, "PDMS based flexible capacitive pressure sensor fabricated using printing technology", Flexible and Printed Electronics Conference (FlexTech), February 4-6, Phoenix, Arizona, USA, pp. 47, 2014.
30. B.B. Narakathu, M.S. Devadas, **A.S.G. Reddy**, A. Eshkeiti, G. Ramakrishna, E. Sinn, M.K. Joyce, G. Mezei, M.Z. Atashbar, "Investigation of electron transfer between gold clusters and (pseudo) rotaxanes using a novel screen printed flexible electrochemical sensor", Flexible and Printed Electronics Conference (FlexTech), February 4-6, Phoenix, Arizona, USA, pp. 46, 2014.
31. ***A.S.G. Reddy**, B.B. Narakathu, A. Eshkeiti, S. Emamian, B.J. Bazuin, M.K. Joyce, M.Z. Atashbar, "All screen printed circular electrodes as electrochemical sensors", Flexible and Printed Electronics Conference (FlexTech), February 4-6, Phoenix, Arizona, USA, pp. 45, 2014.
32. ***A.S.G. Reddy**, B.B. Narakathu, S. Emamian, A. Eshkeiti, M.K. Joyce, B.J. Bazuin, M.Z. Atashbar, "Fully printed electrochemical sensor on flexible substrates", Flexible and Printed Electronics Conference (FlexTech), February 4-6, Phoenix, Arizona, USA, pp. 45, 2014.
33. A. Eshkeiti, **A.S.G. Reddy**, B.B. Narakathu, S. Emamian, M. Rezaei, M.K. Joyce, P.D. Fleming, B.J. Bazuin, M.Z. Atashbar, "Screen printed capacitive pressure sensor", Flexible and Printed Electronics Conference (FlexTech), February 4-6, Phoenix, Arizona, USA, pp. 45, 2014.

34. B.B. Narakathu, **A.S.G. Reddy**, A. Eshkeiti, B.J. Bazuin, M.Z. Atashbar, "Opto-electrochemical based dual detection of heavy metal compounds using a novel flow cell", 12th IEEE Sensors Conference, November 3-6, Baltimore, Maryland, USA, pp. 1-4, 2013.
35. Z. Ramshani, B.B. Narakathu, **A.S.G. Reddy**, M.Z. Atashbar, "Investigation of SH-SAW sensors for toxic heavy metal detection", 12th IEEE Sensors Conference, November 3-6, Baltimore, Maryland, USA, pp. 1-4, 2013.
36. A. Eshkeiti, M. Rezaei, B.B. Narakathu, **A.S.G. Reddy**, M.Z. Atashbar, "Gravure printed paper based substrate for detection of heavy metals using surface enhanced Raman spectroscopy (SERS)", 12th IEEE Sensors Conference, November 3-6, Baltimore, Maryland, USA, pp. 1-4, 2013.
37. ***A.S.G. Reddy**, A. Eshkeiti, B.B. Narakathu, B. J. Bazuin, M.K. Joyce, M.Z. Atashbar, "Fully printed OTFT based flexible humidity sensors", 12th IEEE Sensors Conference, November 3-6, Baltimore, Maryland, USA, pp. 1-4, 2013.
38. B.B. Narakathu, **A.S.G. Reddy**, A. Eshkeiti, B.J. Bazuin, M.K. Joyce, M.Z. Atashbar, "Detection of biochemicals using a gravure printed flexible electrochemical sensor", Flexible and Printed Electronics Conference (FlexTech), January 29-February 1, Phoenix, Arizona, USA, pp. 18, 2013.
39. ***A.S.G. Reddy**, B.B. Narakathu, A. Eshkeiti, M.K. Joyce, B. J. Bazuin, M.Z. Atashbar, "Heavy metal detection using a flexible wireless printed LC sensor", Flexible and Printed Electronics Conference (FlexTech), January 29-February 1, Phoenix, Arizona, USA, pp. 17, 2013.
40. A. Eshkeiti, **A.S.G. Reddy**, B.B. Narakathu, M.K. Joyce, B.J. Bazuin, M.Z. Atashbar, "Detection of toxic heavy metals using a flexible printed

surface enhanced Raman spectroscopy (SERS) substrate", Flexible and Printed Electronics Conference (FlexTech), January 29-February 1, Phoenix, Arizona, USA, pp. 17-18, 2013.

41. A. Moorthi, B.B. Narakathu, **A.S.G. Reddy**, A. Eshkeiti, M.Z. Atashbar, "A novel flexible strain gauge sensor fabricated using screen printing", 6th International Conference on Sensing Technology: ICST 2012, December 18-21, Kolkata, India, pp. 765-768, 2012.
42. A. Eshkeiti, B.B. Narakathu, **A.S.G. Reddy**, A. Moorthi, M.Z. Atashbar, E. Rebrosova, M. Rebros, M.K. Joyce, "Detection of toxic heavy metals using a novel flexible gravure printed surface enhanced Raman spectroscopy (SERS) based substrate" 6th Asia-Pacific Conference on Transducers and Micro/Nano Technologies (APCOT), July 8-11, Nanjing, China, 2012.
43. B.B. Narakathu, A. Eshkeiti, **A.S.G. Reddy**, A. Moorthi, M.Z. Atashbar, "A novel fully printed and flexible capacitive pressure sensor", 11th IEEE Sensors Conference, October 28-31, Taipei, Taiwan, pp. 1935-1938, 2012.
44. A. Eshkeiti, B.B. Narakathu, **A.S.G. Reddy**, A. Moorthi, M.Z. Atashbar, "Gravure printed surface enhanced Raman spectroscopy (SERS) substrate for detection of toxic heavy metals", 11th IEEE Sensors Conference, October 28-31, Taipei, Taiwan, pp. 434-437, 2012.
45. ***A.S.G. Reddy**, A. Eshkeiti, B.B. Narakathu, A. Moorthi, M. Z. Atashbar, M. Rebros, E. Rebrosova, M.K. Joyce, "Fully printed wireless LC sensor for toxic heavy metal detection", 14th International Meeting on Chemical Sensors (IMCS), May 20-23, Nuremberg, Germany, pp. 1191-1194, 2012.
46. A. Eshkeiti, B.B. Narakathu, **A.S.G. Reddy**, A. Moorthi, M.Z. Atashbar, E. Rebrosova, M. Rebros, M.K. Joyce, "A novel flexible gravure printed

surface enhanced Raman spectroscopy (SERS) sensor for the detection of toxic heavy metals", 14th International Meeting on Chemical Sensors (IMCS), May 20-23, Nuremberg, Germany, pp. 1479-1482, 2012.

47. **A.S.G. Reddy**, B.B. Narakathu, M.Z. Atashbar, M. Rebros, E. Rebrosova, M.K. Joyce, "Gravure printed electrochemical biosensors", 25th Eurosensors Conference, September 4-7, Athens, Greece, vol. 25, pp. 956-959, 2011.
48. **A.S.G. Reddy**, B.B. Narakathu, M.Z. Atashbar, M. Rebros, E. Rebrosova, M.K. Joyce, "Fully printed flexible humidity sensor", 25th Eurosensors Conference, September 4-7, Athens, Greece, vol. 25, pp. 120-123, 2011.
49. A. Eshkeiti, B.B. Narakathu, **A.S.G. Reddy**, A. Moorthi, M.Z. Atashbar, "A novel inkjet printed surface enhanced Raman spectroscopy (SERS) substrate for the detection of toxic heavy metals", 25th Eurosensors Conference, September 4-7, Athens, Greece, vol. 25, pp. 338-341, 2011.
50. B.B. Narakathu, **A.S.G. Reddy**, M.Z. Atashbar, M.K. Joyce, "A novel gravure printed impedance based flexible electrochemical sensor", 10th IEEE Sensors Conference, October 28-31, Limerick, Ireland, pp. 577-580, 2011.
51. **A.S.G. Reddy**, B.B. Narakathu, M.Z. Atashbar, M. Rebros, E. Hrehorova, M.K. Joyce, "Flexible electrochemical biosensor using Rotogravure printing", 10th Annual Flexible Electronics and Displays Conference, February 7-10, Phoenix, Arizona, USA, pp. 37, 2011.
52. **A.S.G. Reddy**, B.B. Narakathu, M.Z. Atashbar, M. Rebros, E. Hrehorova, M.K. Joyce, "Printed wireless humidity sensors on flexible substrates", 10th Annual Flexible Electronics and Displays Conference, February 7-10, Phoenix, Arizona, USA, pp. 37, 2011.

53. **A.S.G. Reddy**, B.B. Narakathu, M.Z. Atashbar, M. Rebros, E. Hrehorova, M.K. Joyce, “Printed electrochemical based biosensors on flexible substrates”, 9th IEEE Sensors Conference, November 1-4, Waikoloa, Hawaii, USA, pp. 1596-1600, 2010.

54. **S.G.R. Avuthu**, B.B. Narakathu, M.Z. Atashbar, M. Rebros, E Hrehorova, B.J. Bazuin, D. Fleming, M.K. Joyce, “Printed capacitive based humidity sensors on flexible substrates”, 13th International Meeting on Chemical Sensors (IMCS), July 11-14, Perth, Australia, pp. 124, 2010.